Study of Radiative Muon Capture for COMET Phase-I Experiment

Dorian PIETERS

A thesis submitted in partial fultillment of the requirements for the degree of Doctor of Science

Graduate school of science
Osaka University
Japan
March 31, 2023

Abstract

The COMET Phase-I experiment will search for the coherent decay of a muonic atom into an electron. While in the Standard Model, extended with neutrino oscillations, this process is strictly suppressed ($\mathcal{O}(10^{-54})$), many models beyond the Standard Model predict its possibility at an observable rate. This makes it a perfect probe for the search for physics beyond the standard model. The experiment aims at a single-event sensitivity of 3.0×10^{-15} in a running time of 150 days, which is an improvement of a factor of 100 from the current limit measured by the SINDRUM-II experiment. The experiment has been designed in such a way that other processes not predicted by the standard model of physics, such as the transition of a negative muonic atom into a positron, can also be studied. However, this decay can be shadowed by radiative muon capture-induced positrons.

To account for this, analysis procedure has been developed to be able to measure the endpoint of the radiative muon capture photons by COMET Phase-I. The analysis is composed of four distinct steps: a hit filtering and track finding algorithm based on the combination of a gradient-boosted decision tree and a circular Hough transform algorithm; a track fitting algorithm based on Kalman filter technique; and a likelihood analysis to fit the reconstructed photon spectrum. In parallel, the online trigger scheme for the COMET Phase-I main physics measurement has been adapted for the measurement of radiative muon capture photons. A simulation of 10^{11} photons was performed to test the performance of the analysis procedure and the online trigger, as well as to gain a better understanding of the different acceptance of the COMET Phase-I experiment to the radiative muon capture process.

The online trigger specifically adjusted to the radiative muon capture process has shown that it can keep 90% of the radiative muon capture events while rejecting 96% of the background-only events, which reduces the trigger rate down to 4 kHz, a factor of 6 below the critical level for the DAQ of the COMET Phase-I experiment. This analysis procedure has been tested on simulation data. As a result, over the course of 100 days of measurement, the COMET Phase-I experiment will be able to reconstruct approximately 16k radiative muon capture events.

The study has shown that the endpoint spectrum of the radiative muon capture photon for an aluminum target could be estimated with the precision of ± 0.82 MeV which is an improvement of a factor of 2 over the previous measurement performed in TRIUMF. Assuming that the endpoint of the radiative muon capture photon in aluminum is 90.1 MeV as measured by the TRIUMF experiment, the improvement in the measurement of the endpoint spectrum reduces the background contribution of radiative muon capture to $\mu^- + N \to e^+ + N'$ ground state transition by a factor of 10.

Acknowledgements

First and foremost, I would like to express my gratitude to Kuno-sensei for giving me the opportunity to study under him at Osaka University on the COMET experiment. This opportunity has provided me with numerous joyous experiences and aided in the development of the man I am today. I would also like to thank Aoki-sensei for continuing Kuno-sensei's job as my supervisor and for all the constructive comments he gave me through the years. Without him and his advice, I would not have been able to write my thesis.

I would also like to thank the old Kuno laboratory and the Aoki laboratory members (Chen, Itahashi-sensei, Koide-sensei, Sato-sensei, Ueno-sensei, etc.) for all the interesting stories, talks, and parties we shared through the years.

I would like to thank the COMET Collaborators for the many friends I made along the way (Giorgi, Weichao, Andy, Sam, Yu, Matsuda, etc.) that made my studies more enjoyable. I would also like to thank the COMET France collaborators for all the support they gave me and all the interesting discussions and ideas I could test thanks to them (Frederic, Wilfrid, Jean-Claude, Cristina, etc.). I would like to thank the Chinese group, particularly Prof. Yao and Tianyu, who implemented GENFIT within the main framework, which has been essential to my study.

Finally, I would like to thank my family and my wife for their support, which helped me get through the hard times. Merci.

Contents

List of Figures

List of Tables

Chapter 1

Introduction

On the one hand, the Standard Model (SM) of particle physics accurately describes and predicts many phenomena. On the other hand, the SM is unable to explain the observed phenomena such as the existence of dark matter and energy, the matter-antimatter asymmetry of the Universe, and so on. A recent precise measurement of the W boson mass revealed a discrepancy with the value predicted by the SM [1]. Thus, it is important to continue looking for evidence of physics Beyond the SM (BSM) to improve the current models and obtain any hints on how to construct a more complete theory than the SM.

The observation of neutrino oscillations implies that the neutrinos are massive, which contradicts the SM, in which they are massless. To explain the mass of the neutrinos, a minimal extension of the SM and the seesaw model introduces Majorana neutrinos (where particles are their own anti-particles). This poses questions about the nature of the neutrinos themselves: Dirac or Majorana? Furthermore, leptonic mixing, which is similar to quark mixing, has been experimentally confirmed. In the lepton sector, processes involving muons and tauons are particularly interesting because they can be more sensitive to new physics. Additionally, one can now produce a large number of muons, which makes them a good candidate to probe for new physics. This makes the muon particularly interesting for finding new models beyond the SM. This chapter briefly introduces the status of lepton physics via the muon history, its future prospects, and one of its main challenges.

1.1 Lepton flavor and lepton number

The muon was discovered in 1936 as a constituent of cosmic-ray particle showers. Although it was initially misidentified as the pion predicted by Yukawa [2] in 1935, the confusion was later solved when, in 1947, the pion was properly observed [3].

It was then believed to be a heavy version of the electron, so for years, physicists tried to observe the decays of muons to $e\gamma$, $3e$, and $\mu N \to eN$. While the upper limits for searching for such reactions have greatly improved recently (see Figure 1.1), none of those decays have been observed to date.

This led to the creation of conserved quantities in the SM, which are the lepton flavors and the lepton number. Every reaction in the SM should conserve those quantities.

Each lepton flavor has a number associated with them (electrons: L_e, muons: L_μ, and tauons: L_τ). Anti-leptons have a value of -1, while leptons have a value of

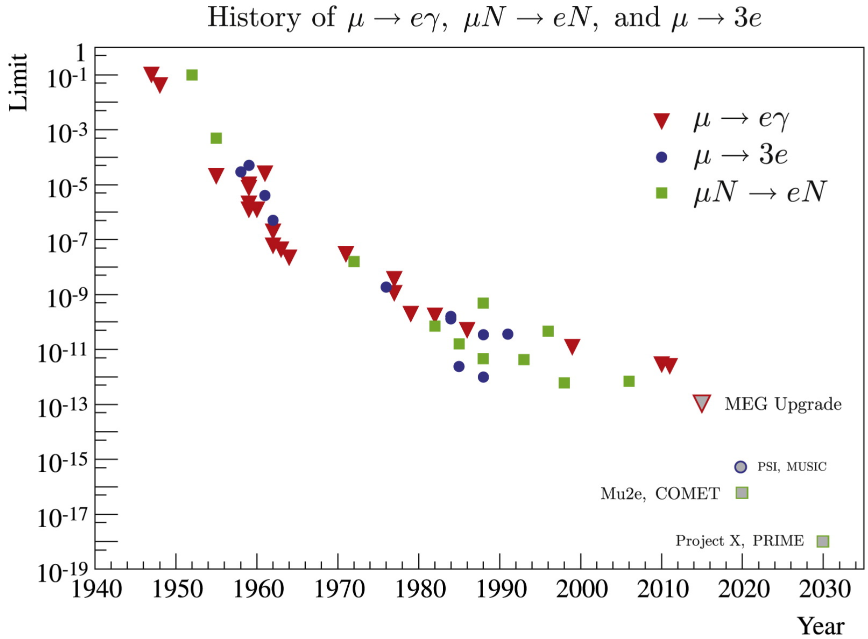

Figure 1.1: Historical search of muon decays and future experiment sensitivity projection of future experiment (MEG update, Mu2e, COMET, Project X and PRIME) [4]

+1. For example, in the muon decay:

$$\mu^- \to e^- + \bar{\nu}_e + \nu_\mu, \tag{1.1}$$

before decaying, the muon flavor number is equal to +1, while the other flavor numbers (electron and tauon) are equal to 0. After the decay, the muon flavor number is also equal to +1 because of the ν_μ. Similarly, the electron and tauon flavor numbers are also conserved.

In addition, the total lepton number L, which can be defined as the addition of the different lepton flavor numbers ($L = L_e + L_\mu + L_\tau$), is conserved in all SM-predicted processes.

However, three articles from two different experiments reported observing neutrino oscillations that violated the lepton flavor number in 1998 [5], 2001 [6], and 2002 [7]. This discovery has two main implications: first, lepton flavors are not conserved. Second, the neutrinos are massive, which means that neutrinos can be Dirac or Majorana ones. In the case of Majorana neutrinos, the lepton number is also not conserved.

1.2 Charged Lepton flavour violation

The branching ratio of decays such as $\mu \to e\gamma$ can be calculated by incorporating the neutrino oscillation into the SM [8][9][10][11]:

$$BR(\mu \to e\gamma) = \frac{3\alpha}{32\pi} \left| \sum_{j=1}^{3} U_{ej} U^*_{\mu j} \frac{m^2_{\nu j}}{M^2_W} \right|^2 \approx \mathcal{O}(10^{-54}), \tag{1.2}$$

where α is the fine structure constant, $m_{\nu j}$ are the mass of the j neutrinos, U_{ij} are the elements of the Pontecorvo-Maki-Nakagawa-Sakata (PMNS) neutrino mixing matrix with $(i, j = 1, 2, 3)$, and M_W is the mass of the W boson.

The branching ratio is suppressed well beyond what can be observed today because of the mass ratios between the neutrino masses and the W boson mass. Thus, any observation of a charged Lepton Flavor Violation (cLFV) process would mean the discovery of physics phenomena beyond the SM. Additionally, many models beyond the SM actually show an enhancement to the cLFV branching ratio, as shown in Table 1.1.

Table 1.1: The size of the observable flavor effect for a variety of BSM SUSY and non-SUSY models. Three stars denote a sizable effect, two stars correspond to a visible effect, and one star indicates no enhancement from the standard model[12]. AC = Abelian U(1) flavour symmetry model [13]; RVV2=non-Abelian model [14]; AKM SU(3) flavour symmetry model [15]; FBMSSM: Flavoud-blind MSSM; LHT: Little Higgs with T-Parity [16], δLL = flavour models with pure CKM-like left handed currents, RS: Randall-Sundrum model with custodial protection [17].

	AC	RVV2	AKM	δLL	FBMSSM	LHT	RS
$D^0 - \bar{D}^0$	★★★	★	★	★	★	★★★	?
ϵ_K	★	★★★	★★★	★	★	★★	★★★
$S_{\psi\phi}$	★★★	★★★	★★★	★	★	★★★	★★★
$S_{\phi K_S}$	★★★	★★	★	★★★	★★★	★	?
$A_{\rm CP}(B \to X_s\gamma)$	★	★	★	★★★	★★★	★	?
$A_{7,8}(B \to K^*\mu^+\mu^-)$	★	★	★	★★★	★★★	★★	?
$A_9(B \to K^*\mu^+\mu^-)$	★	★	★	★	★	★	?
$B \to K^{(*)}\nu\bar{\nu}$	★	★	★	★	★	★	★
$B_s \to \mu^+\mu^-$	★★★	★★★	★★★	★★★	★★★	★	★
$K^+ \to \pi^+\nu\bar{\nu}$	★	★	★	★	★	★★★	★★★
$K_L \to \pi^0\nu\bar{\nu}$	★	★	★	★	★	★★★	★★★
$\mu \to e\gamma$	★★★	★★★	★★★	★★★	★★★	★★★	★★★
$\tau \to \mu\gamma$	★★★	★★★	★	★★★	★★★	★★★	★★★
$\mu + N \to e + N$	★★★	★★★	★★★	★★★	★★★	★★★	★★★
d_n	★★★	★★★	★★★	★★	★★★	★	★★★
d_e	★★★	★★★	★★	★	★★★	★	★★★
$(g-2)_\mu$	★★★	★★★	★★	★★★	★★★	★	?

1.2.1 Coherent muon to electron conversion

Future experiments such as the COherent Muon to Electron Transition (COMET) experiment [18] and Mu2e experiment [19] are focusing their searches on:

$$\mu^- + N(A, Z) \to e^- + N(A, Z), \tag{1.3}$$

where $N(A, Z)$ denotes the nucleus with atomic number Z and mass number A. In muon to electron conversion ($\mu^- \to e^-$ conversion), both the conservations of the electron and muons flavors are violated, but the total lepton number is conserved. In such a reaction, the μ is captured by the nucleus N. Here, the μ is orbiting the atom and forms what is called a "muonic atom". The resultant electron energy, $E_{\mu e}$, from the muon to electron is given:

$$E_{\mu e} = m_\mu - E_N - B_\mu - E_{\text{recoil}}, \tag{1.4}$$

where m_μ is the mass of the muon, E_N is the energy taken by the target nucleus, B_μ is the binding energy of the 1s-state muonic atom, and E_{recoil} denotes the nuclear recoil energy. The rate of the transition to the ground state ($E_N = 0$) is enhanced by a factor of about a number of nucleons in the nucleus, due to coherency, which is induced by the fact that the initial and final nuclei are the same. For the transition to the excited state ($E_N \neq 0$), the rate is relatively suppressed from that to the ground state. In the Ground state (GS) transition, the electrons produced by the transition have a clear mono-energetic signature, which makes it a really interesting process to search for from an experimental perspective.

The COMET experiment [18] and Mu2e [19] measurements will both focus on the search for coherent transitions with an aluminum target. The current best measurements were made by the SINDRUM-II experiment on a Ti target [20] and an Au target [21] with an upper limit at 90% confidence level (CL) of 6.1×10^{-13} and 7×10^{-13} respectively.

1.3 Lepton Number violation: neutrinoless double beta decay

Neutrino oscillations imply that neutrinos have masses; however, the masses of the neutrinos are so small compared to the masses of other particles, and this fact indicates that another mechanism may be needed to generate the neutrino masses. The smallness of the neutrino mass can be explained by the seesaw model, in which at least one heavy Majorana neutrino is introduced. Only the lepton number violation (LNV) experiments are sensitive to the possible Majorana nature of the neutrinos. The neutrinoless double beta decay ($0\nu\beta\beta$) experiment, whose Feynman diagram is shown in Figure 1.2, is currently the most sensitive experiment for LNV. PandaX-III has measured the current limit of $0\nu\beta\beta$, with a lower limit on the half-time of ^{136}Xe of 6.60×10^{27} years [22].

The LNV experiments can probe the Majorana neutrino contribution and provide information on the so-called neutrino effective masses $\langle m \rangle_{l_1,l_2}$:

$$\langle m \rangle_{l_1,l_2} = \sum_k U_{l_1 k} U_{l_2 k} m_k, \tag{1.5}$$

where $l_1, l_2 = e, \mu, \tau$, and $k = 1, 2, 3$. U_{lk} is the PMNS mixing matrix element between the lepton mass and the k^{th} neutrino mass, and m_k are the Majorana masses. The neutrinoless double beta decay process is only sensitive to the ee sector. The current upper limit given by $0\nu\beta\beta$ is $\langle m \rangle_{e,e} \leq 0.33$ eV [23].

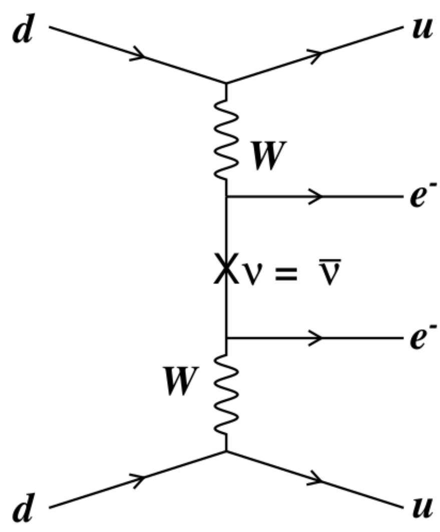

Figure 1.2: Feynman diagram of $0\nu\beta\beta$ in a Majorana neutrino model

1.4 Muon to positron conversion

The neutrinoless double beta decay process is not the only process that can be used to find LNV and thus probe the nature of the neutrino. Muon to positron conversion:

$$\mu^- + N(A, Z) \rightarrow e^+ + N'(A, Z-2), \tag{1.6}$$

is another candidate.

While $0\nu\beta\beta$ is the most sensitive LNV process, it is only sensitive to the *ee*-sector. Furthermore, there is no guarantee that this sector is not heavily suppressed compared to other sectors. For example, the flavor effect has been proposed as a possible enhancement of the rate muon to positron conversion ($\mu^- \rightarrow e^+$ conversion) over $0\nu\beta\beta$ [24]. Furthermore, when compared to the *ee*-sector, other models, which introduce new particles, predict an improvement in the $e\mu$ and $e\tau$ sectors [25][26][27].

1.4.1 Experimental aspect of $\mu^- + N(A, Z) \rightarrow e^+ + N'(A, Z-2)$

On the experimental perspective, $\mu^- \rightarrow e^+$ conversion can be searched in parallel with $\mu^- \rightarrow e^-$ conversion searches at the COMET experiment and the Mu2e experiment, which is an advantage. The energy signature of the positron, $E_{\mu^-e^+}$, can be calculated in the same way as the electron energy from the $\mu^- \rightarrow e^-$ conversion:

$$E_{\mu^-e^+} = m_\mu + M_N - M_{N'} - E_{N'} - B_\mu - E_{\text{recoil}}, \tag{1.7}$$

where M_N is the mass of the initial nucleus and $M_{N'}$ is the mass of the final nucleus in the ground state. Because N and N' are different, there is no enhancement by coherency in the GS transition. The final nucleus can still be produced in its ground state ($E_{N'} = 0$). But it can also be produced in an excited state. Thus, a mixture of both excited and ground state transitions is expected. The study of Divari *et al.*[28] predicts that in ^{27}Al the ratio of GS transition is 41%. For muon capture processes, the nucleus is, on average, left with an excitation energy of 20 MeV [29]. At this energy level, the nuclear structure of the nucleus is well described by the

Table 1.2: Maximum energy of the positron in $\mu^- + N(A,Z) \rightarrow e^+ + N'(A,Z-2)$ for various nucleus.

	$E^{\text{end}}_{\mu^- e^+}$ (MeV)
^{27}Al	92.3
^{40}Ca	103.5
^{48}Ti	98.9
^{58}Ni	104.2

Giant Dipole Resonance (GDR) model [30]. Thus, two transitions were assumed when searching for $\mu^- \rightarrow e^+$ conversion, the GS, and the GDR transitions. Table 1.2 shows the maximum energy of the positron $E^{\text{end}}_{\mu^- e^+}$ for different nucleus targets.

1.4.2 The SINDRUM-II experiment

The current best measurements for $\mu^- \rightarrow e^+$ conversion were performed by the SINDRUM-II experiment, assuming both the GS and GDR transitions. The SINDRUM-II experiment assumed in the GDR model that the energy taken by the nucleus can be modeled by a Lorentzian with a mean energy of 20 MeV and a width of 20 MeV. They measured the current best limit to $\mu^- \rightarrow e^+$ conversion on a titanium target at 1.7×10^{-12} [31] with a 90% CL for the GS model. For the GDR model assumption, they measured the upper limit to be 3.6×10^{-11} with a 90% CL. This give a upper bound on $\langle m \rangle_{e,\mu} \leq 17$ MeV [23]. This makes the $\mu^- \rightarrow e^+$ conversion transition process the most sensitive process to measure $\langle m \rangle_{e,\mu}$, as other similar processes $(K^+ \rightarrow \pi^- e^+ \mu^+)$ currently give a limit at 90 GeV [23].

To measure the $\mu^- \rightarrow e^+$ conversion at higher sensitivity, the background due to Radiative Muon Capture (RMC), which can produce positrons in the same energy region as the $\mu^- \rightarrow e^+$ conversion positron signal, needs to be well known. Figure 1.3 shows the reconstructed positron spectrum by the SINDRUM-II experiment [31]. The gray area positrons have been identified as RMC-induced positrons. The predicted spectrum for $\mu^- \rightarrow e^+$ conversion is shown, assuming GS and GDR transitions. In this figure, one can see the importance of constraining the RMC positron tail to improve the measurement of $\mu^- \rightarrow e^+$ conversion as around half of the GDR spectrum overlaps with the RMC positron spectrum.

1.5 Radiative muon capture process

The radiative muon capture process is given by:

$$\mu^- + N(A,Z) \rightarrow N(A,Z-1) + \nu_\mu + \gamma. \tag{1.8}$$

The γ can then undergo internal or external conversion, producing a positron-electron pair, obstructing the measurement of $\mu^- \rightarrow e^+$ conversion. Three theoretical approaches have been used to describe the RMC γ spectrum:

- perturbation theory from Feynman diagrams [32] [33] [34],
- application of Low's theorem [35] of soft photon [36] [37] [38], and

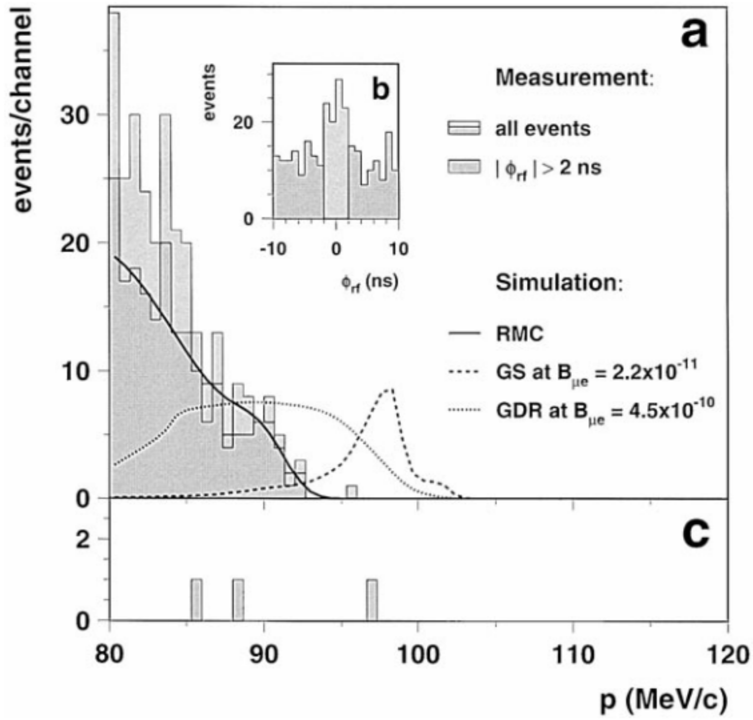

Figure 1.3: Reconstructed positron spectrum by the SINDRUM-II experiment with a titanium target overlap with simulation results [31]

- construction of elementary RMC amplitude from current conservation laws called Hwang-Primakoff closure approximation [39] [40].

The three models have showed similar results. However, the Hwang-Primakoff closure approximation is usually used because of its generalization to different nuclei. The model assumes that using the mean excitation energy, the sum of the nucleus final states can be approximated with a single nuclear transition. The resultant photon spectrum can be expressed as a 5th degree polynomial [38]:

$$\frac{dN}{dE} = \frac{e^2}{\pi}\frac{k_{\max}^2}{m_\mu^2}(1 - \frac{N-Z}{A})(1 - x + 2x^2)x(1-x)^2, \tag{1.9}$$

where E is the photon energy, $k_{\max}$ is the energy spectrum endpoint, $(N-Z)/A$ is the neutron excess in the nucleus, and x is given by $E/k_{\max}$. The only unknow is $k_{\max}$, which theoretically has a limit given by:

$$E_{\text{RMC}}^{\text{end}} = m_\mu + M(A,Z) - M(A,Z-1) - B_\mu - E_{\text{recoil}}, \tag{1.10}$$

where m_μ is the muon mass, $M(A,Z)$ is the initial nucleus mass, $M(A,Z-1)$ is the final nucleus mass at rest, B_μ is the muonic atom binding energy, and E_{recoil} is the final nucleus recoil energy. According to the measurements done by previous experiment $k_{\max}$ is 5—10 MeV below the maximum allowed energy $E_{\text{RMC}}^{\text{end}}$ [41] [42] [43]. Table 1.3 shows, for various nuclei, $k_{\max}$ measurement, the partial branching ratio where the photon has an energy E_γ greater than 57 MeV R_γ, and the maximum allowed photon energy.

Table 1.3: Previous RMC measurement results

	R_γ (10^{-5})	k_{max} (MeV)	$E_{\text{RMC}}^{\text{end}}$ (MeV)	Experiment
^{27}Al	1.40 ± 0.11	90.1 ± 1.8	101.84	TRIUMF [43]
^{40}Ca	2.09 ± 0.19	93 ± 2	102.57	TRIUMF [41]
^{48}Ti	1.30 ± 0.12	89.2 ± 2	99.68	TRIUMF [43]
^{58}Ni	1.48 ± 0.08	92 ± 2	102.46	TRIUMF [42]
^{197}Au	NA	88 ± 0.6	94.3	SINDRUM II [21]

1.5.1 The TRIUMF experiment

Figure 1.4 shows a schematic view of the TRIUMF RMC detector [44]. The main goal of the TRIUMF experiment was to measure the partial branching ratio of RMC. In most models [45][46][47], the branching ratio of RMC is linked to the g_P/g_A by using the partially conserved axial current (PCAC) hypothesis, where g_P is the pseudo scalar coupling and g_A is the axial coupling induced by the weak force. Thus, by measuring the RMC partial branching ratio on multiple target the PCAC hypothesis could be tested. The TRIUMF experiment, thus, measured the RMC spectrum for different targets, including ^{27}Al.

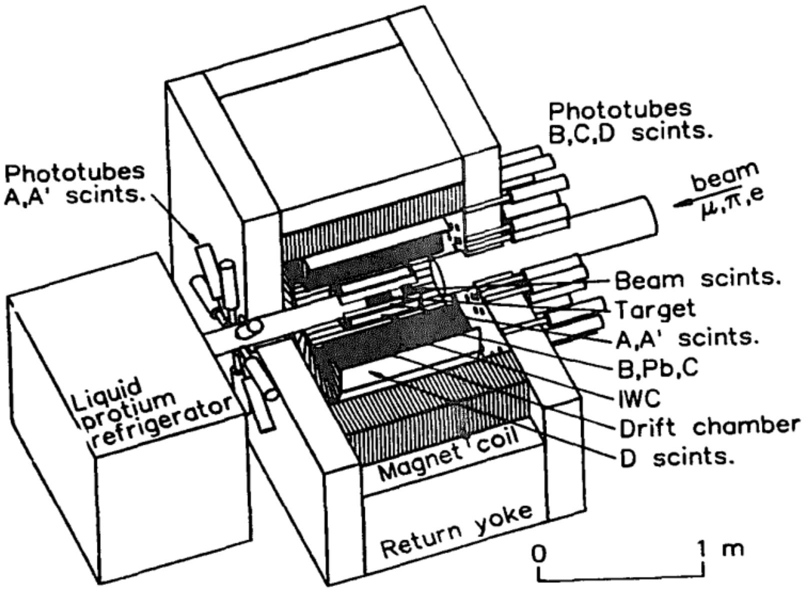

Figure 1.4: Sketch of TRIUMF RMC detector [43]

The ^{27}Al RMC spectrum reconstructed by the TRIUMF experiment is shown in Figure 1.5. This spectrum was obtained by measuring 3051 photons with an energy superior to 57 MeV. For different values of k_{max}, the spectrum was fitted using the Primakoff approximation model. The statistical error at 1σ of the fit is given by $\Delta\chi^2 = 1$. The TRIUMF experiment, on the other hand, consistently overestimated statistical uncertainty by defining it as $\Delta\chi^2/NDF = 1$, where NDF is the degree of freedom. As a result, the TRIUMF experiment statistical error has been overestimated by a factor of $\sqrt{NDF}$ [1]. The systematic uncertainty of k_{max}

[1] Assuming that the fitting has been done with NDF = 40, as shown in Figure 1.4, the statistical error is around 0.3-0.4 MeV. The analysis presented in this thesis has been performed assuming the same number of events, which has shown consistent results.

has not been evaluated. In this thesis, the overestimated statistical uncertainty of TRIUMF will be used as the current precision to the value of $k_{\max}$ for ^{27}Al.

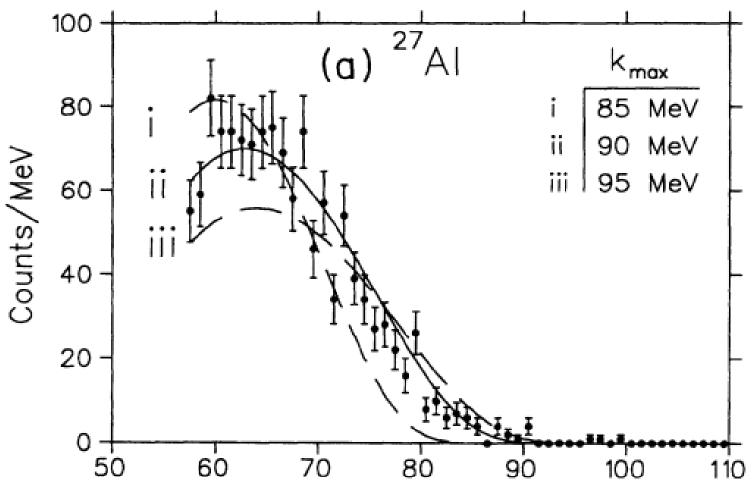

Figure 1.5: Reconstructed photon spectrum by the TRIUMF experiment with an ^{27}Al target. Solid circles are showing the measured events and the lines are showing spectrum fitting results using Primakoff model for different values of $k_{\max}$ [43]

1.5.2 Expected reconstructed positron spectrum in the COMET Phase-I experiment

The positron spectrum that will be measured in the COMET Phase-I experiment can be predicted using Table 1.3. The results are shown in Figure 1.6. In the case of a 1.7 MeV error in the measurement of $k_{\max}$, as in the TRIUMF experiment, the COMET Phase-I experiment cannot increase the upper limit of the measurement of $\mu^- \to e^+$ conversion to a precision 100 times greater than the previous measurement as the endtail of the RMC spectrum overlaps with the mono-energetic positron maximum momentum (92.3 MeV) for muonic aluminum atoms. However, the gap between the RMC spectrum without error and the RMC spectrum with an error of 1.7 MeV is sufficiently large so that measuring $k_{\max}$ at higher precision may make the measurement of $\mu^- \to e^+$ conversion$^{\mathrm{GS}}$ possible at a branching ratio $B_{\mu e} = 1.7 \times 10^{-14}$. It would be noted that improving the measurement of the $\mu^- \to e^+$ conversion$^{\mathrm{GDR}}$ spectrum with an aluminum target is difficult, as the major part of the spectrum is hidden by the RMC-induced positron spectrum.

1.5.3 Limit of the Hwang-Primakoff closure approximation model

While the Hwang-Primakoff closure approximation model predicts that no photon with energy greater than $k_{\max}$ will exist, nothing prevents it from occurring as long as its energy is less than the maximum allowed energy. An excess of positrons was measured near the endtail of the RMC spectrum in the SINDRUM-II experiment[21], as shown in Figure 1.7. However, Mackenzie and Murat [48] strongly refute the possibility of the observation of $\mu^- \to e^+$ conversion, and instead point out to a possible exclusive radiative muon capture channel that may change the positron spectrum near the kinematic endpoint of the RMC spectrum, hinting at the need for a more precise measurement of the RMC endtail spectrum.

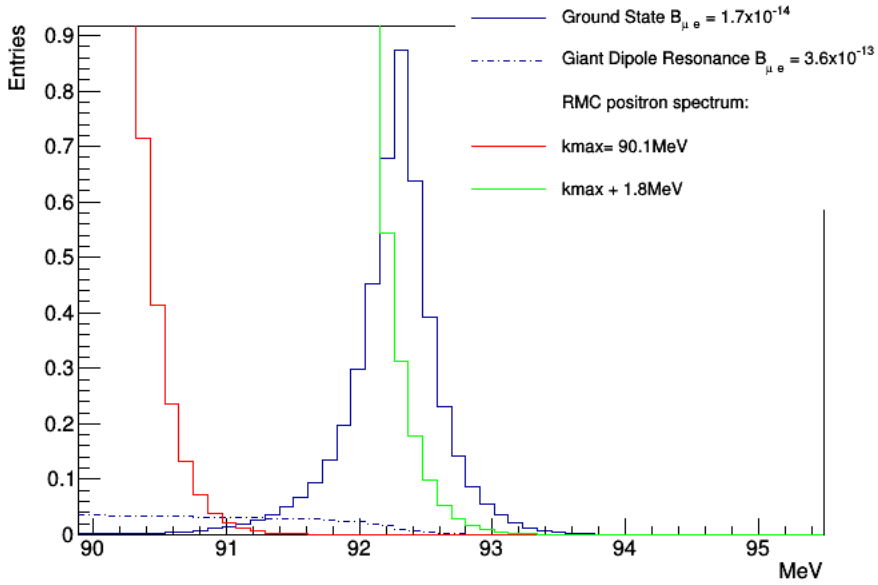

Figure 1.6: The expected reconstructed positron spectrum in the COMET Phase-I experiment. Calculation details are explained in chapter 11

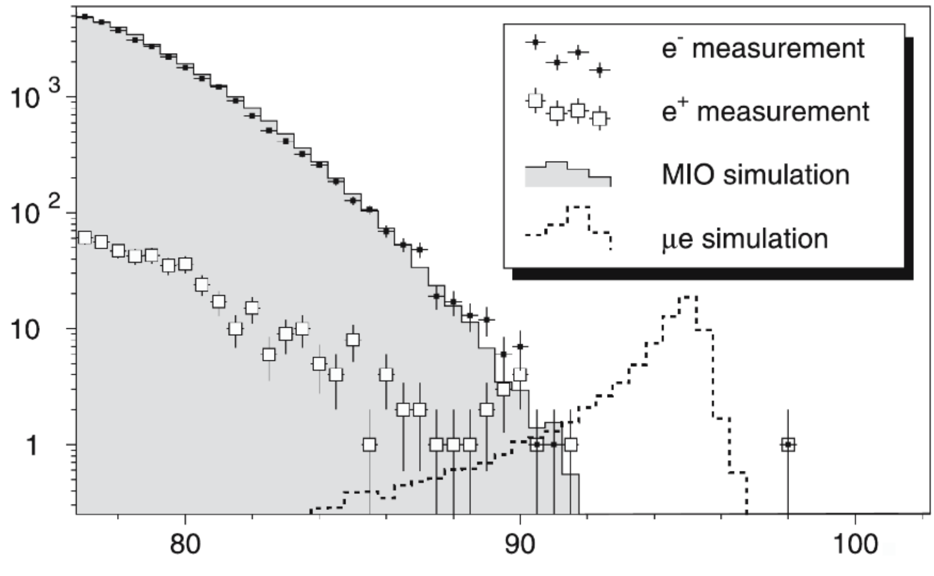

Figure 1.7: SINDRUM-II experiment e^- and e^+ spectra on an ^{197}Au target [21].

Future experiments, such as the COMET and Mu2E experiments, will need to precisely measure the end-tail spectrum of RMC to improve $\mu^- \to e^+$ conversion precision. For this purpose, this thesis focuses on building a procedure to measure the RMC γ spectrum endpoint within the Primakoff approximation model and to estimate the uncertainty of the measurement for the COMET Phase-I experiment.

Chapter 2

The COMET Phase-I experiment

The COMET experiment at the Japan Proton Accelerator Research Complex (J-PARC) aims to search for the neutrinoless coherent transition of a muon in a muonic atom into an electron. The goal is to measure $\mu^- \to e^-$ conversion at a Single Event Sensitivity (SES) of 2.6×10^{-17} [18]. For that, the experiment is staged into two phases: the COMET Phase-I experiment and the COMET Phase-II experiment.

The COMET Phase-I experiment aims for a search of $\mu^- \to e^-$ conversion in a nuclear field at a SES of 3.1×10^{-15}, which is roughly a factor 100 better than the current experimental upper limit set by the SYNDRUM-II experiment at PSI [21]. It will also be a preparation for COMET Phase-II experiment by inspecting the new muon beam line. A layout of the COMET Phase-I experiment is shown in Figure 2.1.

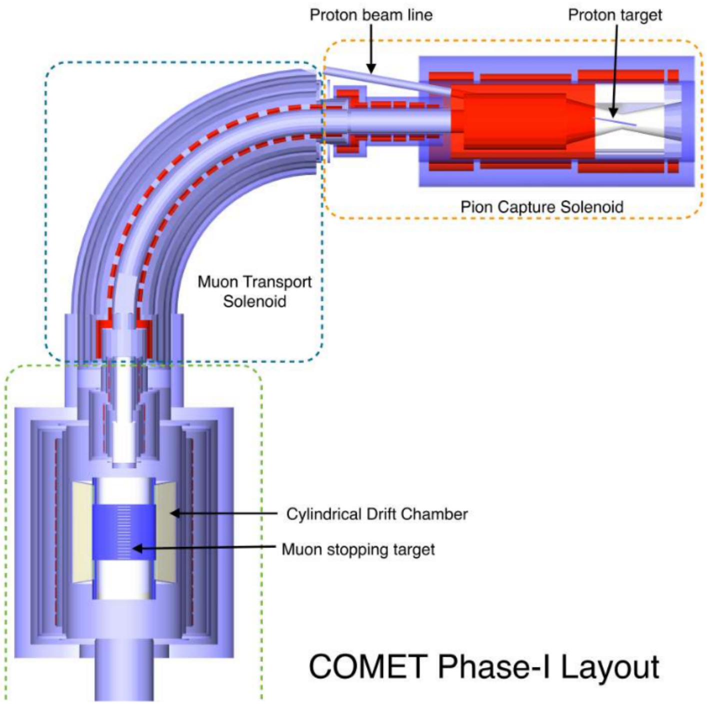

Figure 2.1: Layout of the COMET Phase-I experiment[18]

This chapter first introduces the background to the COMET Phase-I experiment main physic search, and then the COMET Phase-I experimental apparatus is introduced with an emphasis on the countermeasure to the main physic background.

2.1 The COMET experiment main backgrounds

The COMET Phase-I experiment has been cleverly designed to work around the two main backgrounds to the measurement of $\mu^- \to e^-$ conversion, which are:

- Radiative Pion Capture (RPC),
- and muon Decay In Orbit (DIO) electrons.

2.1.1 Radiative pion capture

The muon beam is made from the decay of pions. However, all the pions in the beam may not decay, and once the surviving pions are captured by the muon stopping target, the created pionic atoms can undergo RPC reaction:

$$\pi^- + N(A, Z) \to \gamma + N(A, Z - 1). \tag{2.1}$$

The energy of the photon can go over 120 MeV, which can produce electrons of 105 MeV by compton scattering or by electron-positron pair creation. To effectively suppress this background, the COMET experiment is using two techniques that are both based on the short pion lifetime (26 ns):

- a large distance separating the proton target, where the pions are created, from the muon stopping target, and
- a pulse beam coupled with a delayed measurement window.

2.1.2 Muon decay in orbit electrons

The DIO:

$$\mu^- + N \to e^- + \bar{\nu}_e + \nu_\mu + N, \tag{2.2}$$

is one of the main decay channel of muons stopped in the target. The resultant electron can have an energy greater than half of the muon mass due to the nuclear target absorbing the recoiled momentum and shifting the possible electron energy up from the free muon decay [49]. The spectrum of the electrons is shown in Figure 2.2. The tail electrons (105 MeV range) are highly suppressed, however, a large number of stopped muons are expected, which balance out the suppression. Thus, the COMET Phase-I experiment expects to see DIO electrons in this energy region. To avoid background contamination from DIO electrons, a resolution of 200 keV/c for the 105 MeV/c electrons is required to achieve the sensitivity of the COMET Phase-I experiment. At this precision, the resolution is dominated by multiple-scattering, so it is imperative that the detector density be as low as possible.

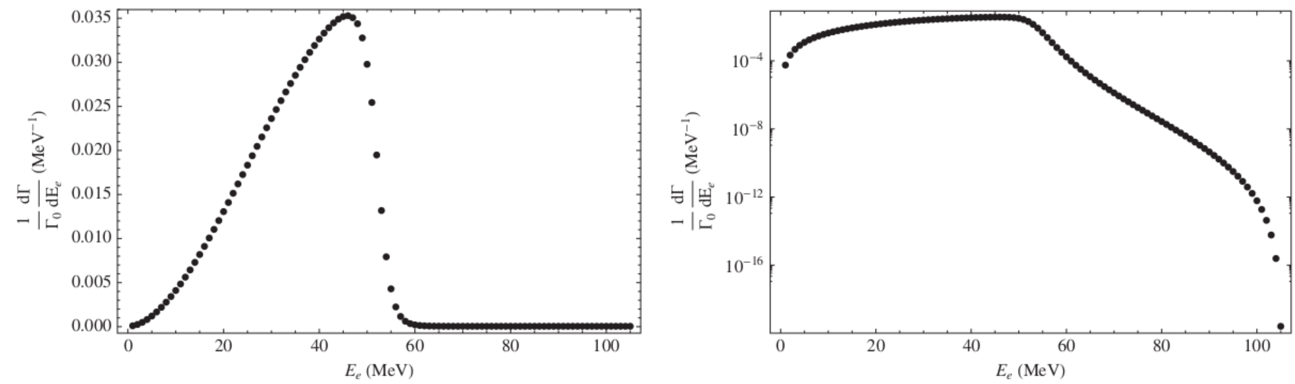

Figure 2.2: DIO electron spectrum for calculated for ^{27}Al [49]

2.2 The COMET Phase-I experimental apparatus

The COMET Phase-I experiment can be separated into 3 parts:

- the proton beamline,
- the muon beamline and
- the cylindrical detector system.

2.2.1 Proton beamline

Figure 2.3 shows the J-PARC accelerator complex in which the COMET experiment will be conducted. Protons are accelerated to 400 MeV by a LINear ACcelerator (LINAC). They are then accelerated by the Rapid Cycling Synchroton (RCS) to reach an energy of 3 GeV. The Main Ring (MR) then accelerates them to 8 GeV. They are then redirected through the Hadron hall where the COMET experiment is located. The pion production cross section is correlated with the energy of the proton [50], at higher beam energy, the creation of pion increases; however, at high beam energy, the production of antiprotons, which create backgrounds by their annihilation, also increases [51]. Thus, as a compromise, the beam power is chosen at 8 GeV.

The proton beam is made of bunches, i.e., clusters of protons, with a time length of 100 ns. Each bunch is separated by 1.2 μs. Combined with a delayed measurement, the pulse beam helps to further suppress the possible background due to RPC. Figure 2.4 shows how to make a beam separation of 1.17 μs by filling protons in every other proton beam bucket.

Any issue could cause protons to leak between bunches, increasing background contamination of RPC to $\mu^- \to e^-$ conversion measurement. The fraction of protons leaked is expressed by the proton beam extinction factor $R_{\text{extinction}}$:

$$R_{extinction} = \frac{N(\text{leakage protons})}{N(\text{protons per bunch})}. \tag{2.3}$$

To achieve its goal sensitivity on the measure of $\mu^- \to e^-$ conversion, the $R_{\text{extinction}}$ should be as low as 10^{-10} for COMET Phase-I [18].

Figure 2.3: J-PARC

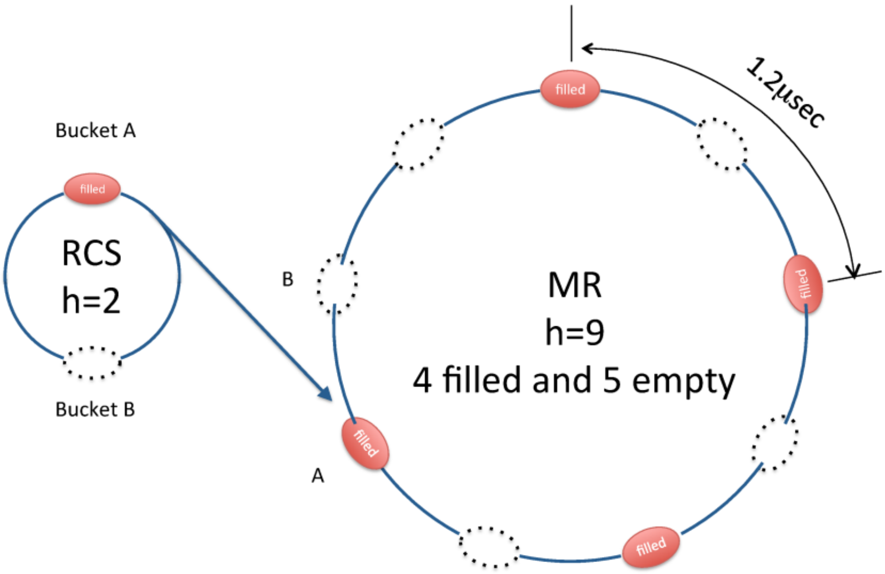

Figure 2.4: The COMET pulse beam layout [18]. The bunches are separated by 1.17 μs by filling protons in every other proton beam bucket.

2.2.2 Muon beamline

The 8 GeV proton beamline is directed at the proton target, which has been designed to maximize the production of negative pions.

The negative pions produced are then redirected to the muon transport section. The muon transport is used to:

- let the remaining pions decay — the length of the muon beam transport is of around 7.6 m, as shown in Figure 2.5; and

- select the particles momentum — select muons with a momentum of around 40 MeV/c and eliminiate high energy muons ($p_\mu > 75$ MeV/c) to avoid backgrounds from muon decays in flight.

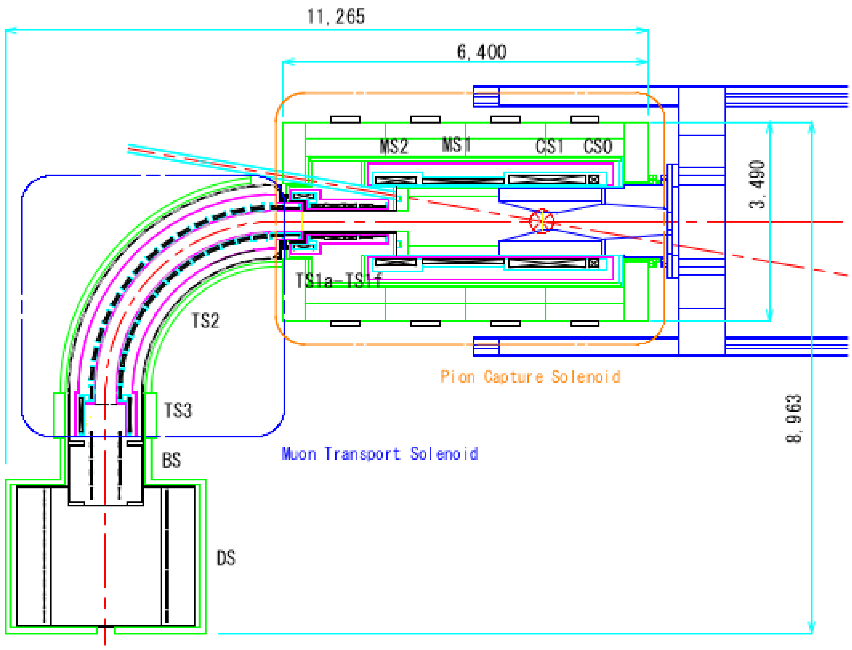

Figure 2.5: Layout of the COMET Phase-I Experiment [18]. The proportion of the different part are shown in m

2.2.3 Cylindrical Detector System

The Cylindrical Detector System (CyDet) is shown in Figure 2.6. It is composed of three different parts:

- the muon stopping target,
- the cylindrical drift chamber and
- the CyDet trigger hodoscope.

Muon stopping target

The muon beam is then directed toward the muon stopping target. The muon stopping target is placed in a bore of 1 T in the detector region. It is made up of 17 aluminum disks with a radius of 100 mm and a thickness of 200 μm spaced by 50 mm from each other. The design has been made to maximize the stopping rate of muons and limit the energy loss of the 105 MeV signal electron. Figure 2.7 shows a mock-up muon stopping target.

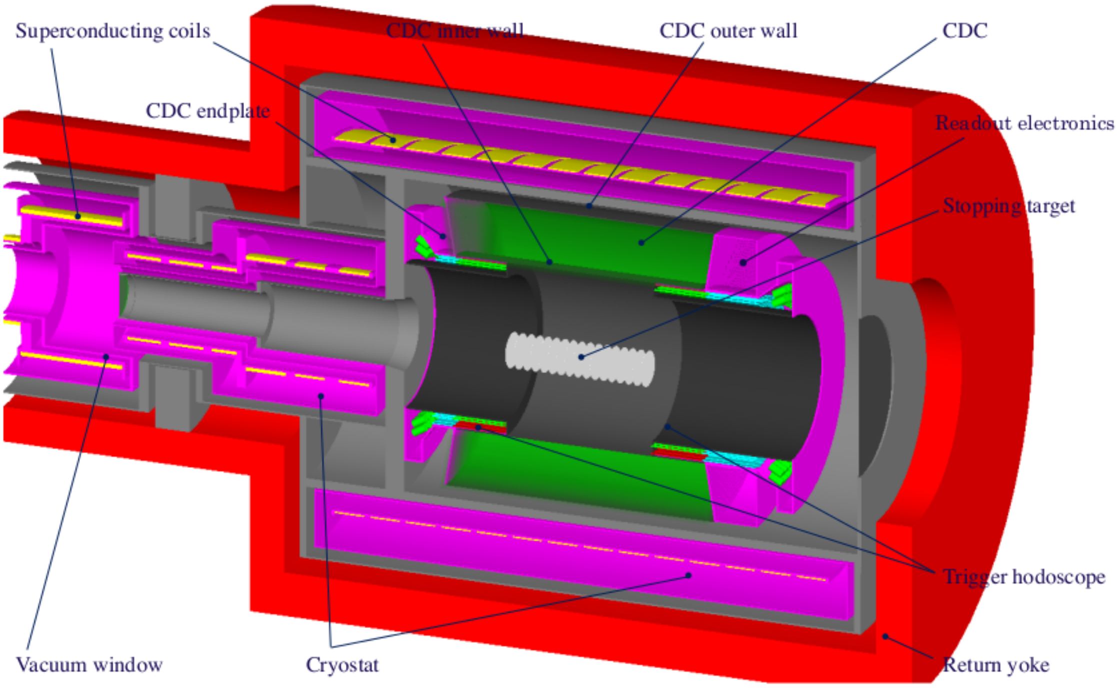

Figure 2.6: Schematic layout of the CyDet [18]

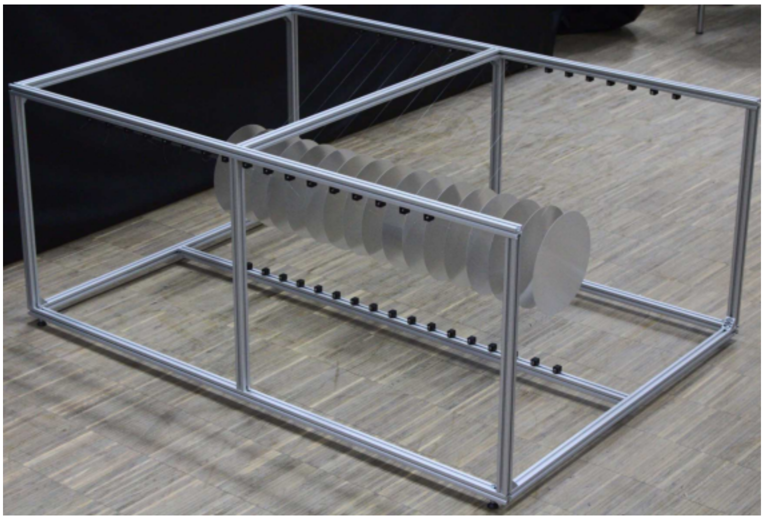

Figure 2.7: A mock-up muon stopping target [18]

Measurement time window Figure 2.8 shows the relationship between the timing of the proton pulse, the beam flash with the negative pion contribution, and the electrons from stopped muons with a wide measurement time window.

Pions can be stopped in the muon stopping target, which can create backgrounds due to RPC photons. The creation of the pions and the arrival of particles in the detector region are separated by 180 ns. The lifetimes of pionic aluminum (< 1 ns) and muonic aluminum (864 ns) differ significantly. The measurement time window is set to only work between 700 ns and 1170 ns, in which the chance of prompt beam-related pions surviving is highly suppressed due to the pion short life time.

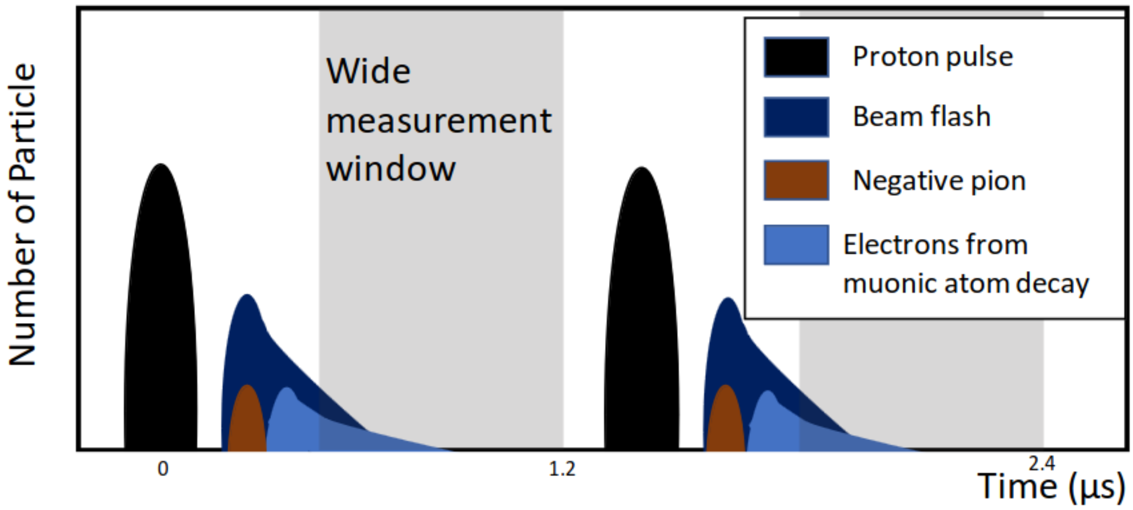

Figure 2.8: Sketch of the relation between the proton pulse, the beam flash (negative pion) and the electrons from the muonic atom decays with the trigger window.

The cylindrical drift chamber

The main detector is a cylindrical drift chamber (CDC) that surrounds the muon stopping target. The detector is submerged in a 1 T magnetic field, and with the distance between the detector and the muon stopping target, the rate of low-energy charged particles reaching the detector is greatly reduced.

The CDC is arranged in 20 concentric sense layers with alternating positive and negative stereo angles. The first and twentieth layers act as guard layers. Each cell has one sense wire surrounded by an almost-square grid of 8 field wires. A high voltage is applied to the sense wire while the field wires are at ground potential, creating an electric field inside the cell. The cell size is 16.8 mm and 16 mm in height. The stereo angle is set to 64-75 mrad to achieve a longitudinal spatial resolution of about 3 mm. Figure 2.9 shows a typical cell with typical drift lines assuming a magnetic field of 1 T.

When a charged particle passes through one cell, it ionizes the gas and produces primary electrons and ions. The primary electrons feel the electric field between the field and sense wire and are thus drifting to the sense wire, while the ion slowly drift toward the field wire. Once the electrons are close to the sense wire, an electron avalanche occurs, with each electron producing more electron-ion pairs. The flow of the electrons and ions produced by the avalanche induces a current on the sense wire. The CDC is measuring this current. The time between the primary electrons and the induce current on the sense wire is called "drift time". It is the time it takes for the primary electron to reach the sense wire. Knowing the drift time, one can calculate the drift distance. The drift distance precision characterizes the CDC performance.

The inner wall of the CDC is made of a 0.5 mm thick carbon-fiber-reinforced polymer (CFRP). Thin aluminum foils (0.05 mm) are stuck inside it to eliminate charge-up on the CFRP. The inner wall is as thin as possible to lower energy loss from the 105 MeV electron when entering the detector and thus increase the signal acceptance.

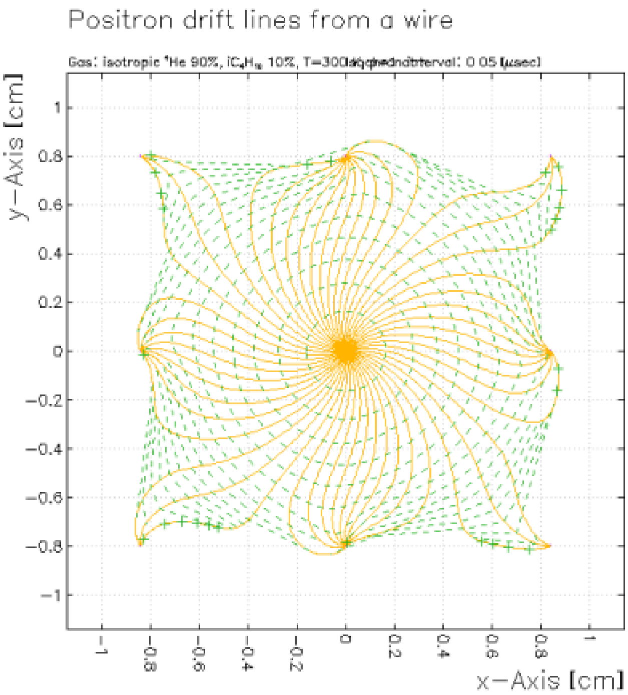

Figure 2.9: Typical drift lines for the CDC cell under a 1 T magnetic field from a Garfield simulation [18]

The main parameters of the Cylindrical Drift Chamber (CDC) are listed in the table 2.1.

The CyDet trigger hodoscope

The COMET Phase-I experiment uses a two-level trigger strategy. The CyDet Trigger Hodoscope (CTH) is used in the first level trigger. The second level trigger, called the online trigger, uses the CDC hit information as described in chapter 5.

The CTH is composed of two hodoscope components placed at both ends of the CDC. A quater of a hodoscope ring is shown in Figure 2.10. Each hodoscope is made up of 48 modules, which are composed of a plastic scintillator and a lucite Cherenkov counter. The plastic scintillator and the lucite Cherenkov counter of each module are separated by a few centimeters. The modules are rotated by an angle of 20 degrees tangent to the concentric circles so that a four-fold coincidence can be made with a high acceptance for $\mu^- \to e^-$ conversion signal electrons while reducing the fake trigger caused by γ-rays. These γ-rays are produced by delayed muon decays. To further reduce fake triggers from these γ-rays, a lead layer has been added.

Table 2.1: Main parameters of the CDC [18]

Inner wall 1	Length	1495.5 mm
	Radius	496.0-496.5 mm
	Thickness	0.5mm
	Material	CFRP
Inner wall 2	Length	1495.5 mm
	Radius	496.5-496.55 mm
	Thickness	0.05mm
	Material	Al
Number of sense layers		20 (including two guard layers)
Sense wire	Material	Au-plated W
	Diameter	25 µm
	Number of wires	4986
Field wire	Material	Al
	Diameter	126 µm
	Number of wires	14562
Gas	Mixture	He:i-C4H10 (90:10)
	Volume	2084 L

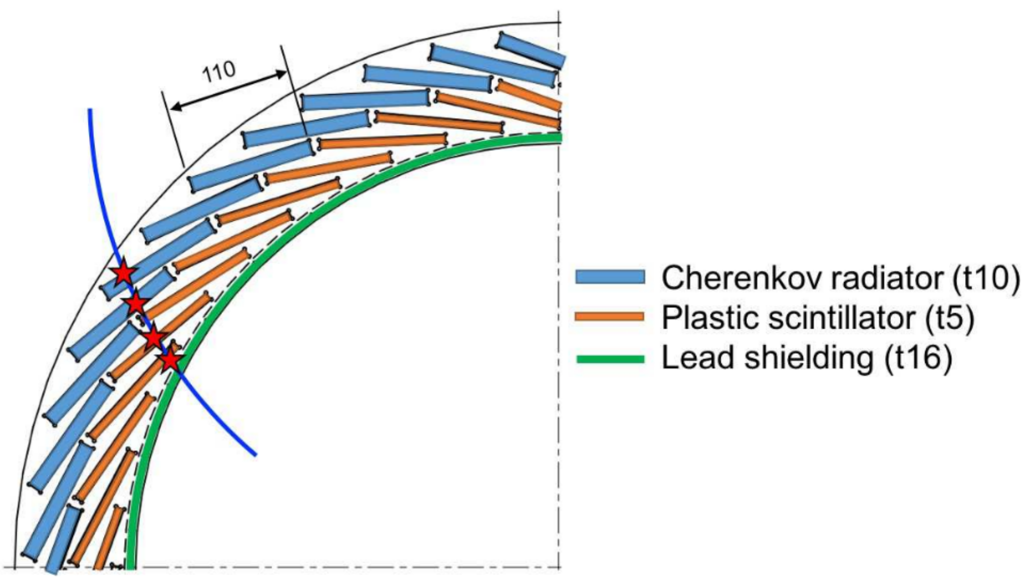

Figure 2.10: Layout of a hodoscope ring with the example of a 4-fold coincidence [18]

Chapter 3

Radiative muon capture γ measurement scheme

This chapter describes how the γ spectrum of radiative muon capture, in parallel with the main physics goal, can be measured in the COMET Phase-I experiment.

3.1 Mesuring scheme

The photon energy cannot be directly measured with the experimental apparatus of the COMET Phase-I experiment, but fortunately the photon can convert into an electron-positron pair:

$$\gamma + N \rightarrow N + e^{+} + e^{-}, \tag{3.1}$$

where N is a nucleus with which the photon interacts. Due to the energy and momentum conservation principle, this reaction can only happen in matter.

As shown by Figure 3.1, the photon conversion can occur in:

- the muon stopping target,
- within the CDC, and
- within the CDC inner wall.

The photon energy is reconstructed using the momenta of the electron and the positron measured by the CDC. In the case of a conversion in the muon stopping target, both the electron and positron are unlikely to reach the CDC due to their limited energy combined with the magnetic field of 1 Tesla. For conversion inside the CDC, there are two problems. First, the CDC density is low, which does not yield a high number of conversions. Second, conversions happening deep inside the detector cannot trigger the CTH, which is attached to the CDC inner wall, and thus there is no data acquisition. Only conversion in the inner wall would be usable in the COMET Phase-I experiment.

Thus, only photons converted inside the inner wall of the CDC, where either the electron or the positron trigger the CTH are considered in this study, as illustrated in Figure 3.2. The figure also defines the XYZ coordinate system that will be used throughout this thesis. The point O(0,0,0) corresponds to the middle of the chamber. The inner wall is composed of two thin layers: a graphite layer of 0.5 mm and an aluminum layer of 0.05 mm; it has been designed to be as thin as possible

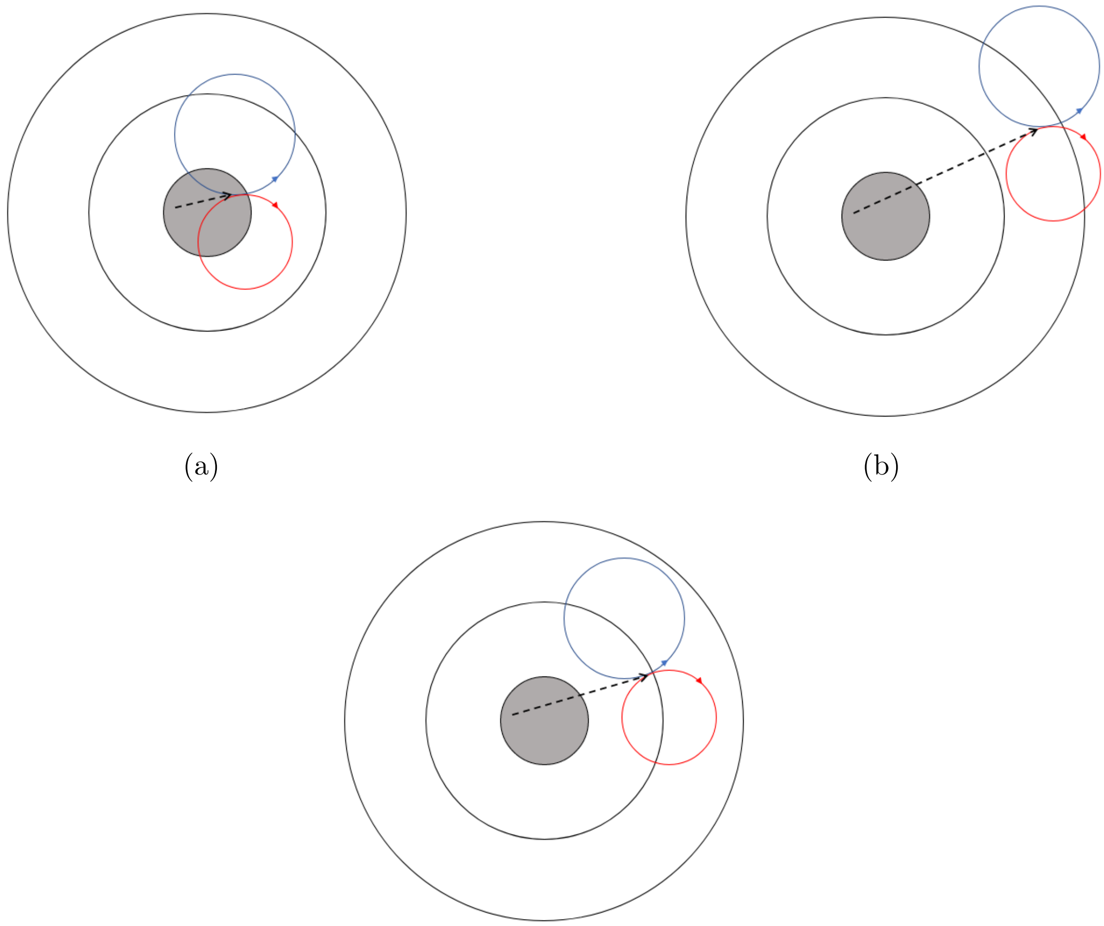

(a) (b) (c)

Figure 3.1: Sketch of a photon (dash line) converting into an electron (blue) and positron (red) pair in (a) the muon target, (b) deep within the CDC, and (c) within the CDC inner wall.

to reduce the energy loss of electrons from $\mu^- \to e^-$ conversion before entering the detector. According to the simulation shown in chapter 4, for photons with energies ranging from 60 to 100 MeV, the ratio of photons that pass through and are converted in the inner wall is around 0.13%. The expected number of events is greatly reduced because of this design.

3.2 Analysis procedure

The analysis procedure that reconstructs the energy of the electron and the positron from the RMC-induced photon conversion is separated into 3 steps:

- denoising,
- track finding, and
- track fitting.

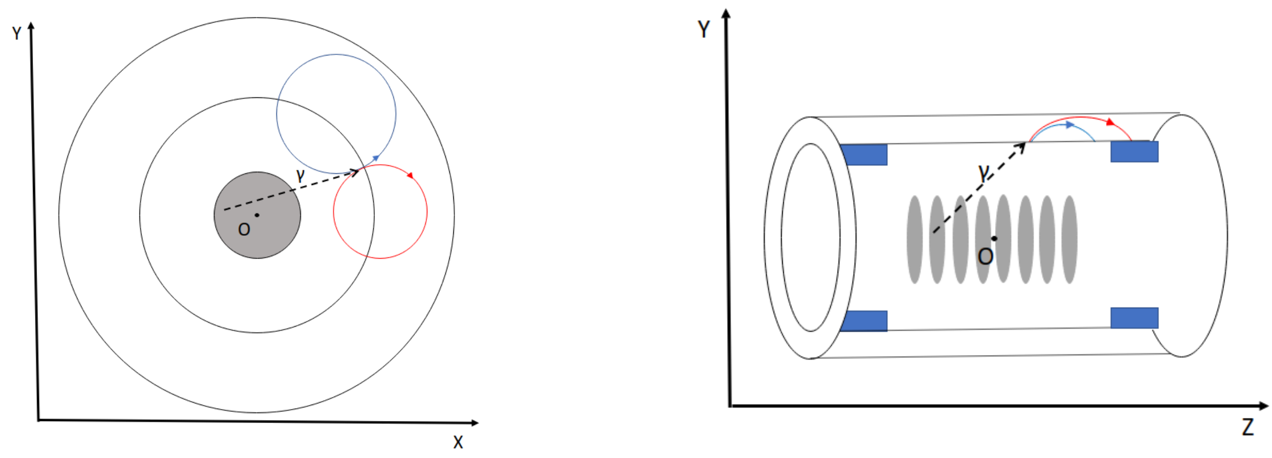

(a) (b)

Figure 3.2: Sketch of a photon (dash line) converting into an electron (blue) and positron (red) pair in the CDC inner wall in (a) XY plane and (b) YZ plane.

3.2.1 Denoising

The COMET experiment is a high-intensity experiment, so a large number of background hits are expected. To quantify the background in the CDC, one can use the background hit occupancy:

$$O = \frac{N_h}{N_w} \tag{3.2}$$

where N_h is the number of sense wires with at least 1 hit, N_w is the total number of sense wires. Simulations have evaluated the background occupancy in the CDC to be around $(41.5 \pm 2.3)\%$ [52].

A simple track finding algorithm, such as the circular Hough transform, cannot work at such a high hit occupancy level. Thus, a denoising step is used to solve this problem. The goal of denoising is to reject as many background hits as possible while keeping as many signal hits as possible.

Figure 3.3 shows a typical event display before and after the denoising step. The details of the denoising are shown in Ch. 6.

3.2.2 Track finding

The track finding has three functions:

- removing more background hits,
- separating positron and electron hits, and
- providing the initial parameters for the track fitting.

Due to the 1 T magnetic field applied in the CDC region, charged particles draw a helical trajectory in the CDC. These helical trajectories show circles in the two-dimensional projection onto the plane perpendicular to the CDC axis. Thus, to recover the electron and positron trajectories, one can use a simple circle finding algorithm in the X-Y projected plane, such as the circular Hough transform, which is commonly used for finding circles in images [53]. Figure 3.4, shows a typical RMC event produced by the Monte Carlo simulation, where the photon converts into the inner wall. The hits appear to follow a circular trajectory.

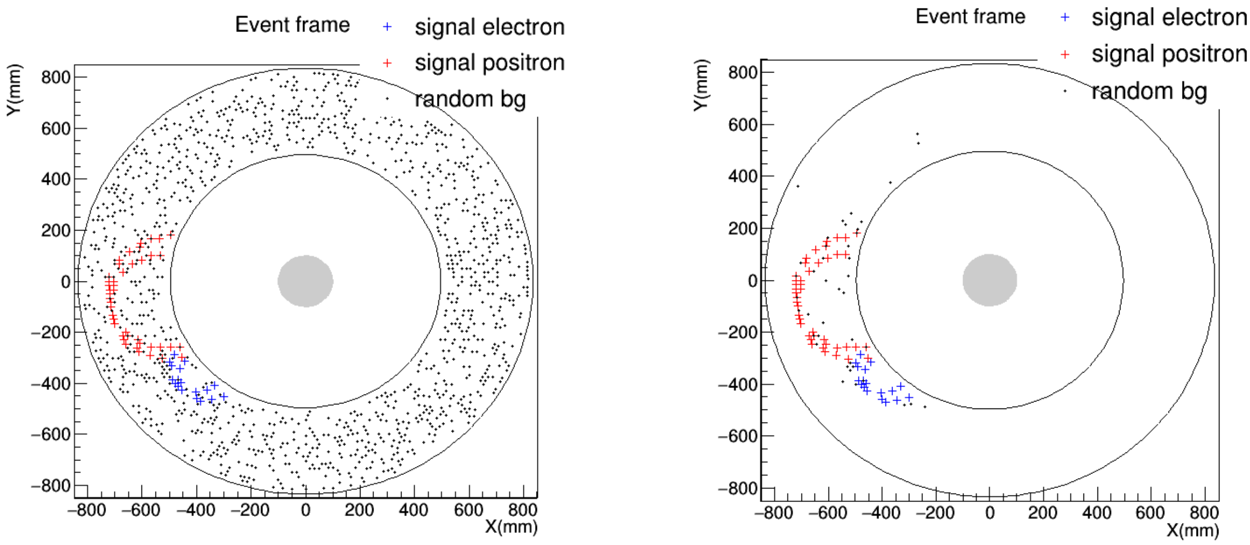

(a) (b)

Figure 3.3: Event frame before denoising (a) and after denoising (b). The background has been generated uniformly across the sensing wires with an occupancy of 45%.

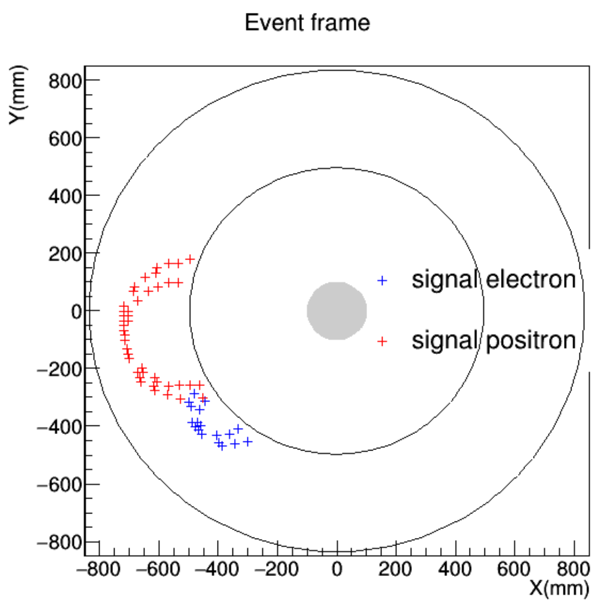

Figure 3.4: Typycal RMC event projected in the XY plane coordinate. The hit position shows the wire position in the middle of the CDC.

3.2.3 Track fitting

The goal of the track fitting is to reconstruct the trajectories of the electron and positron as precisely as possible to calculate their momenta. Two helices are fitted to accomplish this: one for the electron and one for the positron. The helix fitting uses the result of the track finding procedure already described as a first guess, also called a "seed". From the seed, the fitting is adjusting the track to fit the drift distance circles; thus, in the transversale (XY) plane, the goal is to find a circle that is tangent to all the drift distance circles. Figure 3.5 shows a sketch of an electron track in the transverse plane, the sense wires hit, and the drift distance circle associated with the hit.

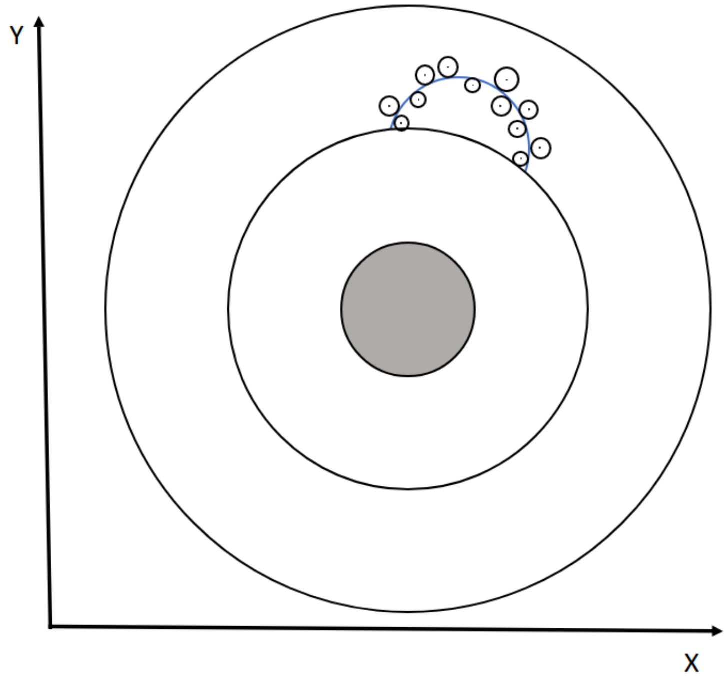

Figure 3.5: Sketch of an electron track in the CDC transversale plane. Wire positions are shown by a black point, and are surrounded by a black circle showing the drift distance circles.

The fitting is performed using Kalman filter techniques [54]. The details of the fitting are explained in Ch. 7.

3.3 Expected RMC events

To estimate the sensitivity of the COMET Phase-I experiment to RMC, the number of expected events needs to be evaluated. The number of expected events is:

$$\begin{aligned} N_{\text{expected}} = & Y_\mu \times f_{\text{cap}} \times R_{\text{time}} \times R_\gamma \times A_{\text{conv}} \\ & \times A_{\text{geom}} \times A_{\text{MTW}} \times A_{\text{online}} \times \epsilon_{\text{analysis}}, \end{aligned} \tag{3.3}$$

where Y_μ is the expected muon yield, f_{cap} is the fraction muon stoped that are captured by the target nucleus, R_{time} is the running time of the experiment, A_{conv} is the conversion rate of photon in the CDC innerwall, A_{geom} is the geometrical acceptance, A_{MTW} is the measurement time window acceptance, A_{online} is the online trigger acceptance, and $\epsilon_{\text{analysis}}$ is the analysis procedure efficiency. The acceptances and the efficiency are not known, so to estimate the number of expected events, they need to be evaluated. To evaluate these acceptances, a Monte Carlo simulation was performed.

The physics motivations behind the measurement of the RMC spectrum were introduced in Chapter 1. Chapter 2 introduces the experimental apparatus of the COMET Phase-I experiment. This chapter explains how the COMET Phase-I experiment can directly measure the RMC photon spectrum. The rest of the thesis is structured as follows:

- Chapter 4 — the simulation study of RMC γ in COMET Phase-I with the evaluation of A_{conv}, A_{geom} and A_{MTW}.
- Chapter 5 — the adaptation of the 2nd level trigger to the RMC measurement and the evaluation of A_{online}.
- Chapter 6 — the development of the denoising and track finding procedure.
- Chapter 7 — the fitting of the electron and positron tracks and evaluation of $\epsilon_{\text{analysis}}$.
- Chapter 8 — the breakdown of the acceptances and the analysis procedure efficiency.
- Chapter 9 — the evaluation of the statistical precision to the γ spectrum end point k_{max}, and of the partial branching ratio R_γ.
- Chapter 10 — evaluation of physical background and systematic error.
- Chapter 11 — discussion about the limit of the Hwang-Primakoff model and the necessity of scanning tail events.
- Chapter 12 — the conclusion of this thesis.

Chapter 4

COMET Phase-I simulation

The computer-simulated RMC γ process is used to evaluate the sensitivity and precision of the COMET Phase-I experiment to RMC γ in the following chapter. This chapter describes how the RMC γs were simulated. The simulation of the signal is used to calculate the geometrical acceptance, the photon conversion rate in the inner wall, and so on. The full beam-related background simulation performed by collaborators [52] and used to test the online trigger scheme (see Chapter 5) is also described. A simpler background simulation based on the full background simulation that is used to test the analysis procedure (see Chapter 6) is also described.

4.1 Simulation framework ICEDUST

The simulation is performed within the Integrated COMET Experiment Data User Software Toolkit (ICEDUST) framework developed for COMET experiment. The software is based on the ND280 framework made for the T2K experiment [55].

The simulation was carried out by using two main packages:

- SimG4 — simulation of event based on GEometry And Tracking (GEANT4) [56]; and
- SimDetectorResponse — simulates the responses of the COMET detectors.

4.2 Radiative muon capture signal simulation

Due to the low geometrical acceptance of COMET Phase-I to RMC γ, a huge number of γs must be generated.

4.2.1 RMC γ generation

The simulation that the COMET collaboration performed for the Technical Design Report [18] calculated the muon stopping distribution in the muon stopping target disks. It simulated 9.7×10^{10} Protons On Target (POT) for a total of 4.5×10^{7} muons stopped in the muon stopping target. The muon stopping distribution is shown in Figure 4.1.

The muon stopping time at the muon stopping target was also estimated using the same simulation. The muon stopping distribution is shown in Figure 4.2, where

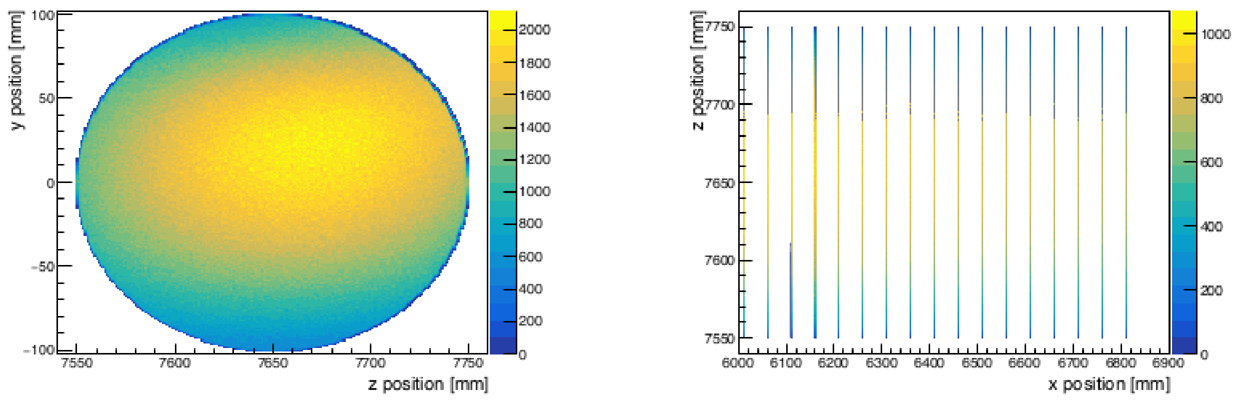

(a) XY plane

(b) XZ plane

Figure 4.1: COMET Phase-I simulated muon stop position in the muon-stopping target system [18]

$t = 0$ ns corresponds to the time, when the protons are generated a few cm upstream of the front surface of the production target. The muon and other beam particles take, on average, around 180 ns to reach the muon stopping target.

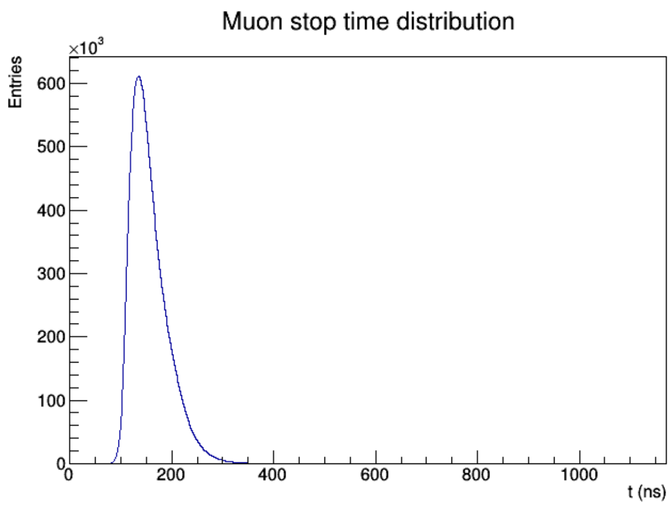

Figure 4.2: Muon stopping time distributio in the muon stopping target

The start position and time of simulated photons are resampled from the distribution shown in Figure 4.1 and from Figure 4.2, assuming no correlation in these distributions. The energy of the γ has been generated uniformly between 60 and 101.85 MeV, which is the maximum allowed energy for the ^{27}Al RMC γ signal. The uniform distribution was chosen to assess the acceptance of the COMET Phase-I experiment dependence on various E_γ at the same statistical level. The photons are generated isotropically.

The simulation is made using GEANT4 electro-magnetic default process. In this model, the pair production process has been simplified, as there is no recoil energy taken by the nucleus. The resultant electron and positron share the total energy of the photon. In a more complex model such as the Penelope Gamma Conversion model [57], on average, in aluminum, for a 100 MeV photon, 5.1×10^{-5} MeV are given to the recoiled nucleus. This is negligible compared to the fitting resolution of the COMET Phase-I experiment to RMC shown in Ch. 7.

4.2.2 Photon to electron positron pair creation

The total number of photons generated in this study is 1×10^{11}. Out of them, 8.1×10^7 photons are converted into the positron and electron pair in the inner wall of the dectetor. The conversion ratios between the different layers of the inner wall are:

- 76.7% in the carbon fiber inner wall, and
- 23.3% in the aluminum inner wall.

The conversion cross section of a photon in a material with an atomic number Z is proportional to Z^2. In the case, of aluminum ($Z = 13$) and carbon ($Z = 6$), at a similar thickness, one can expect four times more conversion in aluminum compared to that in carbon. However, the carbon fiber is made of 30% oxygen ($Z = 8$), which brings the difference in the expected photon conversion rate to a factor 3, consistent with the simulation result shown above.

Figure 4.3 shows the energy distribution of the initial photon that created the electron-positron pair and the corresponding photon conversion acceptance, which is the number of photons converted in the inner wall divided by the number of simulated photons. It shows a slight energy dependence of the pair-creation probability. This behavior is coherent with the observation reported in [58].

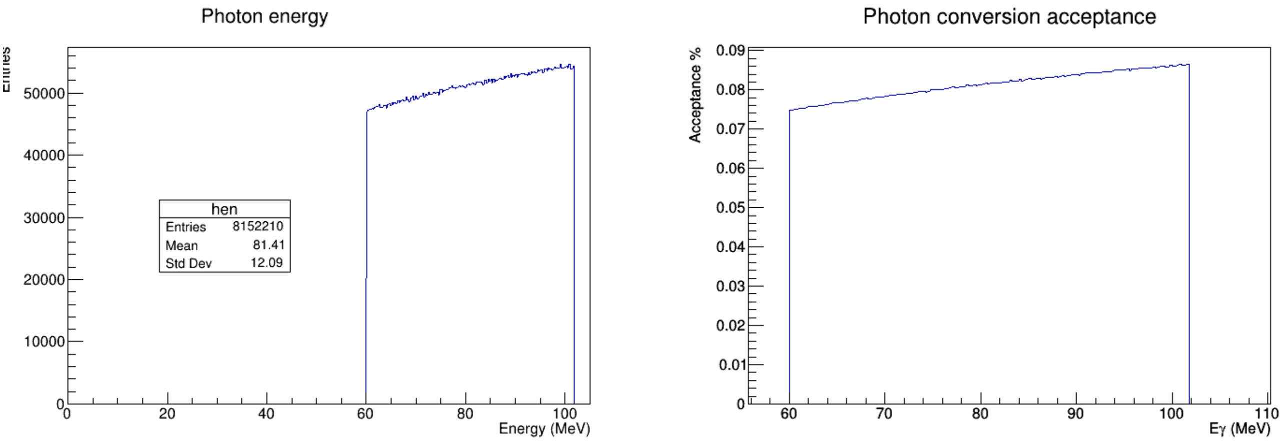

(a) (b)

Figure 4.3: (a) Energy distribution of the photon conversion in inner wall (b) Inner wall photon conversion acceptance

Figure 4.4 shows the momentum distributions of the electron (a) and the positron (b) at the conversion vertices for a photon with an energy of 100 MeV. At first approximation, the share of energy is symmetric between the electron and the positron, but theoretically speaking, the positron energy should be slightly higher due to the recoil of the nucleus, but this effect is too small to be seen in Figure 4.4. The spectrum shows a double bump structure, which is a characteristic of high-energy photon pair production shown in [58].

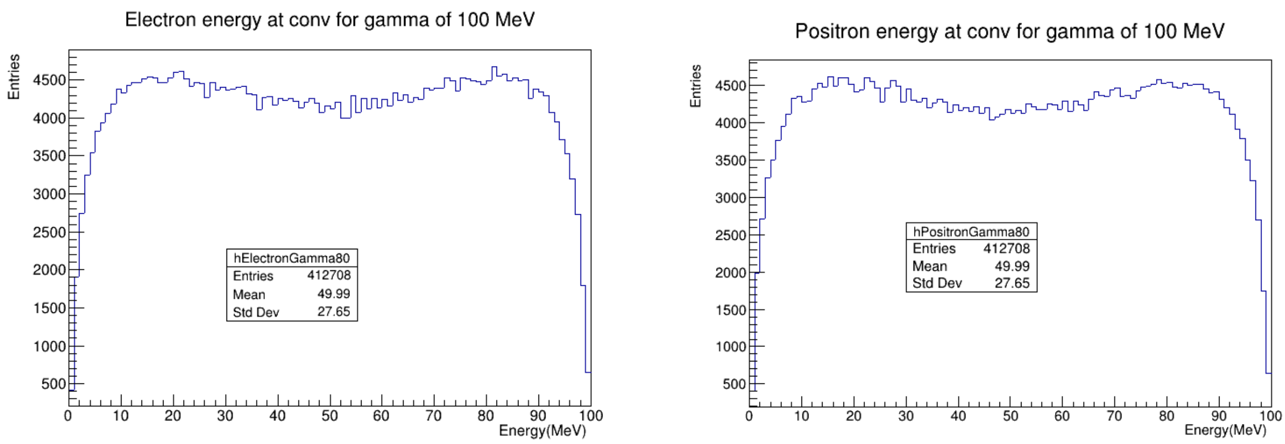

(a) (b)

Figure 4.4: (a) Electron momentum at production for photon of 100 MeV (b) Positron momentum at production for photon of 100 MeV

Figure 4.5 shows the momentum distribution of the electron and the positron produced by photons whose energy ranges from 60 to 100 MeV. The long tail in the higher energy region is caused by two conditions: the photons must have a high energy, and either the electron or the positron must retain the majority of this energy, making it extremely rare for an electron or a positron to reach a momentum of 100 MeV.

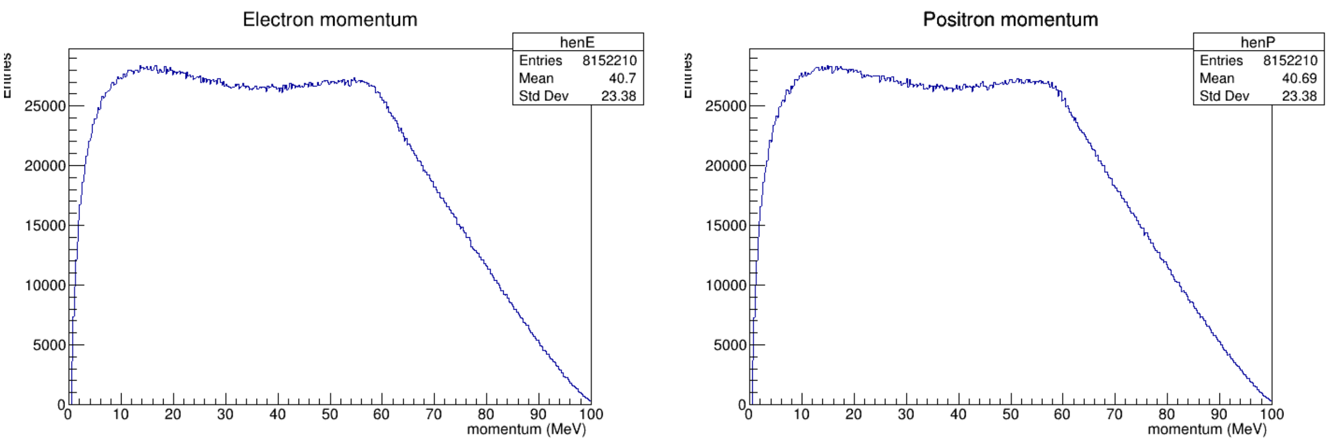

(a) (b)

Figure 4.5: (a) Electron momentum at production. (b) Positron momentum at production

4.2.3 Geometrical acceptance

There are two event-selection requirement that affect the geometrical acceptance:

- either the electron or the positron should pass the CTH trigger requirement (see section 2.2.3), and

- both the electron and the positron should at least reach the fifth layer of the CDC (see section 6.2.2).

Figure 4.6 shows the photon energy distribution (a) for events passing the requirements above, and the corresponding acceptance, which is the number of events passing the above requirements divided by the number of events where the photon converts into the inner wall of the CDC. Compared to a high-energy photon (101 MeV), the probability of a low-energy photon (60 MeV) converting in the inner wall while also satisfying the geometrical cut is reduced by a factor of ten. This is because, to pass the geometrical cut, the electron and positron produced need a certain amount of energy. For low-energy photons, only in the case of symmetrical sharing of the photon energy do both the electron and positron pass the geometrical conditions. While for higher-energy photons, the energy share can be more anti-symetric as the energy that can be used is larger.

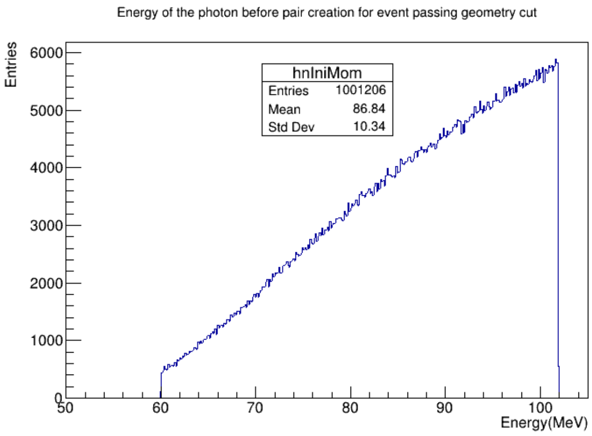

(a)

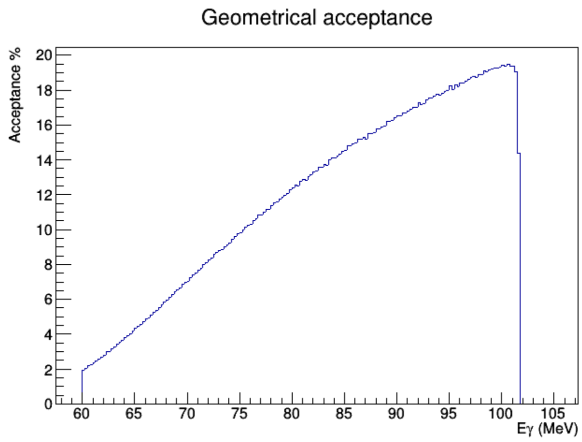

(b)

Figure 4.6: Energy distribution of the photon that created the positron-electron positron pair that pass the geometrical cut (a) and the geometrical acceptance (b)

Figure 4.7 shows the distribution of the electron momentum vs. the positron momentum for the events passing the geometrical cuts. The majority of the events occur in the region where P_{e^-} and P_{e^+} are similar. A minimal amount of energy is needed to reach the fifth layer, which explains why electrons and positrons with momentum inferior to 20 MeV are extremely rare. For the same reason, there is no positron or electron with momentum higher than 80 MeV, because allowing electrons and positrons at higher energy will also allow electrons and positrons with momentum lower than 20 MeV.

4.2.4 Measurement time window acceptance

In the COMET Phase-I experiment, the measurement time window is defined from 700 to 1170 ns, where $t = 0$ corresponds to the arrival time of the proton on the proton target. If an event is triggered outside this range, it will not be seen by the COMET Phase-I experiment. Figure 4.8 shows the trigger timing, and the measurement time window. Some RMC events can happen in the next bunch time window. To take those events into account, a modulo of 1200 ns is applied. 30.1%

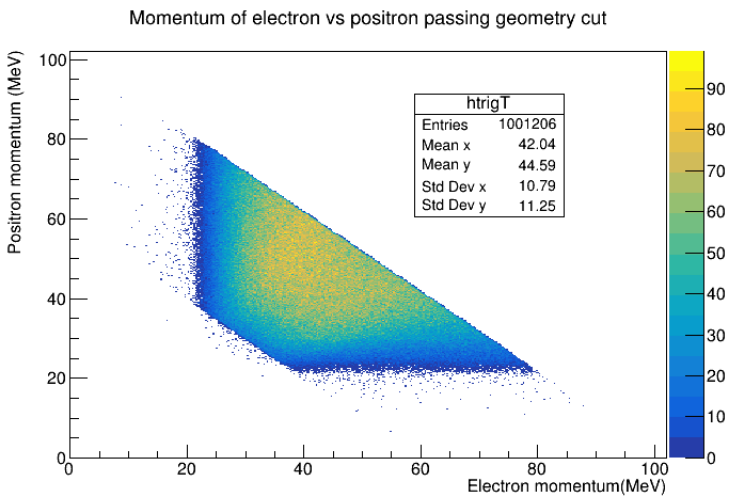

Figure 4.7: Momentum distribution of electron vs positron satistying the geometrical condition of both reaching the 5th layer and having a CTH 4-fold coincidence

of the events are triggered within the measurement time window. The measurement time window can be optimized for the RMC study; for example, a simple increase of the measurement time window from [700-1170] ns to [700-1300] ns can increase the acceptance rate up to 35%. The only limit on the change in the measurement window is the DAQ system. For large measurement windows, the trigger rate of the 1st level trigger increases; however, the DAQ system has a speed limit (26 kHz). To ensure that the DAQ will work in the COMET Phase-I experiment, an online trigger scheme has been designed. Thus, to extend the measurement window, the online trigger needs to be optimized for this specific measurement time window to ensure that the DAQ system will work. The measurement window has not been optimized in this thesis, and the acceptance of 30% will be assumed.

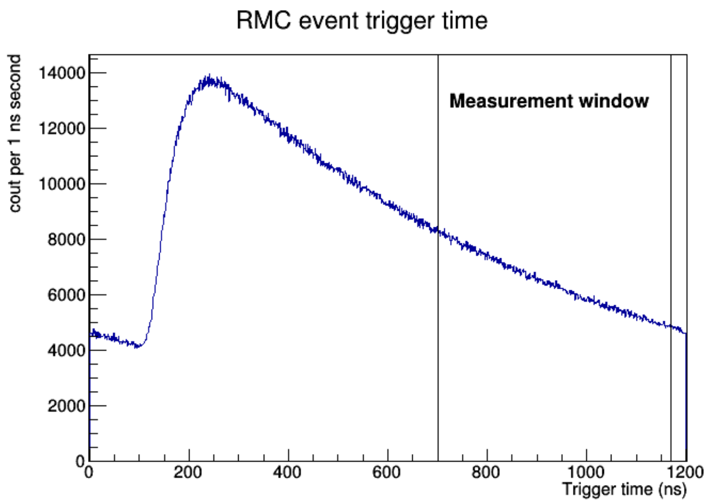

Figure 4.8: Trigger timing distribution. The COMET Phase-I experiment measurement time window is from 700 to 1170 ns. The measure time window contains 30.1%of the total triggered RMC events

The RMC event trigger time is determined by the decay time of the muonic atom (864 ns for muonic Al) and the arrival time of the muon. There is no dependence on the RMC event itself. Thus, to increase the statistics, all the events will be used to test the procedure.

4.2.5 Single turn and multiple turn events

In this study, multiple-turns are defined for particles that leave and re-enter the detector. Figure 4.9, shows a sketch of a charged electron making two turns in the CDC. These multiple-turn tracks cause issues for the track-finding algorithm because they create two or more tracks extremely close to each other in the XY prohection and difficult to separate using the Hough transform. The trajectory fitting algorithm is typically incapable of fitting multiple turn trajectories if the hits from the different turns have not been separated; see section 7.3.2.

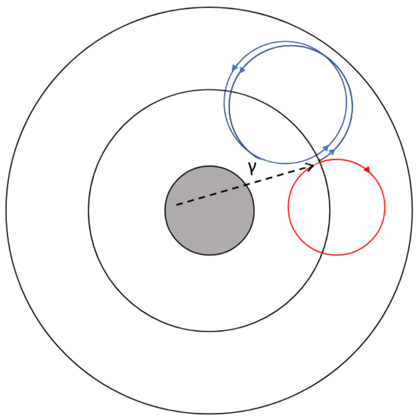

(a)

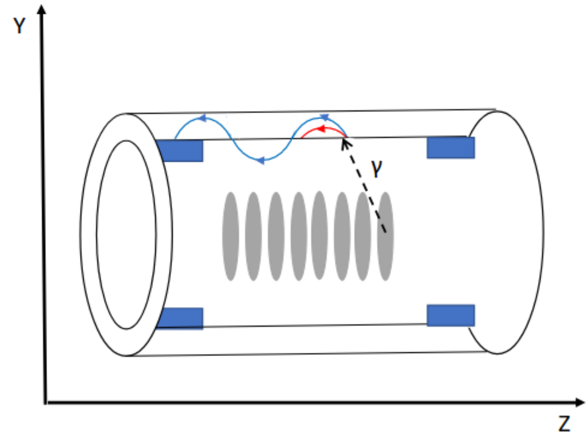

(b)

Figure 4.9: Sketch showing a case when the RMC induced electron makes two turns in the CDC before reaching the CTH in the XY plane (a) and in the YZ plane (b).

The total number of single-turn events (both electron and positron single-turn) is 22.6%. Figure 4.10 shows the distribution of the number of turns for the positron and the electron signal. The high proportion of multiple-turn events compared with single-turn events can be explained by the limitated energy of the electron and positron combined with the geometrical cuts. Both the electron and the positron need to be able to reach the fifth layer. However, to do so, a minimum amount of transverse momentum is needed. Thus, most of the momentum of a particle is in its transverse momentum, while the longitudinal momentum is really low. Due to this low longitudinal momentum, the particle enters and exits the detector, making multiple turns in the detector until it is stopped in the detector, in the inner wall of the detector, or reaches the CTH.

Both single and multiple-turn events are included in the analysis; however, the analysis algorithm is optimized only for single-turn events.

4.3 Background simulation

Two different kinds of background simulations were performed to evaluate the total performance of the COMET Phase-I RMC measurement. One is a full background

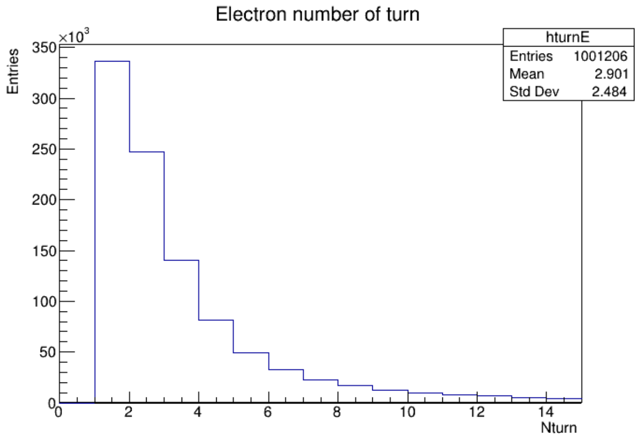

(a)

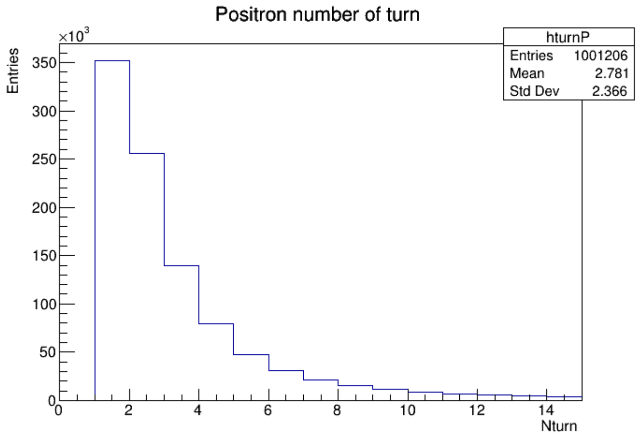

(b)

Figure 4.10: Number of turn in the chamber (a) for electron (b) for positron

simulation of the experiment for a second-level trigger (online trigger) performance check, and the other is a simple random background hit generation based on the full simulation for checking CDC tracking performance.

4.3.1 Full beam simulation

The full beam simulation serves two purposes. First, it is used to make data to test the RMC online trigger presented in Chapter 5. Second, the hit time and energy distribution of the simulated hit are used to generate random hits. The full background simulation was performed in ICEDUST[52]. The simulation was divided into three steps:

- simulation of the muon beam that starts from the proton hitting the proton target and ends at the exit of the muon transport solenoid with beam particles;
- simulation of the detector region starting from the beam particles at the exit of the muon transport solenoid; and
- bunch-train merging to take account of the late arriving beam particles.

Muon beam simulation

A total of 4.8×10^9 proton-on-target (POT) were simulated. They were separated into 300 groups of 1.6×10^7 POT to make bunches. The average number of POT per bunch that is expected in the real COMET Phase-I experiment is 1.6×10^7 POT. This bunch size has been determined for the COMET Phase-I experiment to achieve its goal sensitivity to $\mu^- \to e^-$ conversion.

The simulation is stopped at the end of the muon transport solenoid, where the position, the momentum, and the time of the particles that reached the end of the muon transport solenoid are saved. The simulation of the muon beam takes a lot of resources, and thus, the number of simulated events is limited. To counterbalance this effect, one can use reseeding techniques. Thus, the simulation of the beam is stopped here, and reseeding is used to generate more events with less computing resources. Reseeding is also particularly interesting to test the different effects of changing the detector geometry without having to re-simulate the entire beam.

Detector region simulation

The simulation is resumed using the muon beam simulation recorded information. The statistics are increased by using the reseeding method introduced in the previous section. All the processes happening in the simulation are pseudo-random processes that can change depending on the state of the random generator, which is called the "RNG seed". To make those event change, the simulation is done again with a different RNG seed. The 300 bunches have been resampled 14 times using this technique to produce 4200 bunches.

Bunch train merging

A hit in the detector can be extremely delayed and appear in the next bunch, or in the next next bunch and so on. Thus, to understand the effect of delayed hits on the measurement, it is important to link the bunch together by making a train. The bunch train has been made in the form of a ring, as shown in Figure 4.11.

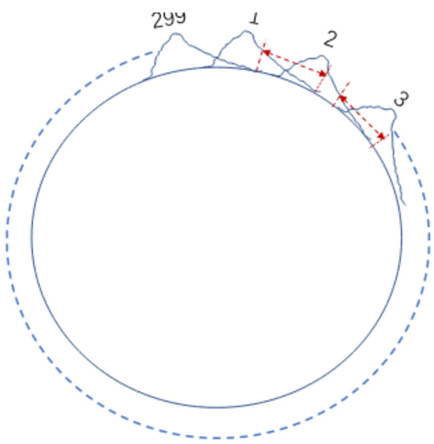

Figure 4.11: Bunch ring train concept [52]

The bunch tail can be particularly long, but the current simulation only considers 300 bunches per train; thus, the ring shape is particularly important to balance the small number of bunches. The number of hits in the CDC as a function of time is shown in Figure 4.12. Time $t = 0$ corresponds to the time of the proton beam hitting the proton target. The different hit contributions in the current frame for the current bunch and for the previous bunches are also shown. This shows that while individual bunch contributions to the hit rate in the detector quickly decline to be negligeable (ΔBunch ID $= -5$), the combined contribution of the previous bunches is far from negligeable (ΔBunch ID $\leqslant -6$).

Figure 4.13 shows the accumulated ratio of hits in the CDC as a function of the number of bunches. This demonstrates that 2500 bunches are required to achieve the true background occupancy of the CDC.

The sample is used to make probability distributions of energy and time of hits for the random hit simulation explained in the following section, as well as to test the online trigger performance in Chapter 5.

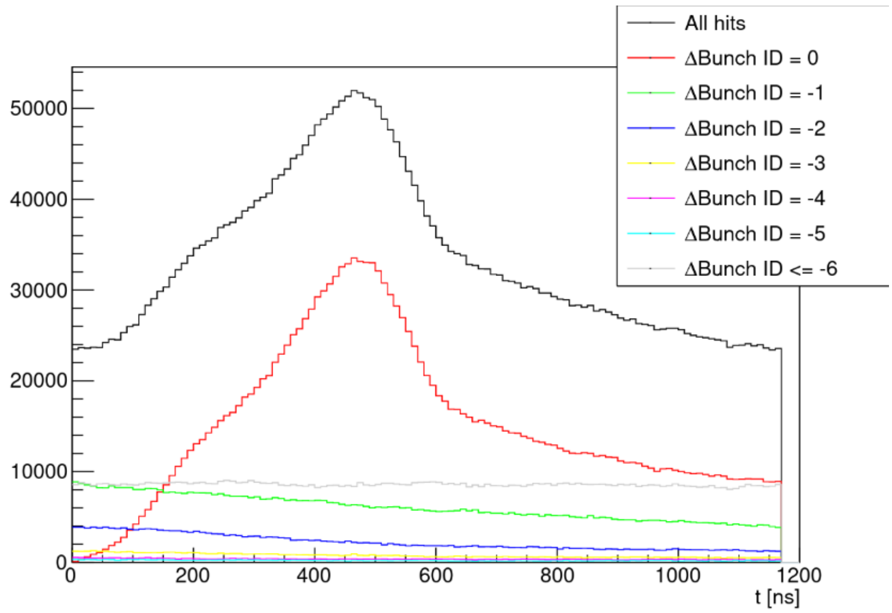

Figure 4.12: Number of hit in the detector function of the time. The total number of hit in the current frame is shown in black. The hit due to the different bunch are shown in different colors [52]

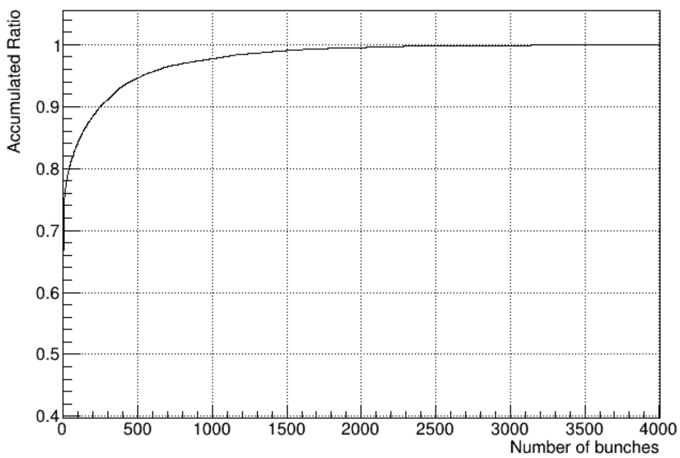

Figure 4.13: The accumulated ratio of hits in the event as a function of the number of bunches [52]

4.3.2 Random hit simulation

The number of simulated bunches is insufficient to be used for testing the analysis procedure. Thus, to test the analysis procedure, a random background was generated.

As shown in Figure 4.12, the number of background hits in the detector changes as a function of time. However, for the analysis, all the triggered events have been kept, even those triggered outside of the measurement time window as explained in section 4.2.4. For example, an event triggered at 500 ns will almost have twice as many hits in the detector as an event triggered in the measurement time window. However, the experiment will only see events that are triggered in the measurement time window, and those highly noisy events will not be seen. Thus, to use these events in this study, their noise level should be coherent with the events triggered in the measurement time window. The distribution of background hits cannot be kept as it is. The background hit times distribution for trigger in the measurement window needs to be calculated. For that, the time is redefined as : $t_m = t_{\text{Hit}} - t_{\text{trigger}}$, where t_{Hit} is the time the hit generates a signal in the CDC relative to the time of the proton bunch arriving at the proton stopping target, and t_{trigger} is the time of the CTH 4-fold trigger. The new background hits time distribution is shown in Figure 4.14. The peak around 700 ns is due to hits from the next beam bunch. It is wider than previously because the trigger can happen anywhere between 700 and 1170 ns, this as the same effect as convoluting it by the trigger rate function in the measurement window shown in Figure 4.8.

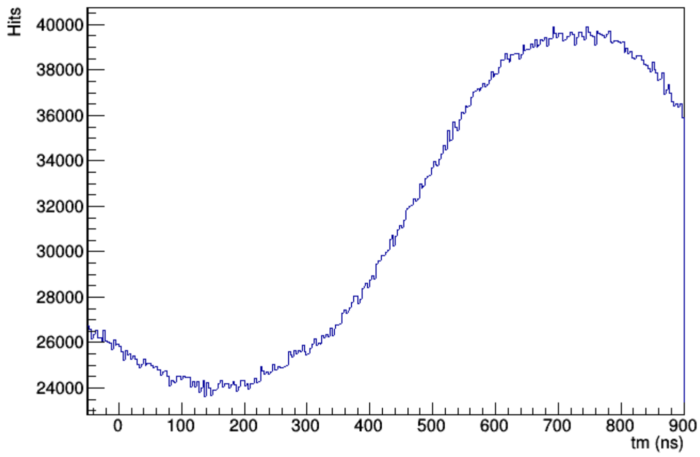

Figure 4.14: Background hits time t_m distribution [52]

In the simulation, there is an average of 5.5 hits per cell in a time window of 900 ns. This multiplicity is mainly due to delta ray showers, that leave multiple hits in one cell [52]. As a starting point, the simulation has been simplified to only generate a maximum of one hit per cell [1]. Thus, using the distribution shown in Figure 4.14 and an average multiplicity of 5.5, one can generate the time distribution of the background hit by only taking the first hit in each cell. The resulting distribution is shown in Figure 4.15.

The energy deposit induced detector response, the ADC-sum, has been generated by using the same technique as the study for $\mu^- \rightarrow e^-$ conversion [59]. The background ADC-sum distribution that was used to generate the random background is shown in Figure 4.16.

The occupancy of the random background has been chosen to be 45%, which is slightly larger than the occupancy expected by the full simulation (42.4± 2.3)%. The occupancy has been slightly increased; which provides another challenge as the random simulated background is not capable of reproducing the features of the simulated background. However, the random background has an advantage over the simulated, which is that the background occupancy can easily be changed to test the limit of the analysis procedure.

[1]Selecting only the first hit in each cell is one possible measurement scheme that can also be used in the experiment.

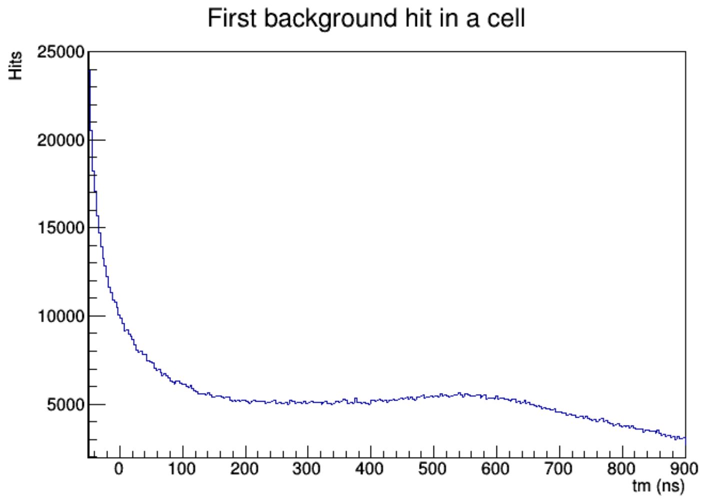

Figure 4.15: First background hit in a cell time t_m distribution [52]

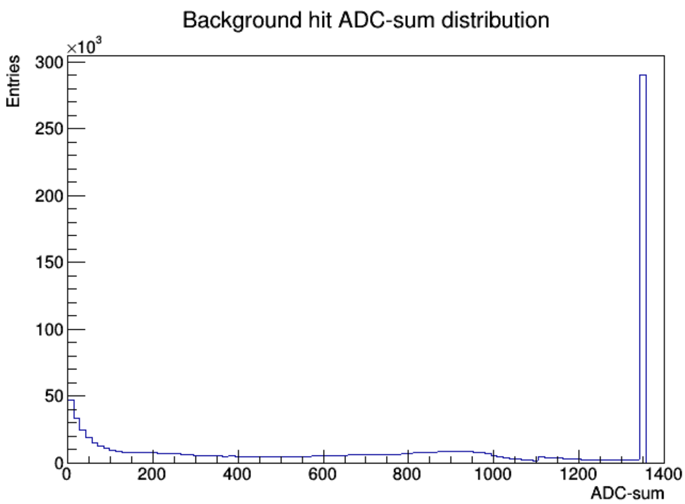

Figure 4.16: The energy deposit induced detector response, the ADC-sum, distribution for simulated background [52]

4.4 Event time window

As defined in the previous section, the measured time is:

$$t_m(i) = t_{\text{Hit}}(i) - t_{\text{trigger}}, \tag{4.1}$$

where $t_m(i)$ is the measured time of hit i by the experiment, $t_{\text{Hit}}(i)$ is the time of the hit previously defined, and t_{trigger} is the time of the CTH 4-fold trigger. The measured times for the RMC signal and background hits are shown in Figure 4.17. Hit can have a measured time inferior to zero because the hit occurs before the trigger time by a delay superior to the $t_{\text{Hit}}(i)$.

In the following chapters, the time of each hit will correspond to t_m. Only hits with t_m between -50 ns and 400 ns are taken into account. This cut helps remove 42% of the background hits while only sacrificing 8% of the RMC signal hits. The sacrificed RMC signal hits are due to so-called ”corner hits”, which are hits made in the corner of a cell where the electric field is weak. Because the electric field felt by the ionized electron is weak, it takes time for it to reach the sense wire.

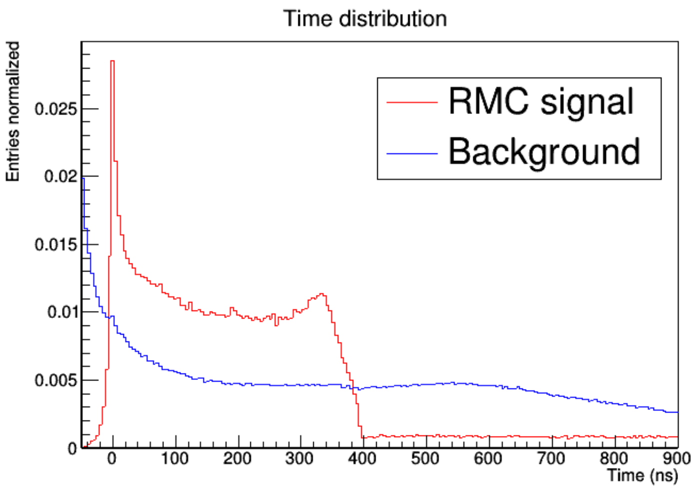

Figure 4.17: Time distribution of RMC signal and background hits

Chapter 5

Online trigger scheme

This chapter describes the implementation of an online trigger for RMC based on the trigger study for $\mu^- \rightarrow e^-$ conversion already performed [59].

The purpose of this chapter is first to ensure that the RMC online trigger framework can be implemented in the current trigger framework. The second goal of this chapter is to calculate the online trigger acceptance, which is used to predict the number of expected RMC events in the COMET Phase-I experiment.

5.1 Concept

The first-level trigger described in section 2.2.3 has a trigger frequency of 100 kHz [59], which is unacceptable for the Data Acquisition (DAQ) system, which can only support a rate inferior to 26 kHz. To reduce the rate from 100 kHz to 26 kHz, the online trigger is built in two steps:

- Hit classification: separate background hits from signal hits in one event frame. To do that, one can use a look-up table (LUT), which gives a score for each hit.

- Event classification: decide if one event should be saved or not. To do that, one can count the number of hits with a hit classification score greater than a certain threshold. If the number of hits is greater than a certain threshold, the data of the event is saved. If not, it is not saved.

The same framework can be used to construct an RMC online trigger with slightly different parameter optimizations. The current parameters have been optimized solely for $\mu^- \rightarrow e^-$ conversion; however, there are a few variations between the RMC electron-positron pair signal and the $\mu^- \rightarrow e^-$ conversion electron signal features. For example, the final decision of the online trigger (event classification) relies on the number of hits left in the chamber; however, for RMC events, an average of 34 hits are left by the positron-electron pair signal, while for $\mu^- \rightarrow e^-$ conversion electron signal, the average number of hits is 50.

In the following sections, the optimization of the online trigger for RMC is described. At the end of the chapter, its performance is evaluated. The optimization and the test of the RMC online trigger are evaluated with the fully simulated background described in section 4.3.1.

5.2 Hit classification

In real-world data collection, the purpose of hit classification is to determine whether a hit is a signal hit or a background hit. The hit classification is performed using a LUT stored in the trigger hardware.

5.2.1 LUT input parameters

The LUT uses four parameters as inputs to distinguish background hits from signal hits:

- its radial position (layer ID),
- its ADC sum, which is the detector response associated to a hit,
- its left neighbor ADC sum, and
- its right neighbor ADC sum.

Radial position

Figure 5.1 shows the radial position distribution for background and signal hits. Signal hits (electron and positron) are often constrained in the first few layers of the CDC due to their limited momentum range and the effect of the magnetic field. On the other hand, the background follows a flat distribution. This difference is helpful for distinguishing RMC signal hits from background hits.

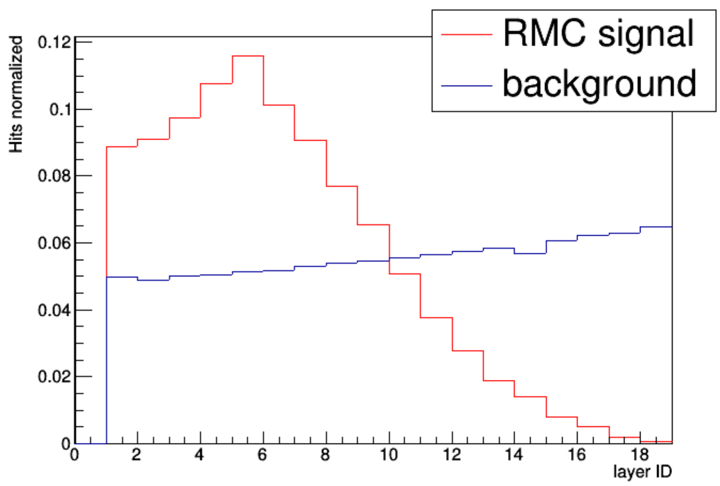

Figure 5.1: Radial position distribution of the RMC signal and background CDC hits. Guard layer hit are not shown.

ADC sum The ADC sum is the detector response associated with a hit in the detector. In the COMET Phase-I experiment, the ADC-sum detector response of a hit is proportional to the energy deposit of that hit. If the energy deposit induced charge is greater than 7 pC, a value of 1350 ADC-sum is returned, which corresponds to the saturation point of the electronic circuit. The ADC-sum distributions for the

RMC signal and background are shown in Figure 5.2. The main difference between the RMC signal energy deposit and the background energy deposit is due to the fact that while the signal is only composed of electrons and positrons, the background is composed of various particles such as protons, pions, muons, and so on. The proton, which has an energy deposit 100 times larger than the electron for the momentum region of interest (100 MeV), is the main source of background hits, which explains the larger ADC-sum for the background hits.

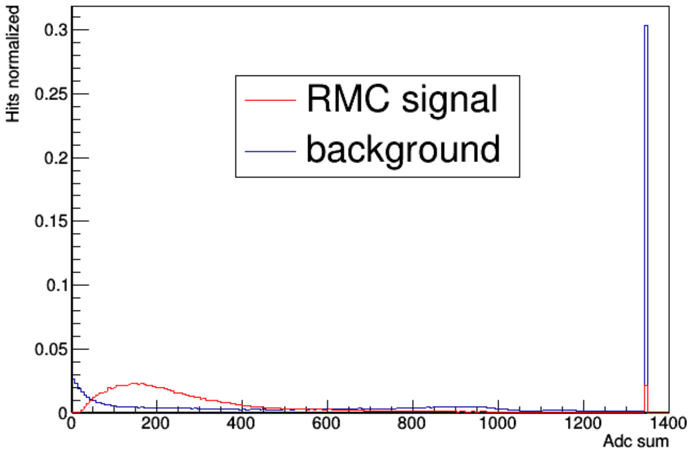

Figure 5.2: ADC sum distributions

ADC sum encoding scheme Due to the limitations of the online trigger hardware, the ADC sum must be encoded down to a smaller data size to reduce the data transfer time. Two different encoding schemes have been tried in [59], 1-bit and 2-bit encoding schemes; the 2-bit encoding scheme has been chosen because it meets the DAQ requirement and provides a better separation between the signal $\mu^- \to e^-$ conversion hits and the background hits than the 1-bit encoding scheme. Thus, the 2-bit encoding scheme has also been chosen for RMC.

Figure 5.3 shows the ADC sum distribution for signal and background hits. It also shows the corresponding 2-bit ADC sum values. The threshold values($q_{th} = 900$ and $q^i_{div} = (6,\ 100,\ 400)$) have not been optimized and have been chosen to be identical to the one used by the $\mu^- \to e^-$ conversion online trigger. By keeping the same encoding scheme as the one used for $\mu^- \to e^-$ conversion trigger, no additional encoding time is needed for the RMC online trigger.

Figure 5.4 shows the resulting distribution of a 2-bit encoded ADC sum conversion. One can see that a large portion of the background hits (a little less than half) are assigned a value of 0. On the other hand, the signal peaks at 2. This difference is helpful for distinguishing RMC signal hits from background hits.

Neighbor wire: left and right

Each sensing wire on each CDC layer is given a wire ID number, W_{id}. This number goes from 0 to the number of sense wires in this layer minus 1. As illustrated in Figure 5.5, the wire ID increases clockwise while looking in the beam direction. Right and left wire neighbors are defined for wires on the same layer. The left and right neighbors of a wire with $W_{id} = w$ are the neighbor with $W_{id} = w - 1$ and the neighbor with $W_{id} = w + 1$, respectively.

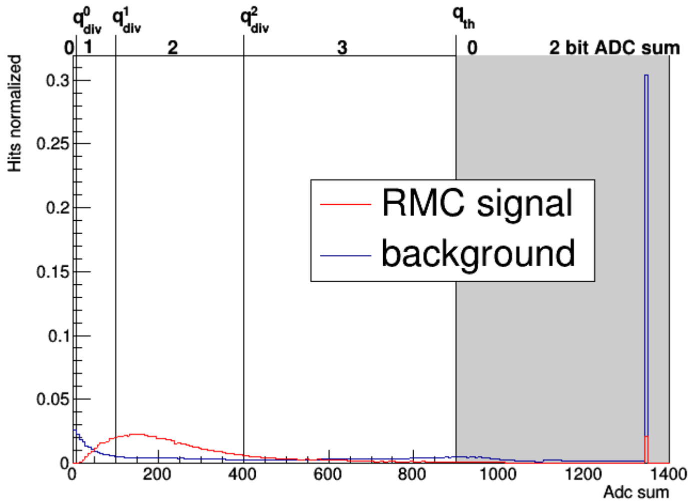

Figure 5.3: ADC sum distribution. $q_{th} = 900$ and $q^i_{div} = (6,\ 100,\ 400)$ are threshold for the ADC conversion into the 2-bit ADC sum.

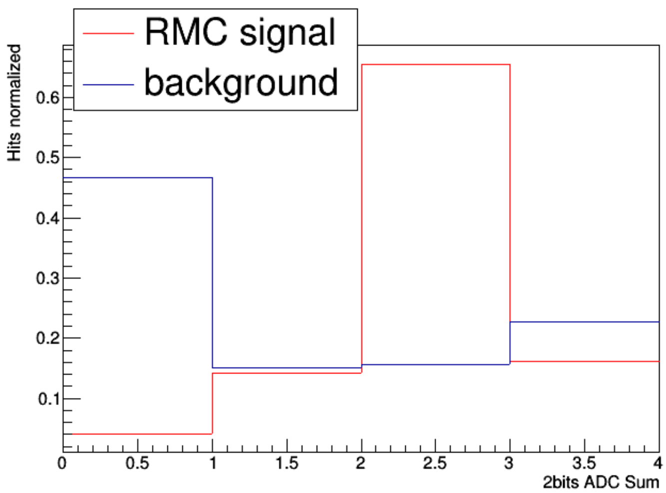

Figure 5.4: 2-bit encoded ADC sum distribution for signal and background hits

ADC sum neighbor Figure 5.6 shows the distribution of the 2-bit encoded ADC sum for the neighbor on the right and on the left. The number of hits with a neighbor ADC sum of 0 increases for both the background hit and the RMC signal hit compared to the ADC sum shown in Figure 5.4 because many hits do not have a neighbor hit. Except for the hits with no neighbor, the neighbor ADC sum distribution shape is similar to the ADC sum distribution observed in Figure 5.4. This is because a particle going into the CDC makes hits close to each other; thus, one hit from this particle has a higher chance of being the neighbor of another hit that it made.

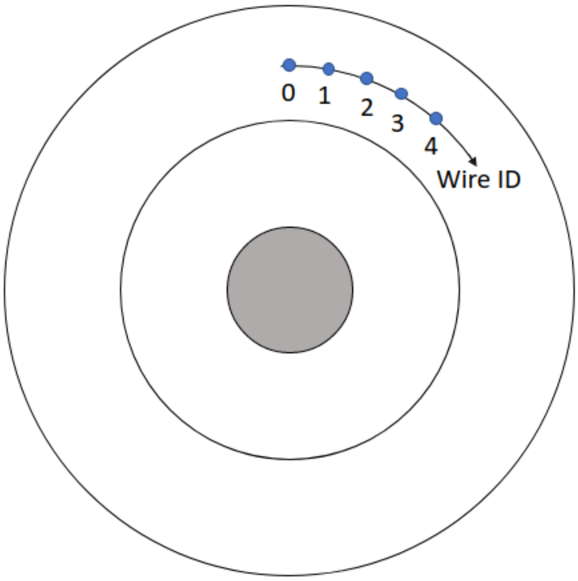

Figure 5.5: Sketch of the wire ID numbering scheme

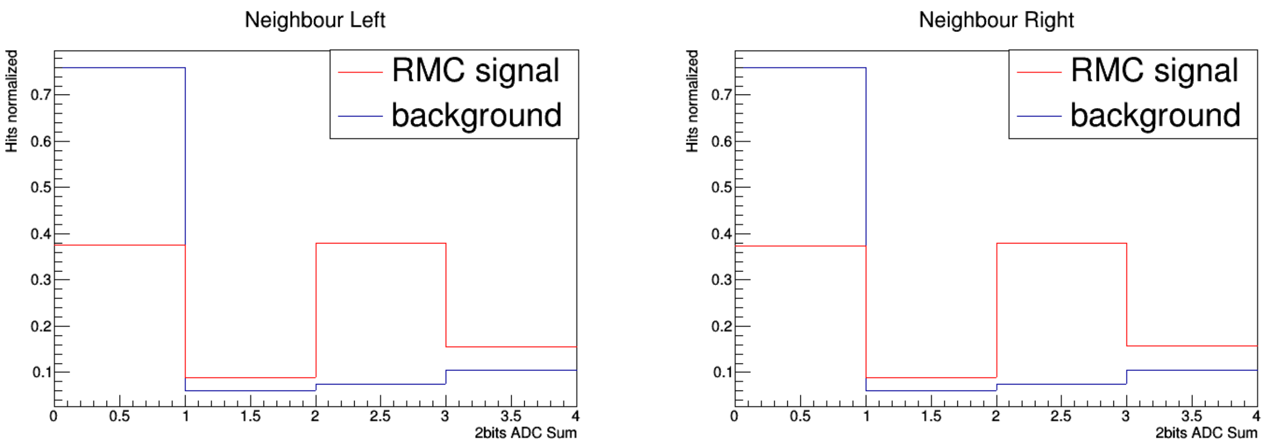

(a) (b)

Figure 5.6: ADC sum distribution encoded in two bits for neighbors, (a) right neighbors and (b) left neighbors

5.2.2 LUT parameter optimization

Since none of the parameters above can provide a clear separation between signal and background alone, it is necessary to combine those parameters somehow. In this study, like in the study for $\mu^- \to e^-$ conversion online trigger, a Gradient Boosted Decision Tree (GBDT) is used to obtain an optimal separation. The GBDT is one of machine learning technique. It must be trained with a training sample to be optimized.

The number of fully simulated background events is 4200 as explained in section 4.3. Out of them, 3300 events are used for the training of the GBDT, while the remaining 900 events are used for testing the performance of the RMC online trigger scheme. The GBDT parameters are the same as those used for the $\mu^- \to e^-$ conversion online trigger study [59]. The details of GBDT are described in the Appendix A. The main parameters are:

- 1000 trees,
- the maximum depth of a tree is 5,
- the binning variable is 20.

The GBDT gives an output value between -1 and 1, called the score. The closer the score is to 1, the more signal-like the hit features are. If its score is close to -1, its features are background-like.

5.2.3 Results with optimized LUT

Below, one can see the input parameters ranked by their separation power [60]:

- Radial position — 0.3324.
- ADC sum — 0.262.
- ADC sum of left neighbor — 0.204.
- ADC sum of right neighbor — 0.2016.

A separation power of 1 indicates a total separation between the background and the signal distribution, whereas a separation power of 0 indicates total overlap between the background and the signal distribution.

Figure 5.7 shows the distribution of the score for signal and background hits. The background hit score distribution is concentrated on -1, while the RMC signal one is concentrated between 0.8 and 1, showing a good separation between the RMC signal and background hits.

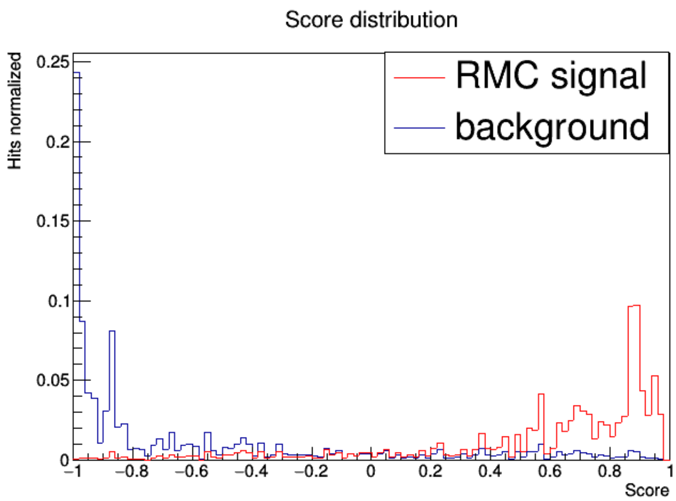

Figure 5.7: Score distribution for RMC signal and background hits

To have a more visual quantity, such as signal hit retention efficiency vs. background hit rejection efficiency, one can draw a line in the score distribution ($score = 0$) from Figure 5.7, and count the number of hits on the left of the line and the number of hits on the right of the line. The hits on the left are the hits rejected by asking for a score of 0, and the hits on the right are the ones that are kept by asking

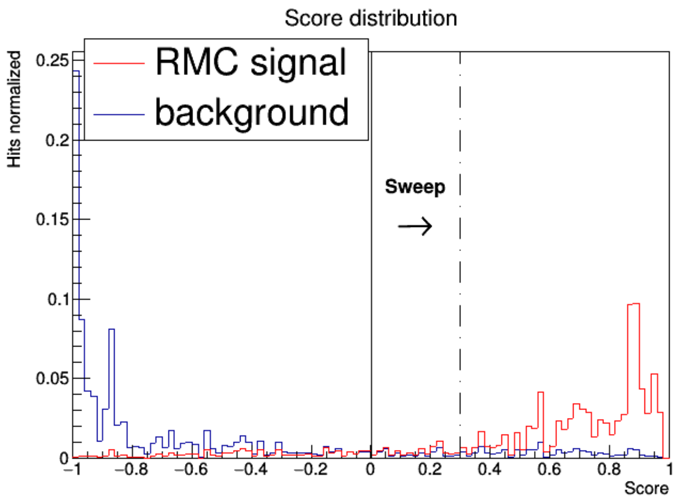

Figure 5.8: score distribution for signal and background hits with a sweeping example

for a score of 0. This can be repeated by moving the line by a small step, as shown in Figure 5.8.

Figure 5.9 shows the resultant Receiver Operator Characteristics (ROC) curve for the hit filtering. The scanning starts from the line at $score = -1$, and proceeds with step size of 1×10^{-5}. The background rejection corresponds to the number of background hits that were rejected divided by the total number of background hits. Hit efficiency corresponds to the number of signal hits that were kept divided by the total number of signal hits. The up-and-down structure in the ROC curve is due to the numerous peaks in the score distribution shown in Figure 5.7.

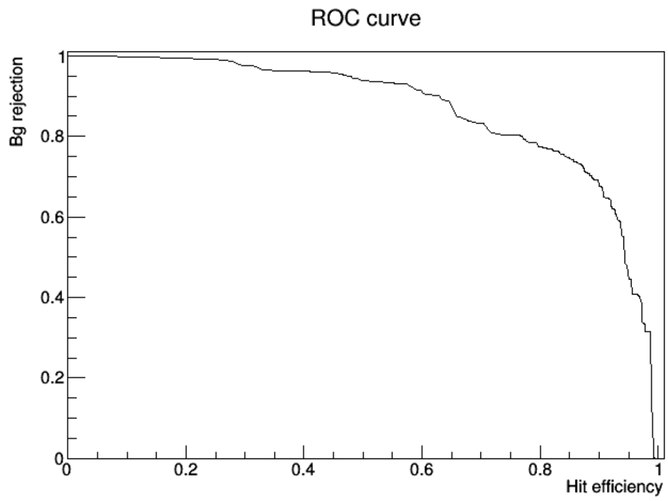

Figure 5.9: Hit filtering ROC curve.

Figure 5.10 shows a typical event projected on the middle of the CDC for different cut on the score with their corresponding efficiency and purity.

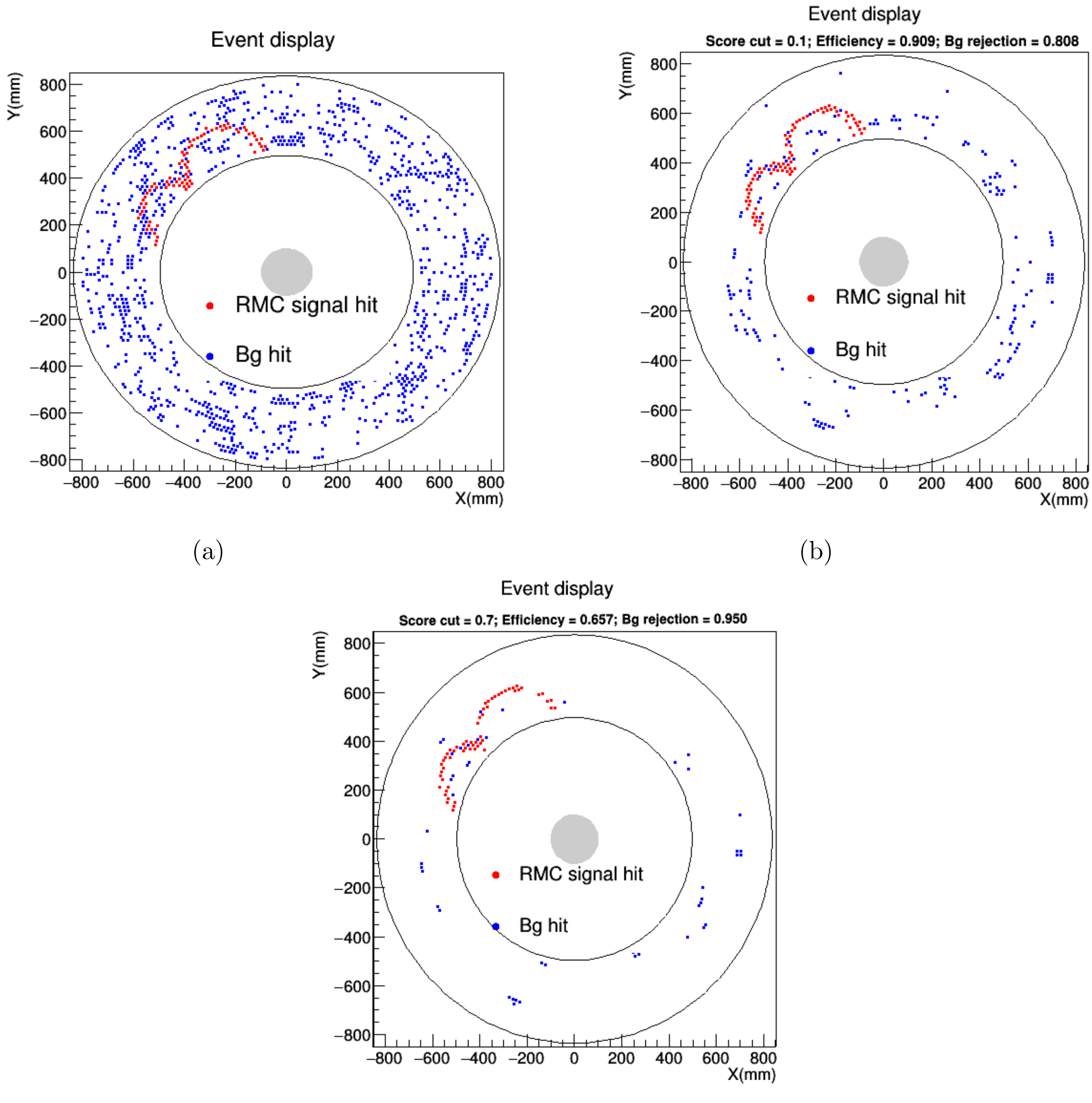

(a) (b) (c)

Figure 5.10: Projection of background and signal hits in the middle of the detector. (a) No selection on hit, (b) Hit with a LUT score superior to 0.1, and (c) Hit with a LUT score superior to 0.7

5.3 Event classification

The event classification makes the final decision about saving or not saving the event. This is accomplished by counting the number of hits with a LUT score greater than a predefined threshold ($N_{\text{hit threshold}}$). If the number of hits exceeds the $N_{\text{hit threshold}}$, the event is saved. Figure 5.11 shows the distribution of hits per event having a score exceeding 0.5. An example of a possible $N_{\text{hit threshold}}$ cut is also shown. One can count the number of events on the left to obtain the number of rejected events and on the right to obtain the number of triggered events. A scan on the $N_{\text{hit threshold}}$ can be performed for various LUT score thresholds to generate event classification

ROC curves.

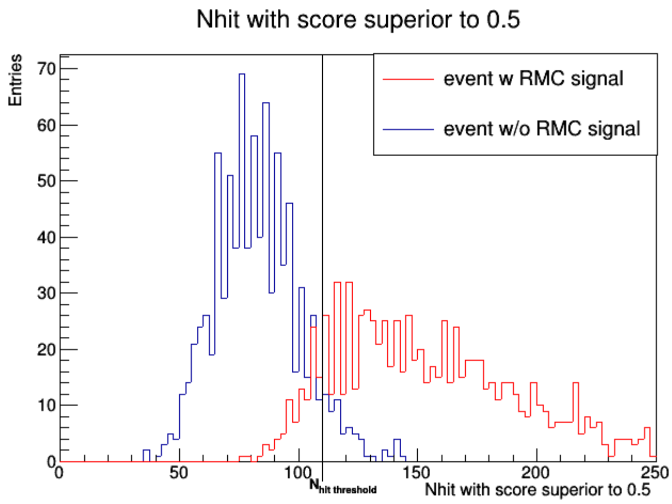

Figure 5.11: Number of hit with a GBDT score superior to 0.5 for event with RMC signal and without RMC signal.$N_{\text{hit threshold}} = 110$

Figure 5.12 shows the resultant event classification ROC curves. The online trigger can achieve a rejection rate of 96% for a signal event acceptance rate of 90% using a LUT score of 0.8 and $N_{\text{hit threshold}} = 35$.

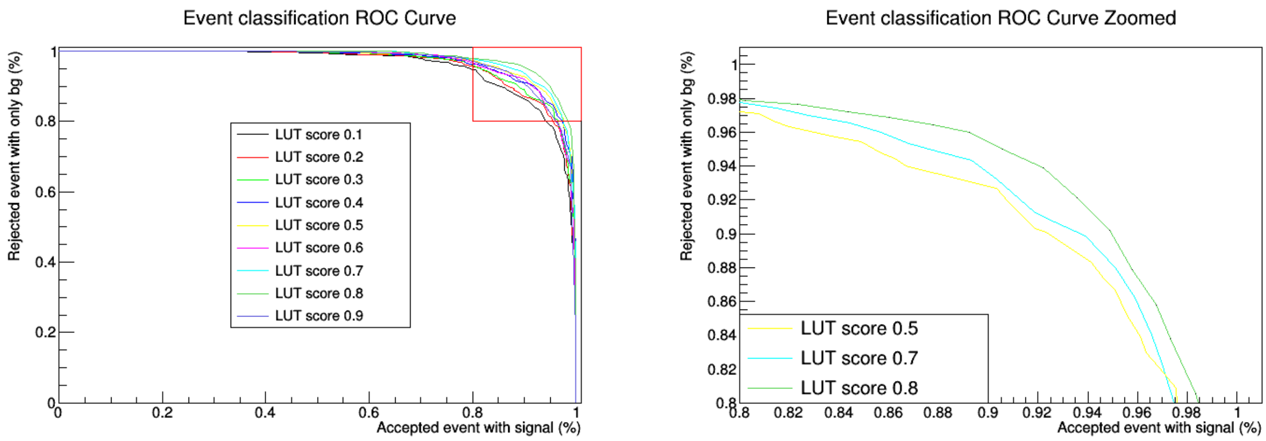

(a) (b)

Figure 5.12: Event classification ROC Curve. (a) Event classification ROC curve for different LUT score (b) Event classification ROC curve only keeping the best 3 ROC curves

5.4 Results

The current first-level trigger of the COMET Phase-I experiment has a rate of 100 kHz; however, the DAQ system can only work at a trigger rate below 26 kHz [59]. The online trigger helps reject 96% of the background trigger events while only losing 10% of the RMC-triggered events. which, for the RMC trigger condition, brings the trigger rate down to 4 kHz, which is more than enough for the DAQ system to work. Therefore, RMC data can be collected simultaneously with the main data taking. In the following chapters, the online trigger acceptance of 90% will be used to estimate the total number of RMC events expected to be seen in the experiment.

Chapter 6

Hit filtering and track finding procedure

The physics analysis performance of RMC is described in this chapter as well as in Chapter 7 and 9.

This chapter describes the hit filtering and track finding procedures. The goal of these procedures is to extract RMC signal hits and identify if they are hits from the electron track or the positron track. To achieve this goal, the procedure is separated into 4 steps:

- hit filtering using a GBDT algorithm,
- a track finding algorithm using Circular Hough Transform (CHT),
- identification of the track candidates, and
- extraction of hit candidates.

In this chapter, the background hits were generated uniformly inside the CDC. The time and energy of the random hits were sampled from a simulated background with ICEDUST, as shown in Sec. 4.3. With this method, the background occupancy can be changed so that the analysis performance under different background occupancy levels can also be studied. The examples and results reported in this chapter and the following chapters consider a background occupancy of 45%.

6.1 Hit filtering

According to the simulation, the background occupancy level is around 41% [52]. At this level, a traditional track finding algorithm without any hit filtering, such as the Hough transform, cannot work. Figure 6.1 shows a typical event with circular Hough transforms found circles without any preliminary hit filtering. Only the 5 best circles according to the circular Hough transform are shown, and none are from the electron track or the positron track. Thus, it is necessary to reduce the number of background hits to make the Hough transform work. A GBDT algorithm, which is the same technique used to optimize the online trigger, is used for that purpose.

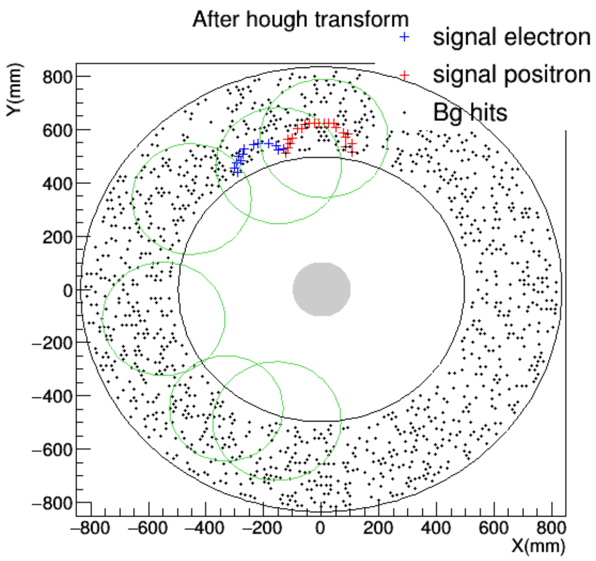

Figure 6.1: Circular Hough transform best 5 circles without applying any pre-filter.

6.1.1 GBDT parameters

The GBDT used in the offline analysis can be much more complicated since there are no constraints from the hardware side. The GBDT uses two types of features: hit features and neighbor hit features. The hit features used are:

- the radial position,
- the ADC sum,
- the hit timing, and
- the delta ϕ — Angle difference between the CTH 4-fold trigger and the wire.

Some of these hit features are similar to these shown in chapter 5. However, they are explained again because, unlike in the previous chapter, the background does not come from the simulation but is instead uniformly generated in the chamber.

Radial position Figure 6.2 shows the layer distribution for the signal and background hits. Due to the magnetic field of 1 T, the signal cannot reach the upper layers. On the other hand, the background is distributed uniformly between the layers. The distribution of background on the layer is similar to the distribution shown in chapter 5 with simulated background. This shows that the random background can reproduce the radial distribution of the simulated background. As seen in chapter 5 radial distributions for background and RMC signal hits is different and can be used to distinguish them.

ADC Sum Figure 6.3 shows the ADC sum distributions for the signal and background hits. The signal ADC sum peaks around 150. On the other hand, the background has a peak around 50 ADC sum, with a visible overflow at 1350. The background ADC sum is coherent with the ADC sum shown in chapter 5, where the background was simulated. This is because the ADC-sum of the random background hit has been generated according to the simulated ADC-sum background hit distribution. As seen in chapter 5, the ADC-sum distributions for background and RMC signal hits is quite different and can be used to distinguish them.

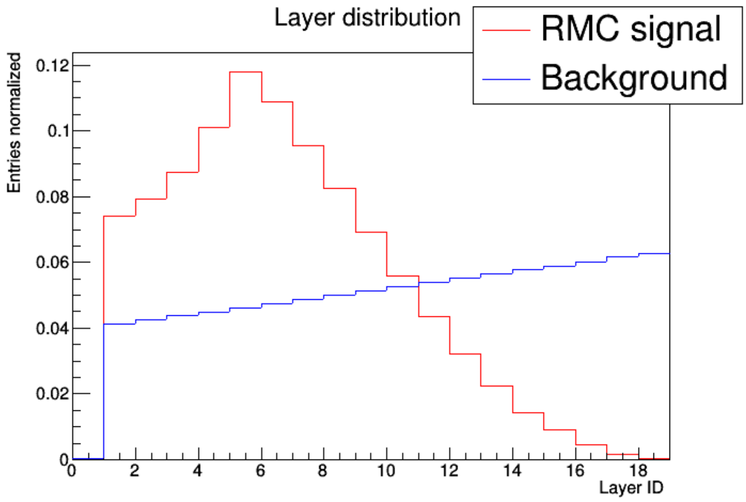

Figure 6.2: Layer distribution

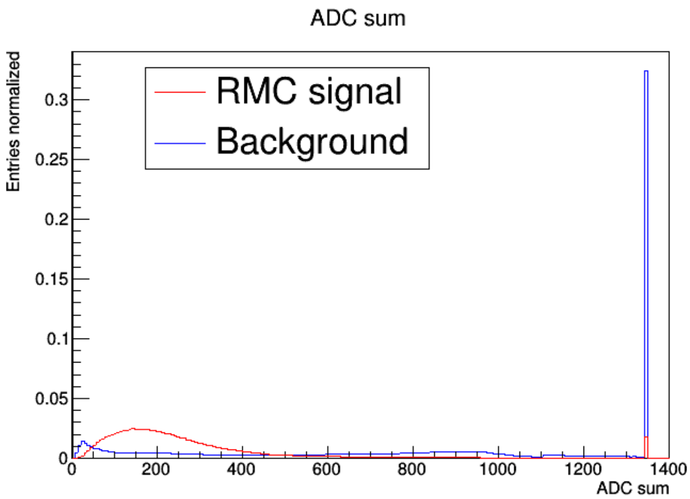

Figure 6.3: ADC sum distribution

Hit timing Figure 6.4 shows the time distribution (t_m)for the signal and background. The RMC positron or electron makes the trigger time; thus, its timing peaks at 0 ns. However, because there is no relationship between the background t_m and the trigger time (t_{trigger}), it simply follows the background hit time distribution, which is determined by the prompt beam timing. The timing distributions are different for RMC signal and background hits, which is helpful for distinguishing them.

Delta ϕ It is the radial angle difference between the wire position (projected at the endplate of the detector) and the CTH 4-fold coincidence module. Figure 6.5 shows a sketch with a typical angle Delta ϕ for an electron hit. The sign of delta ϕ is also shown.

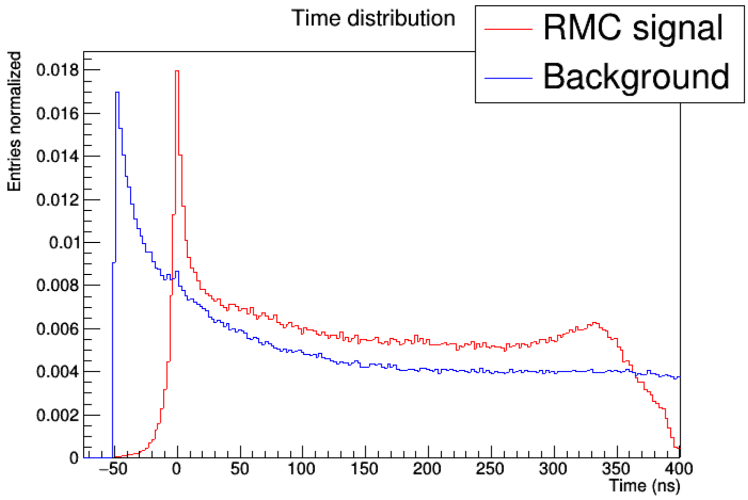

Figure 6.4: Timing distribution

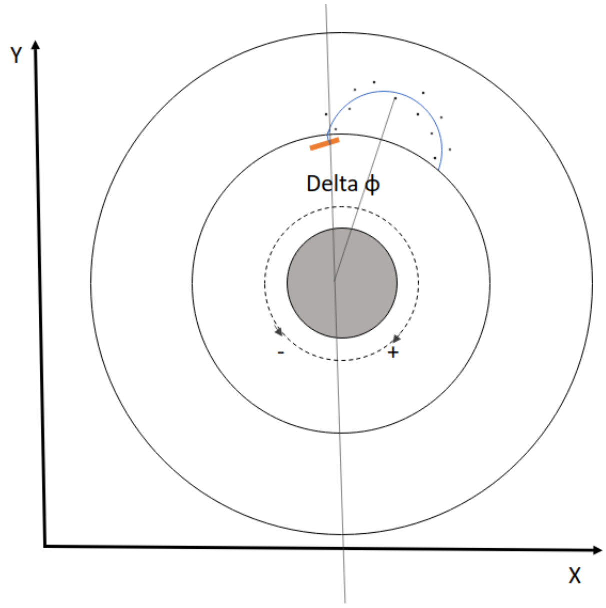

Figure 6.5: Sketch of a detector where an electron hit the CTH module. Delta ϕ of a hit is defined as the angle between the CTH hit and this hit.

Figure 6.6 shows the delta ϕ distributions for the signal and background hits. For the background, the distribution is uniform, while for the signal, it shows a peak around ϕ. The CTH 4-fold trigger is made by the RMC signal, so hits from the signal are constrained to the same radial region as the trigger. The Delta ϕ distribution differs significantly between the RMC and background hits, which aids in distinguishing them.

The neighboring features of a hit are its neighbors:

- left ADC sum,
- right ADC sum,

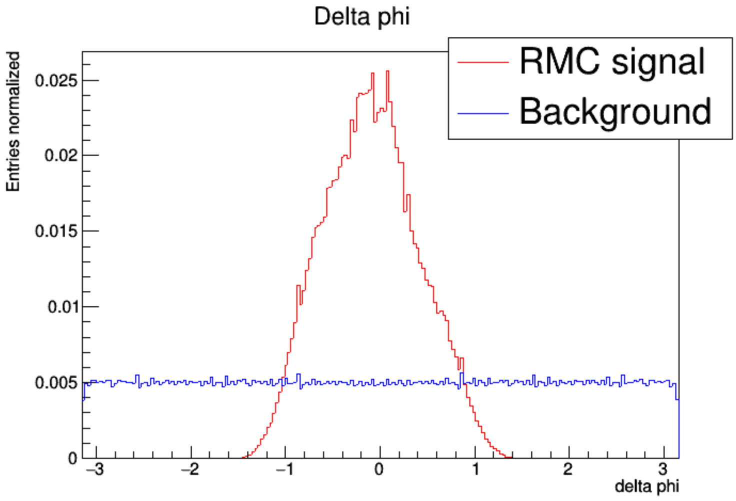

Figure 6.6: Delta ϕ distribution

- down ADC sum,
- down right ADC sum,
- down left ADC sum,
- up ADC sum,
- up right ADC sum, and
- up left ADC Sum.

The definition of "neighbor" is basically the same as explained in section 5.2.1. However, these features have been greatly expanded. The neighbor up of a wire with a layer ID $L_{id} = l$ is the wire that is the closest to it with a layer ID $L_{id} = l + 1$. The distance between each wire is calculated in the XY plane in the middle of the CDC. Similarly, its down wire is the closest wire with a layer ID $L_{id} = l - 1$. Up right and up left are the right and left neighbors of the up wire, respectively. Similarly, down right and down left are the right and left neighbors of the down wire, respectively.

Figure 6.7 shows the ADC sum for the left and right neighbors. If there is no neighbor hit, the neighbor ADC sum is set to -1. The figure does not show the hit when the ADC sum value is -1. The distribution of the ADC sum for left and right neighbors looks a lot like the one shown in Figure 6.3. The main reason is that signal hits are always close to other signal hits. As a result, the likelihood of a signal hit having as a neighbor another signal hit increases. For background hits, the probability of having a signal hit as a neighbor is small because, as shown by the Delta ϕ distribution, it can only happen in a limited space region.

Figure 6.8 shows the ADC sum for up and down neighbors. Figure 6.9 shows the ADC sum for up right, up left, down right, and down left neighbors. The distribution of ADC sum for neighbors is similar to the one shown in Figure 6.3.As explained above, signal hits are close to other signal hits, so signal hits are more likely to have another signal as a neighbor.Thus, the ADC sum neighbor distribution is similar to the RMC signal ADC sum. For a similar reason, a background hit has a higher chance of being closer to other background hits; thus, the ADC sum neighbor distribution for background hits is similar to the ADC sum distribution. All neighbor hit ADC-sum distributions are different for RMC signal and background hits and can be combined to distinguish background hits from signal hits.

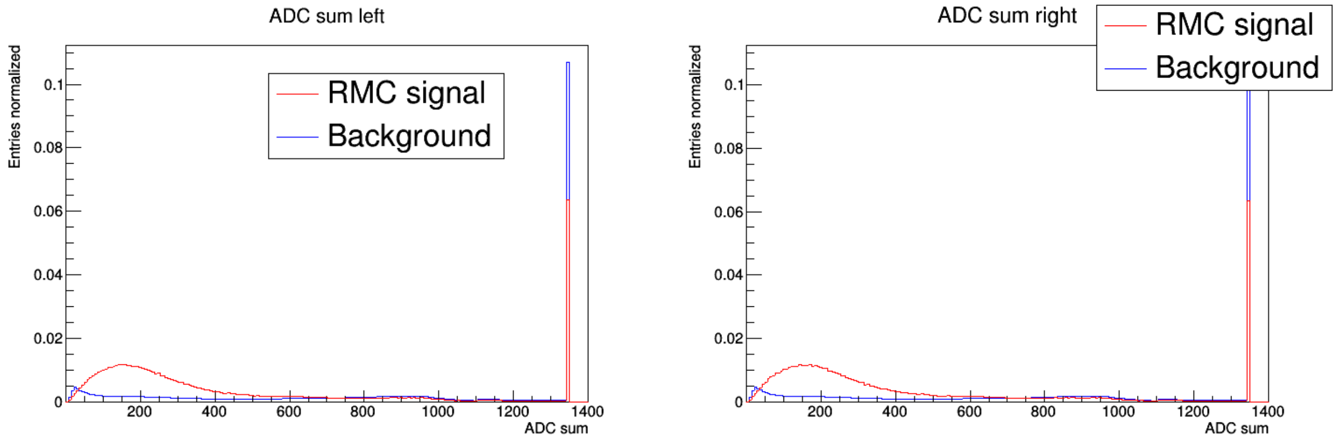

(a) (b)

Figure 6.7: The ADC sum distribution for hits with no neighbors (ADC sum = -1) has not been plotted (a) for the left neighbor (b) for the left neighbor.

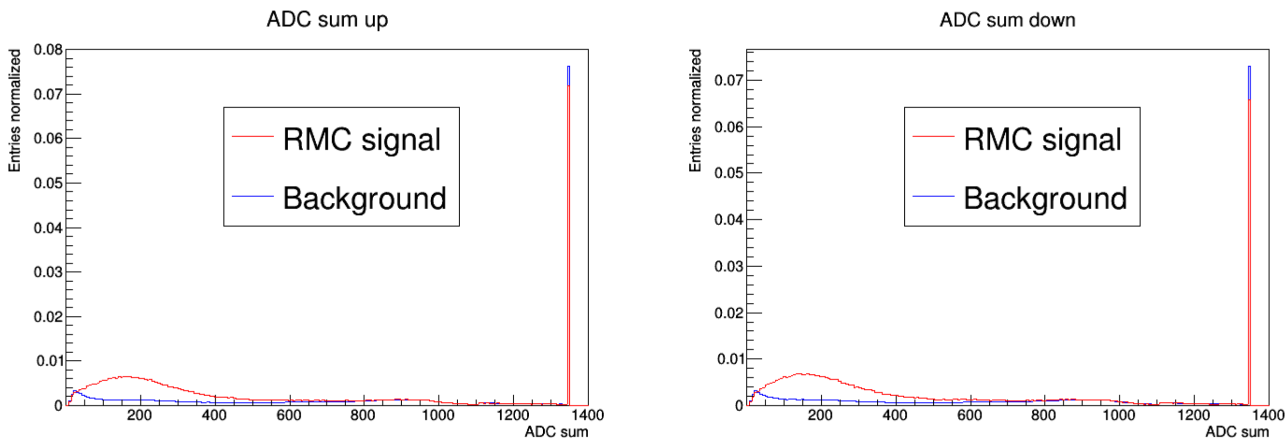

(a) (b)

Figure 6.8: ADC sum distribution, hit with no neighbor (ADC sum = -1) have not been ploted(a) for up neighbor (b) for down neighbor.

6.1.2 GBDT results

While all parameters introduced previously have shown some differences between the RMC signal hit and the background hits, a clear separation is not shown. Thus, it is necessary to combine them. Similarly to chapter 5, a GBDT algorithm is used to separate background hits from RMC signal hits.

The GDBT algorithm is trained with 30k events. The main parameters of the GBDT are the same as shown in section 5.2.2:

- 1000 trees,

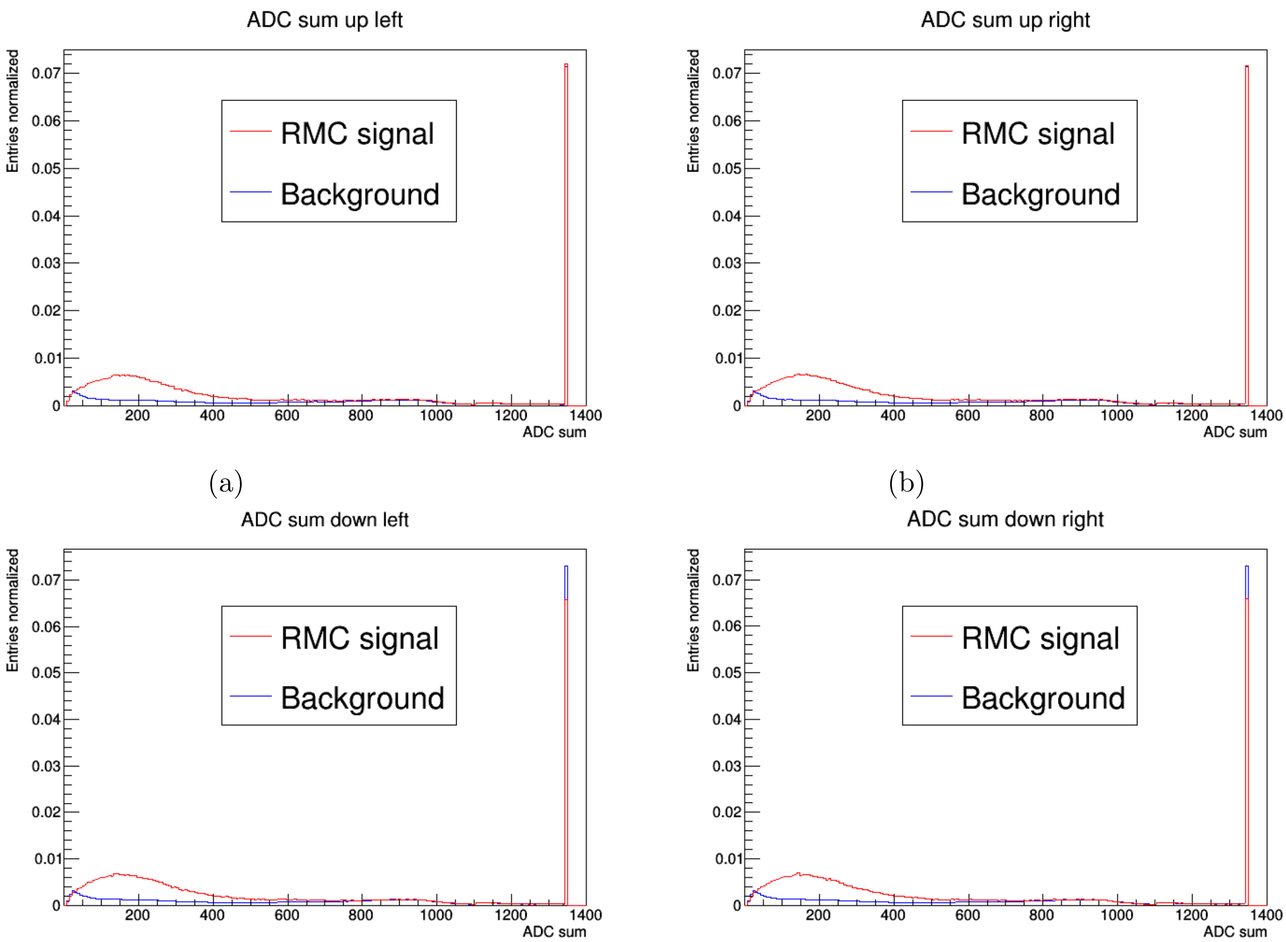

(a) (b) (c) (d)

Figure 6.9: ADC sum distribution, hit with no neighbor (ADC sum = -1) have not been ploted (a) for up left neighbor (b) for up right neighbor (c)for down left neighbor (d) for down right neighbor

- the maximum depth of a tree is 5,
- the binning variable is 20.

Below, one can see the input parameters ranked by their separation power [60]:

- Layer ID — 0.1431
- ADC Sum — 0.1393
- Delta ϕ — 0.1216
- Hit timing — 0.1088
- ADC sum right neighbor — 0.08654
- ADC sum left neighbor — 0.08270
- ADC sum left down neighbor — 0.05557

- ADC sum right up neighbor — 0.05484
- ADC sum left up neighbor — 0.05414
- ADC sum up neighbor — 0.05376
- ADC sum right down neighbor — 0.05356
- ADC sum down neighbor — 0.04617

A separation power of 1 indicates a total separation between the background and the signal distribution, whereas a separation power of 0 indicates total overlap between the background and the signal distribution.

The separation power for the extended ADC-sum neighbor (up, up-right, up-left, down, down-right, and down-up) is lower because there is less chance to have a hit neighbor there. For the RMC signal, there is a 90% chance to have either a neighbor on the left, right, or both, whereas for up and down, this chance drops to 45%. This difference is explained by the CDC geometry and the RMC signal trajectory. First, when the particle enters and passes through one layer of the CDC, due to the cell size and the particle trajectory, it almost always leaves two hits. Thus, there is a high chance that a signal hit will be followed by a left or a right hit or both. On the other hand, the CDC is a stereo chamber, as explained in the chapter 2; thus, tracks projected in the XY plane at a Z that is different from the track Z position will cause a shift between layers. This shift can be as much as six cells wide. Because the projection was chosen in the middle of the chamber by default, the likelihood of the chosen Z matching the one of the trajectory is low. Thus, the probability of having a neighbor up and down is greatly reduced. This limits the potential of the neighbor feature.

Figure 6.10 shows the distribution of score for signal and background. The background is concentrated on -1, while the signal is concentrated between 0.8 and 1. The background and the signal are well separated.

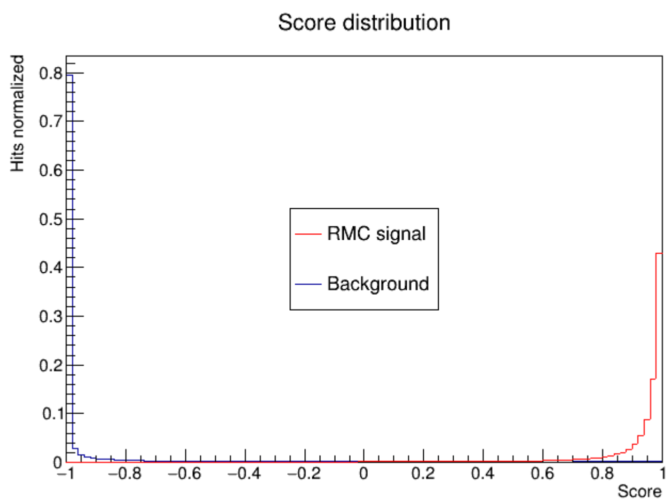

Figure 6.10: Score distribution for signal and background hits

A ROC curve can be created in the same manner as described in section 5.2.3. Figure 6.11 shows the resultant ROC curve for hit filtering. The background rejection corresponds to the number of background hits that were rejected, and hit efficiency corresponds to the number of signal hits that were kept. It is possible to achieve an efficiency of 94% and a background rejection of 94% by using only the GBDT. However, 94% background rejection is still not enough, as it means that there are on average 74 background [1] hits left in the frame.

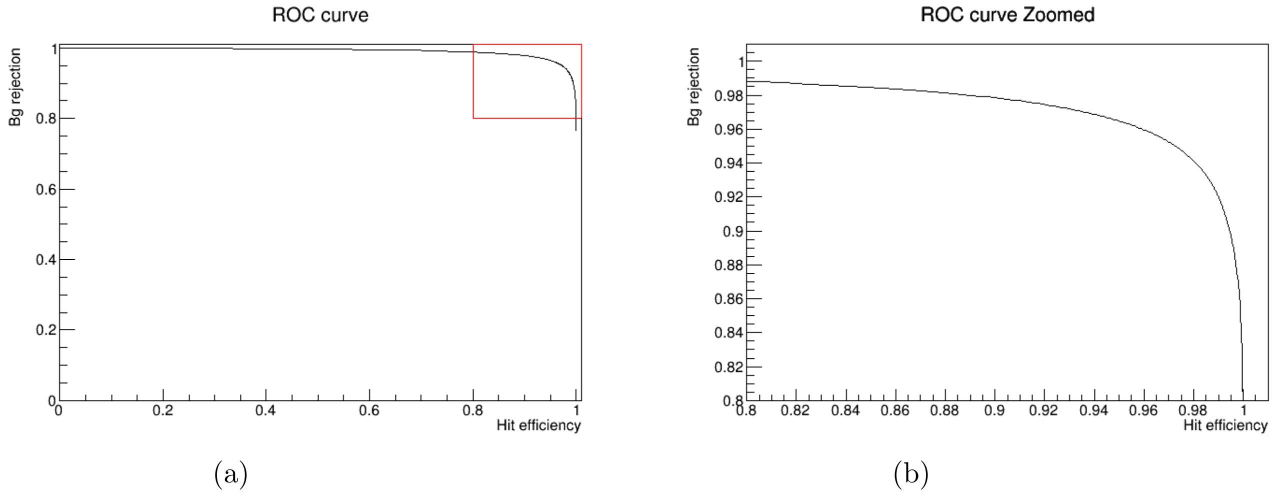

Figure 6.11: Hit filtering ROC curve. (a) full range , (b) Zoom on the right corner

Figure 6.12 shows a typical event projected in the middle of our detector for different cuts on the GBDT score with the event corresponding efficiency and background rejection. As the score increases, the number of background hits in the event display greatly decreases, with the exception of hits around the RMC signal hits. The signal hits are only partially affected.

6.2 Track finding with circular Hough transform

While the denoising procedure removes the major part of the background hits in the frame, it is not able to remove hits close to the electron and positron tracks. Furthermore, it cannot be used to separate the electron and positron tracks. For these two reasons, CHT is used as a complement to GBDT.

6.2.1 Circular Hough transform concept

In a two-dimensional space a circle of center C(a, b) with a radius R can be described by:

$$(x - a)^2 + (y - b)^2 = R^2. \tag{6.1}$$

If one takes a few points (C$_i$ of coordinate (x_i, y_i)) that satisfy the equation above then it is equivalent to:

$$(a - x_i)^2 + (b - y_i)^2 = R^2. \tag{6.2}$$

[1]Originarily, around 2k hits were generated per event. The number of hits was then reduced by 42% thanks to a cut in the analysis time window.

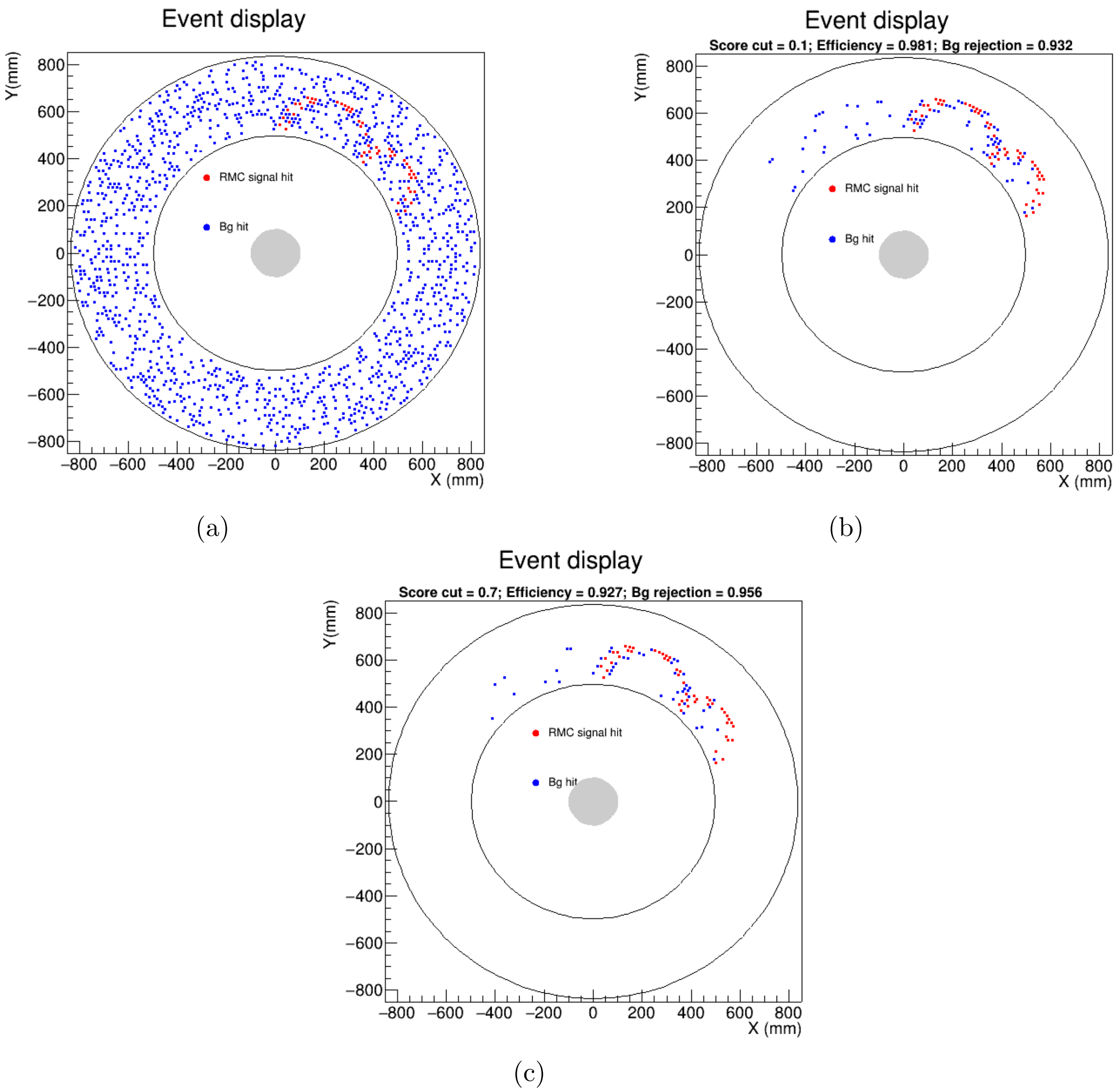

Figure 6.12: Projection of background and signal hits in the middle of the detector. (a) No selection on the hit, (b) hits with a cut on GBDT score superior to 0.1, and (c) hits with a cut on GBDT score superior to 0.7

This means that if one knows the coordinates of N points from the circle C with a radius R, one can find the center position of the circle by solving:

$$\begin{cases} (a - x_0)^2 + (b - y_0)^2 = R^2 \\ \dots \\ (a - x_i)^2 + (b - y_i)^2 = R^2 \\ \dots \\ (a - x_N)^2 + (b - y_N)^2 = R^2. \end{cases} \tag{6.3}$$

Figure 6.13 shows the transform of a circle C in the Hough space.

In practice, because all the points C_n are not on the circle C, instead of solving eq. 6.2, one can draw a circles of radius R around the points C_n and store them in an accumulator, as shown in Figure 6.14. The original circle center, C, is given by the bin in the accumulator with the most entries.

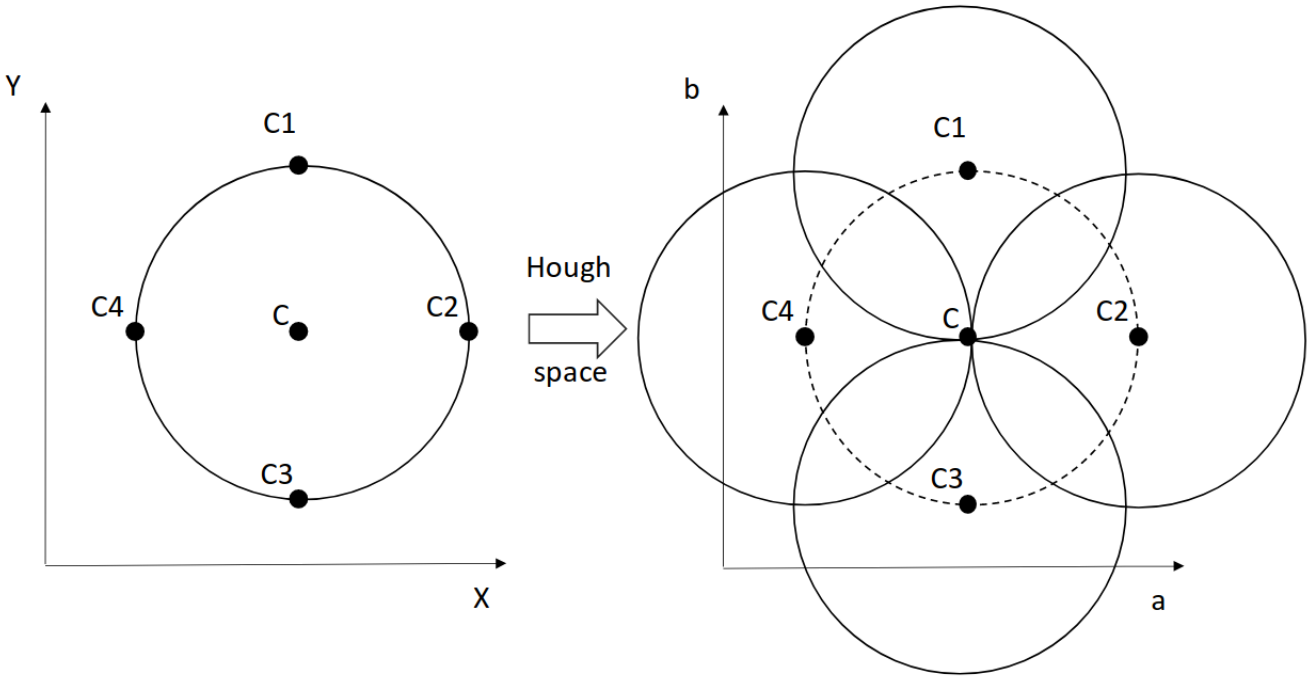

Figure 6.13: Transform of a circle C in the Hough phase space

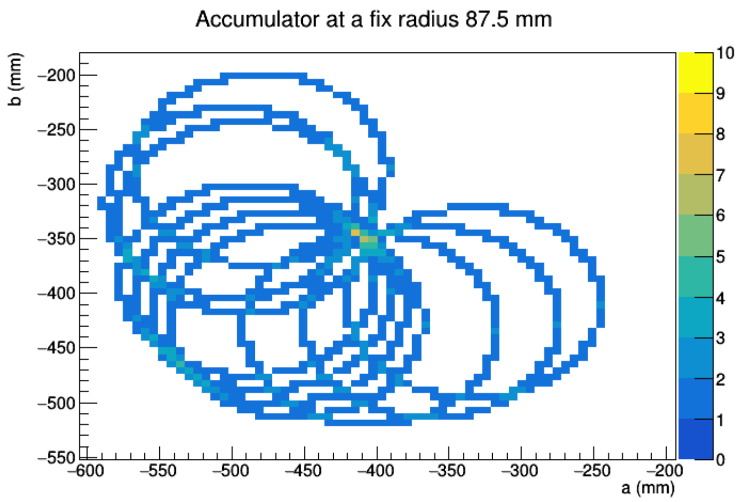

Figure 6.14: Image showing circular Hough transform accumulator at a fixed radius, color shows how many times a bin have been crossed by the different circles

In the case of an unknown radius R, one can use a 3D accumulator in phase space (a, b, R). Instead of drawing a circle, one can draw a cone with the hits positions as the starting point. Figure 6.15 shows the 2D slices in the (a, b) phase space of the accumulator for 3 different values of R. The maximum values of circle intersections differ depending on the value of R. Out of 10 hits in (b) where the truth radius value is used, there are 7 intersections. (a) and (c) have a number of intersections of 4 and 6, respectively, which is lower than the truth.

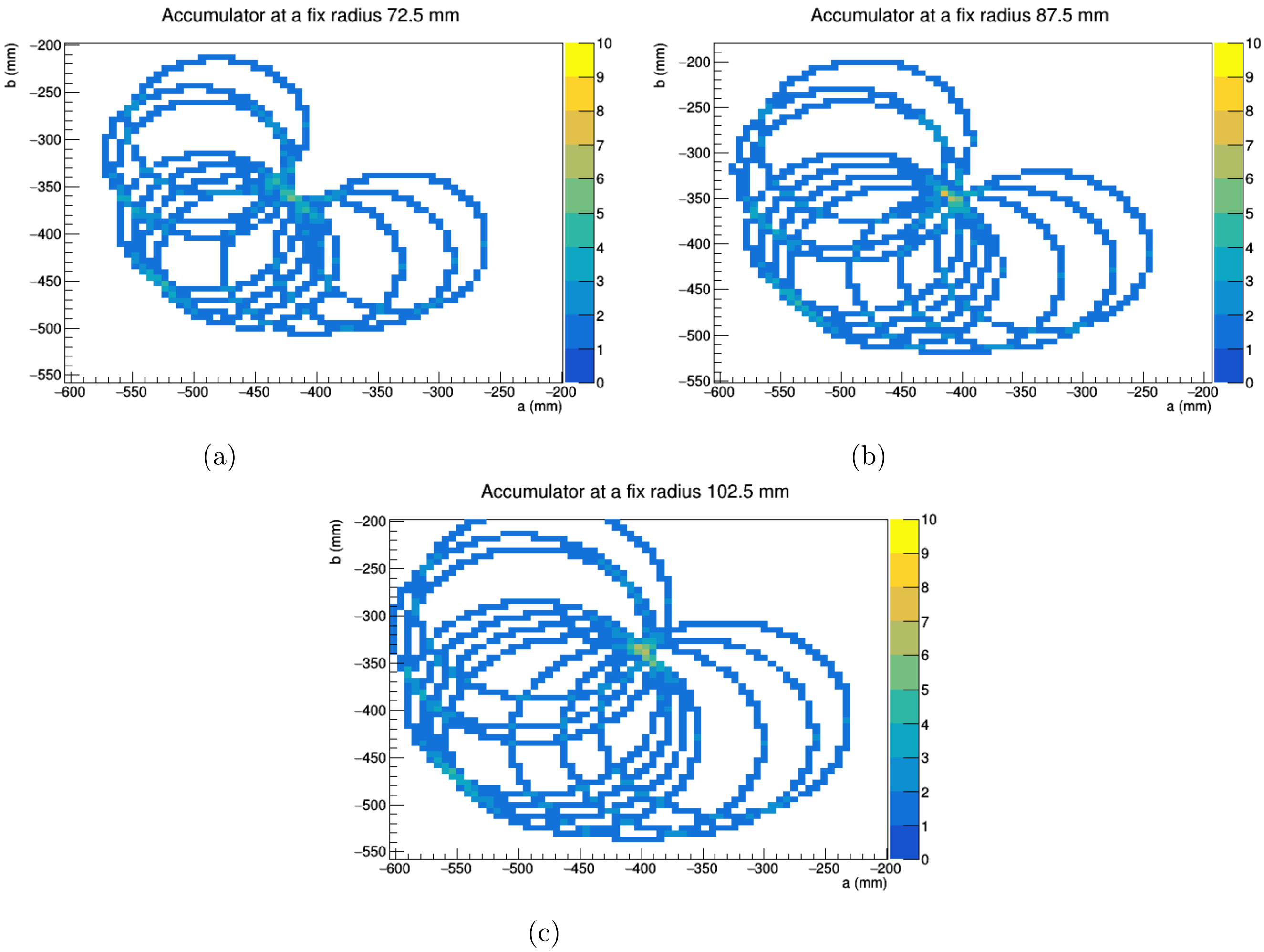

Figure 6.15: Circular Hough transform accumulator projection for 3 differents radius. (a) R = 72.5 (b) R = 87.5 (real radius) (c) R = 102.5

Therefore, by taking the position (a, b, R) giving the largest value of intersection, the original circle parameter can be reconstructed.

6.2.2 Circular Hough transform usage for the RMC Analysis

In the RMC analysis, two circles (the electron and the positron tracks) should be extracted. To do that, in the RMC analysis, the CHT is divided into two steps:

- a first CHT to find one track, either electron or positron, and
- a second CHT to find the other track, either electron or positron, by masking the first Hough transform results.

As explained in section 2.2.3, the CDC is arranged in 20 concentric sense layers with alternating positive and negative stereo angles. Due to this, one track appears to be separated into two circles: one circle on wire with an even layer id and one circle on wire with an odd layer id. To retrieve the track as precisely as possible, each step of the analysis includes three Hough transforms: one on all hits, one on even layer hits, and one on odd layer hits. If the Hough transforms on the even- and odd-layer projection disagree, the Hough transform on all-layer projection is used as a voting scheme to be sure to only take one trajectory per step.

Dividing the Hough transform, between the even- and odd-layer projection, affects the number of hits that can be used to find the associated circles. For this reason, only events in which both the electron and positron tracks reach the fifth layer of the CDC were considered in this study.

Finding the first track using CHT— Voting system

The idea is to retrieve only one circle solution per circular Hough transform. The all-layer projection Hough transform is used as a vote in case the results from the even- and odd-layer projection are inconsistent.

There are three possible outcomes:

- all the Hough transform results agree with each other,
- results on the even- and odd-layer projections disagree, but results on all-layer projection agree with either the odd- or even-layer projection result, or
- none of the Hough transform results agree.

Testing the agreement of the even- and odd-layer projections is called the "coherence check". This coherence check is performed by using two parameters: the radius size difference and the center distance between the odd- and even-layer projections. To obtain these parameter true distributions, 20,000 tracks have been fitted with a circle on their odd- and even-layer projections, using the sense wire position projected in the middle of the CDC as the hit positions. Figure 6.16 shows the distribution of these parameters. Both distributions show two peaks; however, the reason for these peaks is slightly different. First, the difference in radii between the even- and odd-layer projections is due to the longitudinal momentum of the particle as shown in Figure 6.17 (a). At high longitudinal momentum, the difference in radius is accentuated. For the center distance difference between the odd- and even-layer projections, the double peak difference is due to the initial longitudinal position of the track as shown in Figure 6.17 (b). The first peak is due to the tracks that start in the middle of the chamber. The second peak shows the track that started at both ends of the CDC.

Figure 6.18 shows an example when the three Hough transform projections agree with each other. In that case, no adjustment need to be made to the results, and the analysis can go to the next step.

Figure 6.19 (a) shows an example of the second case, where odd- and even-layer projections Hough results disagree with each other, but all-layer projection result agrees with the even-layer projection results. In this case, the odd-layer Hough transform is performed again with hits close to the even- and/or all-layer projections Hough transform circles. Figure 6.19 (b) shows the result after re-doing the Hough transform on the odd layer projection.

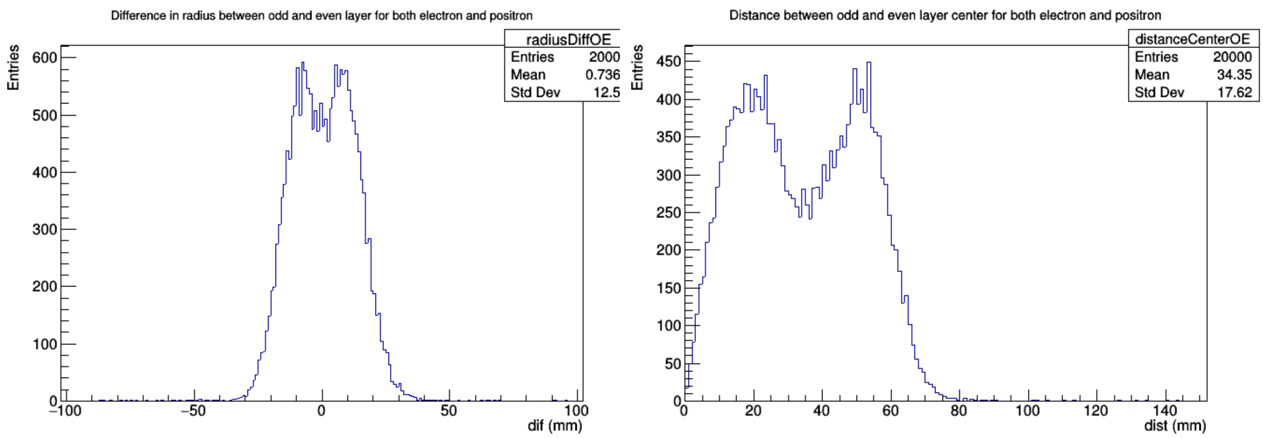

(a) (b)

Figure 6.16: Fine tuning parameters for coherence check between odd- and even-layer projections.(a) shows the radius difference between odd- and even-layer projections circle fitting. (b) shows the distance between odd- and even-layer projections fitted circle center.

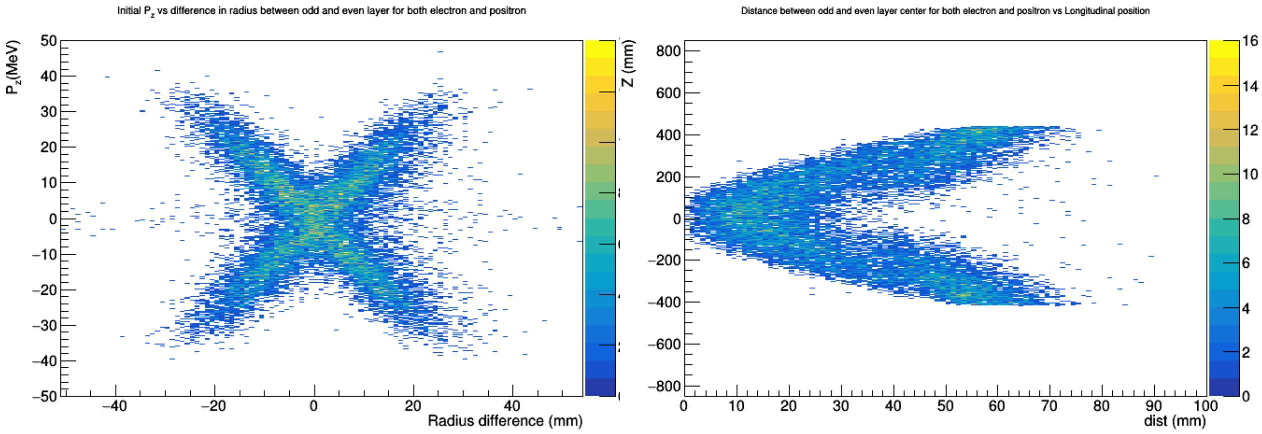

(a) (b)

Figure 6.17: (a) Longitudinal momentum of the particle versus the even- and odd-layer projections radius difference. (b) Distance between odd- and even-layer projection circle center between longitudinal position.

Figure 6.19 shows an exemple of the third case, where all-, odd- and even-layer projections circular Hough transform results disagree with each other. In that case, the Hough transform with the best weight (the hit contribution in the accumulator divided by the radius size) is chosen as the reference. The other two Hough transforms are re-done around hits close to the best circle.

The flow of the algorithm is shown in Figure 6.21.

Finding the second track using CHT with masking

To retrieve the second track, a second CHT is performed after the region found by the first Hough transform is masked. The masking is performed by drawing two lines coming from the detector center, passing by the intersection of the Hough transform result and a circle representing the CDC inner wall. Figure 6.22 illustrates how the masking works on even-layer projection. The same masking is done on all-, even- and odd-layer projections.

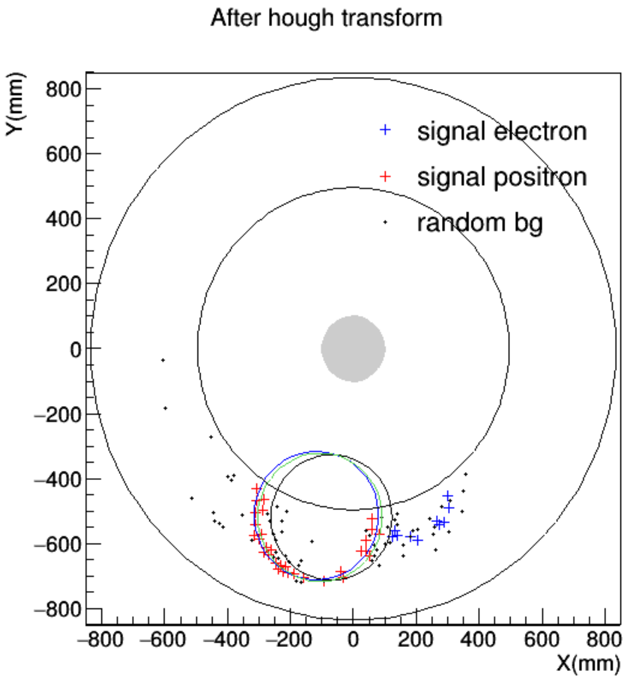

Figure 6.18: Event display with Hough transform result for all 3 projections, hit shown are hit with a GBDT score superior to 0.1.

Once the Hough transform is finished, the coherence check is performed. Figure 6.23 shows a typical event display with the results found by Hough Transform after the second iteration.

Loop of circular Hough transform with masking

The first track found by the Hough transform algorithm can have been influenced by the adjacent track, which provided a partially correct result. Thus, the track found in the second step can be masked, and the circular Hough transform can be performed to have better precision for the first circle. Figure 6.24 shows a sketch of how repeating the Hough transform and the masking can help the results converge to better ones.

The same principle can be extended, and the result of the $(N-1)$th Hough transform can be masked before performing the Nth Hough transform. The track finding procedure stops when $N = N_{loop}$ where N_{loop} is the number of Hough transforms. N_{loop} is optimized in section 6.5.2. The flow of the algorithm is shown in Figure 6.25.

6.3 Track candidates identification

Track candidates, defined by the Hough transform circles, can be associated with the electron and positron tracks. Due to the magnetic field and the charge of electrons and positrons, one can identify which track is an electron track and which one is a

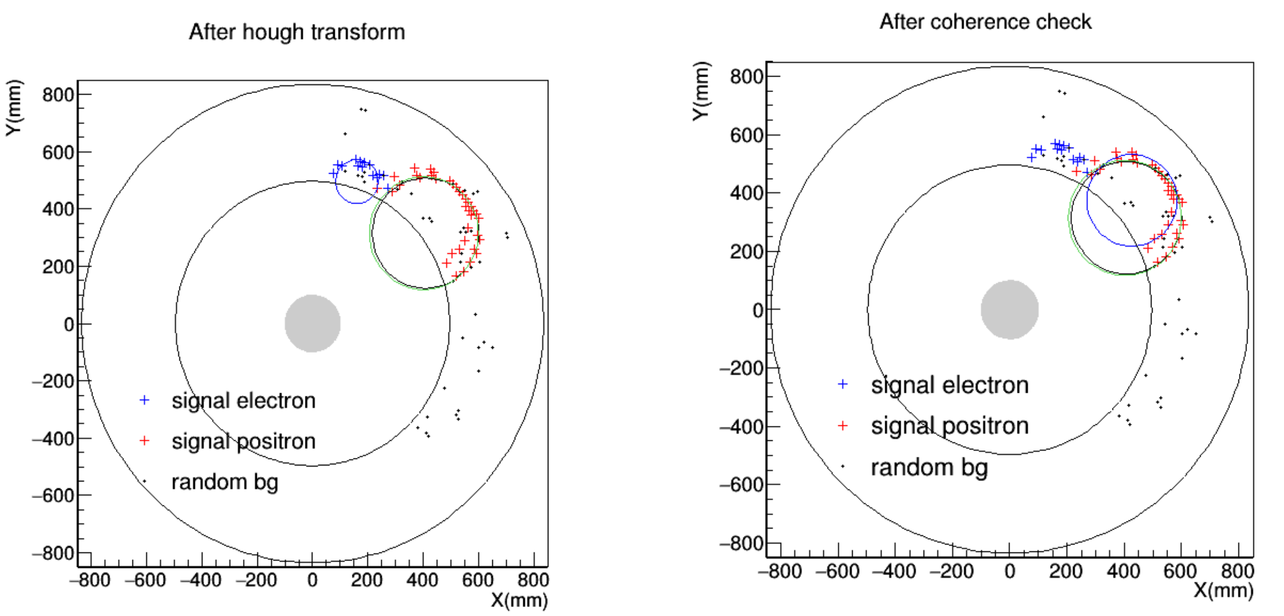

(a) (b)

Figure 6.19: Typical event where odd- and even-layer projections Hough transform don't agree with each others, hit shown are hit with a GBDT score superior to 0.1. (a) shows the Hough transform result all layer and even layer results found the positron track while odd layer found the electron track (b) odd layer Hough transform is re-done.

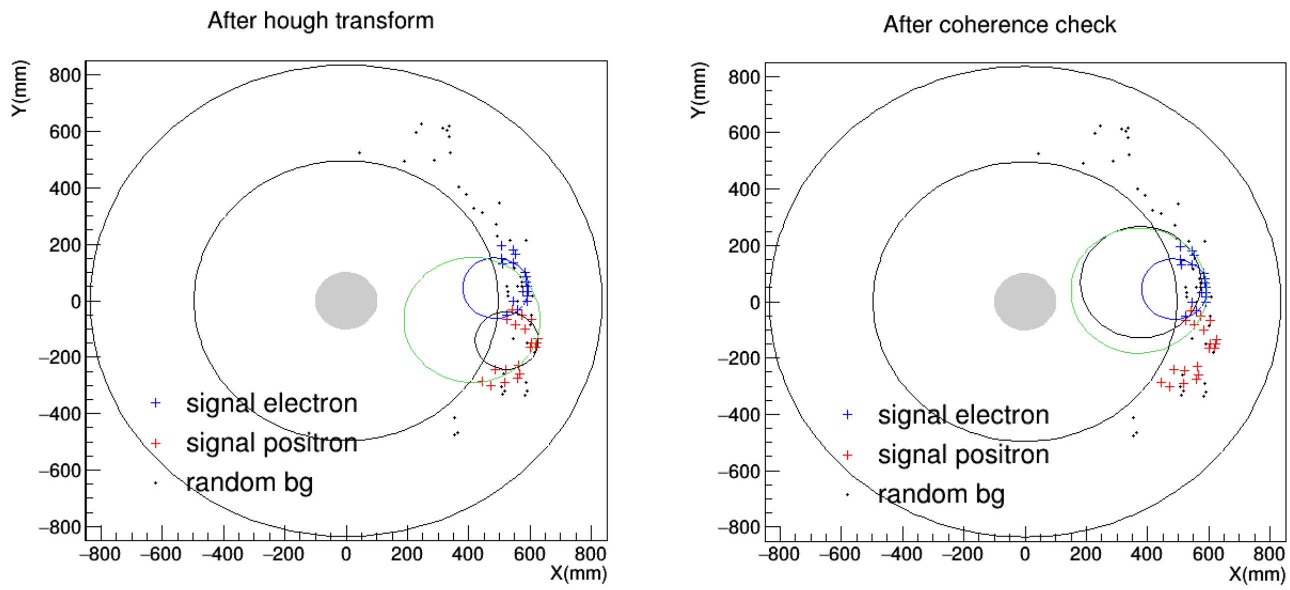

(a) (b)

Figure 6.20: Event where none of 1st the Hough transform agree with each other, hit shown are hit with a GBDT score superior to 0.1. (a) shows that even layer found the positron track while odd layer found the electron track. All layer found a mixture of even- and odd-layer projections track (b) shows the Hough transform result adjusted to the odd layer circle

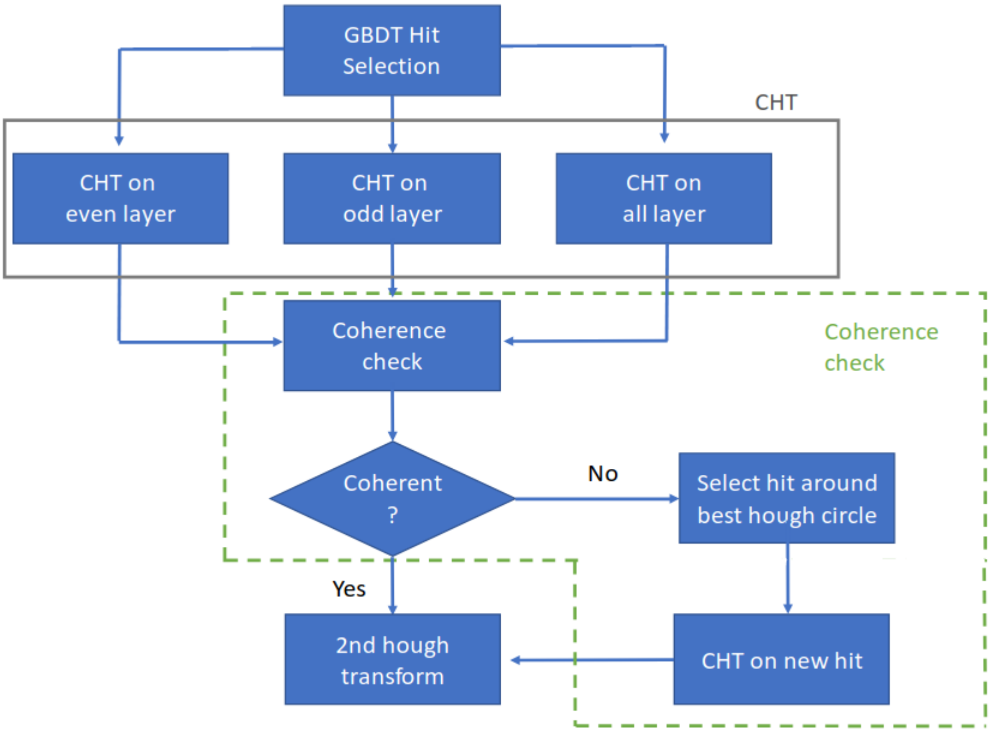

Figure 6.21: Sketch of process flow

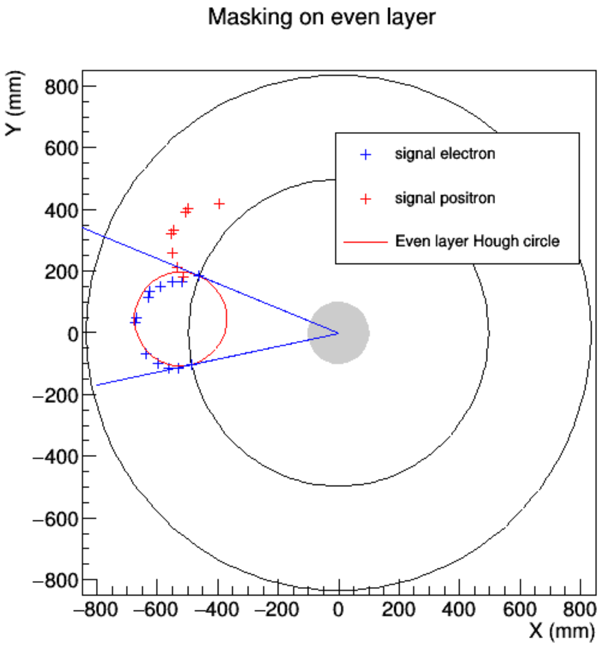

Figure 6.22: Event display with Hough transform result for even layer projection with signal hit. The masked zone correspond to the zone in between the 2 blue line

positron track by comparing the sign of $\widehat{C_aOC_b}$ where O is the center of the CDC, C_a and C_b are the center circles found by the Hough transform. Positive angles are defined as angles going clockwise when looking at the CDC in the same direction as the muon beam. Thus, if $\widehat{C_aOC_b}$ is positive C_a is the electron trajectory, and C_b is the positron trajectory. An example sketch is shown in Figure 6.26. In the sketch

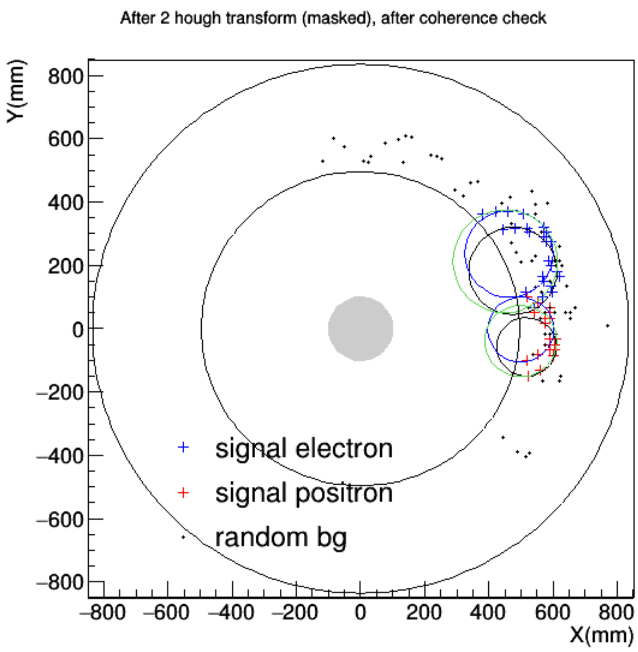

Figure 6.23: Event display with Hough transform result, hit shown are hit with a GBDT score superior to 0.1

$\widehat{C_aOC_b} > 0$, thus, C_a is associated with the electron circle and C_b is associated with the positron circle.

6.4 Extraction of hit candidates

The next step of the procedure is to extract the hits from electron and positron tracks for the track fitting algorithm.

6.4.1 Extraction parameters

Once the tracks are reconstructed, each hit is associated with 3 parameters:

- its GBDT score — s,
- its distance to the electron circle — d_e, and
- its distance to the positron circle— d_p.

The distance to any (electron and positron) circle d_x is:

$$d_x = D(H, C_x) - R_x. \tag{6.4}$$

Where x can either be e for electron or p positron, $D(H, C_x)$ is the distance between the hit H and the circle center C_x, and R_x is the circle radius. With that definition d_x is positive for hit outside the circle, and negative for hit inside of the circle. Figure 6.27 shows the distance distribution to the electron circle d_e. The background hit number grows larger as a function of the distance. The background distribution is asymmetric for one reason: the transverse momentum of both the electron and the

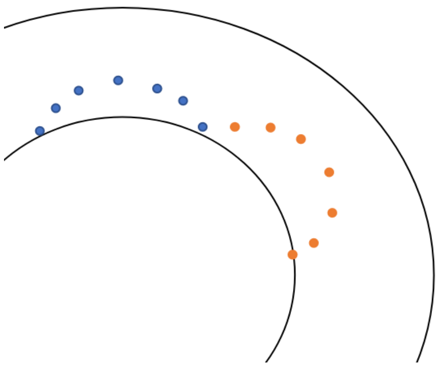

(a) Electron (black) and positron (red) schematic wire hit

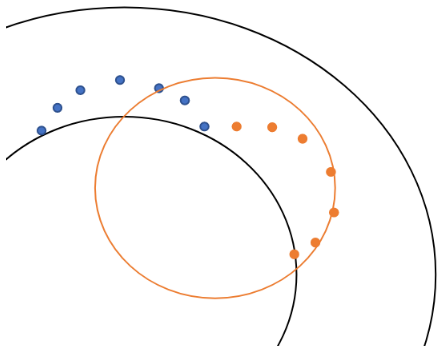

(b) Result of the first circular Hough transform. Biased by the positron hits

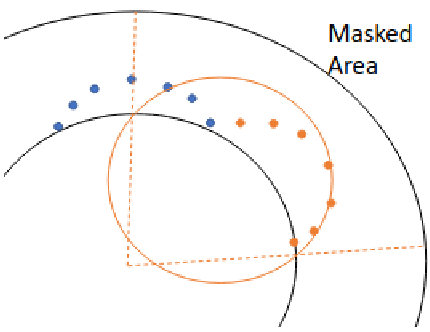

(c) Masking of the region of the 1st Hough transform results

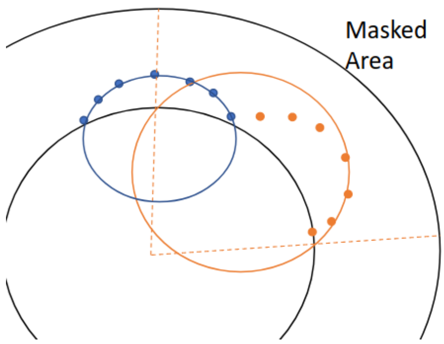

(d) Second Hough transform finding the positron hits. It somehow recovered the hit that were masked

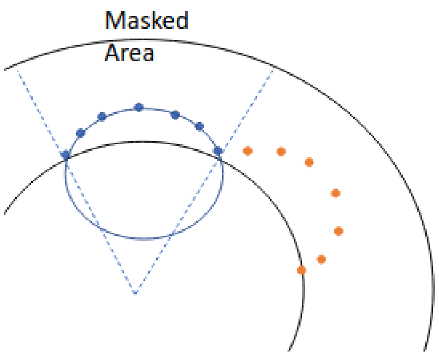

(e) Masking the region of the 2nd Hough transform results

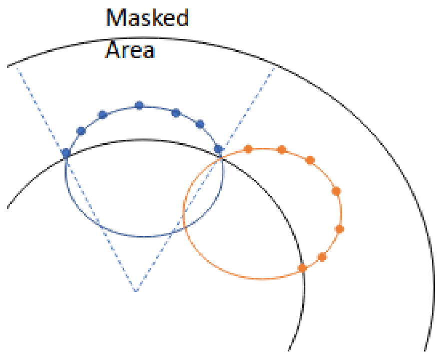

(f) Third Hough transform results.

Figure 6.24: Circular Hough transform and masking scheme loop sketch.

positron is limited in the chamber, thus their track radius is small, which limits the number of possible hits inside the circle from -100 to -40 mm. Thus, to retrieve the hit based on d_x, one can differentiate between hits inside and outside the circle found by the Hough transform and apply two cuts: a lower cut and an upper cut.

Thus, hit candidate for electron (positron) are hit that pass the conditions:

- $s > S_t$,
- and $R_d < d_e < R_u$ ($Rd < d_p < R_u$).

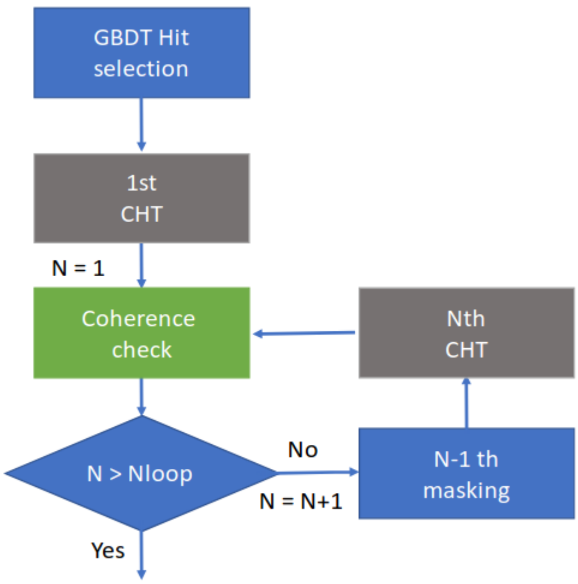

Figure 6.25: Hit filtering and track finding algorithm flow with CHT loop. The coherence check and 1st and Nth CHT are shown in more detail in Figure 6.21

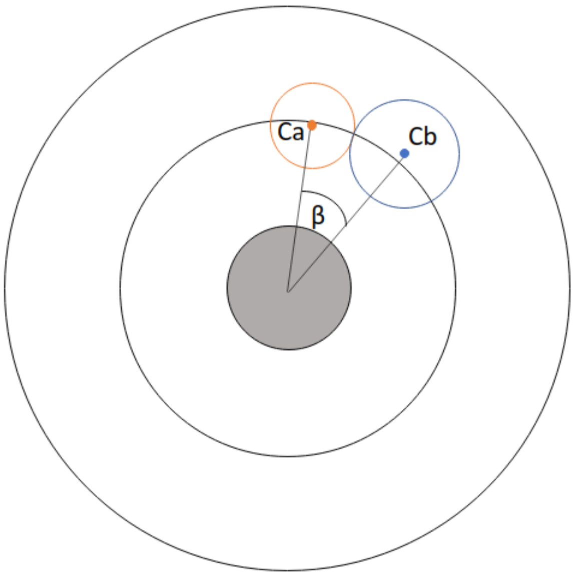

Figure 6.26: Sketch of how to identify which track is from the electron and which is from the positron. In these case, C_a is the electron trajectory and C_b is the positron trajectory

where S_t is the score threshold, R_d is the minimum distance to the circle, and R_u is the maximum distance. The three parameters are optimized in Section 6.5.

6.4.2 Hit Efficiency and purity

To quantify the goodness of the hit extraction, two parameters can be defined:

$$P_u = \frac{N_s}{N_{TR}}, \tag{6.5}$$

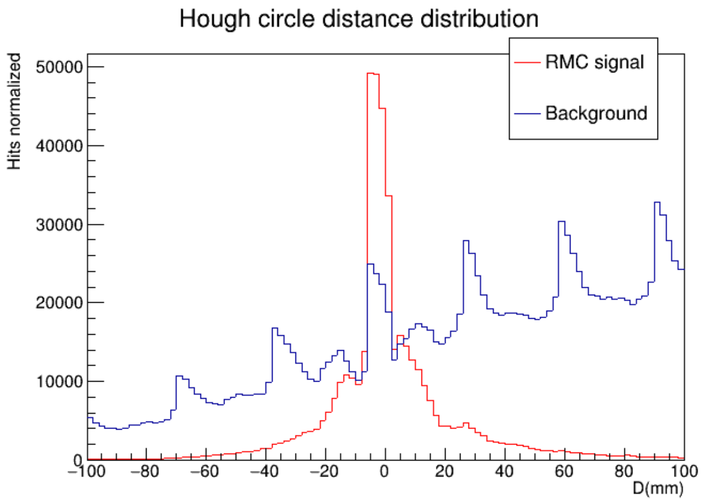

Figure 6.27: Distance distribution between the electron circle found by Hough transform and background (random background) and signal hits (electron hits)

and:

$$E_{eff} = \frac{N_s}{N_T}, \tag{6.6}$$

where P_u is the hit purity, E_{eff} is the hit efficiency, N_s is the number of signal hits that were extracted, N_{TR} is the total number of hits that were extracted, and N_T is the total number of signal hits. N_s and N_T are obtained by using the simulation truth information.

6.4.3 Separating hit for the electron and positron track

To recover hits from the electron and positron track there is two possibilities:

- Method 1: one hit can only be associated with one track, either the electron or positron track.

- Method 2: one hit can be associated with both tracks, electron and/or positron track.

By definition, the two methods give slightly different results. Method 1, by definition, reduces the risk of attributing an electron hit to the positron tracks or a positron hit to the electron tracks. However, if a hit is misidentified, it is a loss. Thus, this method trades hit efficiency for hit purity. Method 2, by definition, should not lose a hit. The number of electron and positron hits associated with both tracks decreases its hit purity. Thus, this method trades hit purity for hit efficiency.

In [61], the performance of the track fitting algorithm for the COMET Phase-I experiment has been shown for $\mu^- \to e^-$ conversion. Fitting has been performed with 100% hit efficiency, and different levels of hit purity. The study found that when the hit purity falls below 80%, the high momentum tail grows rapidly. Thus, hit purity is a more important parameter. For that reason, method 1 has been chosen.

The hit are associated to electron or positron by using d_e^2 and d_p^2. If a hit has $d_e^2 < d_p^2$, it is associated with the electron track, but if $d_e^2 > d_p^2$, it is associated with the positron track.

6.5 Parameter optimization

A few parameters can be optimized to improve the procedure results. A scan was performed on S_t, R_d, and R_u to determine the best hit efficiency and hit purity. The point where hit efficiency and hit purity are closest to 100% hit effiency and 100% hit purity has been chosen as the best hit efficiency and hit purity as a naive approximation.

6.5.1 Circular Hough transform GBDT operation point S_h

To determine which is the best GBDT score cut threshold for the circular Hough transform, the circular Hough transform was performed at different GBDT score operation points S_h (from 0.1 to 0.9). A scan of the different parameters has been performed following subsection 6.4.1. The best hit purity and hit efficiency have been drawn as functions of the GBDT hit score threshold in Figure 6.28. At a GBDT hit score threshold of 0.7, the hit purity is the highest. However, the hit efficiency is at its best at 0.5 and starts to decrease slowly after this point. Due to the previous study results [61], hit purity is prioritized over efficiency, and the operation point of 0.7 is chosen.

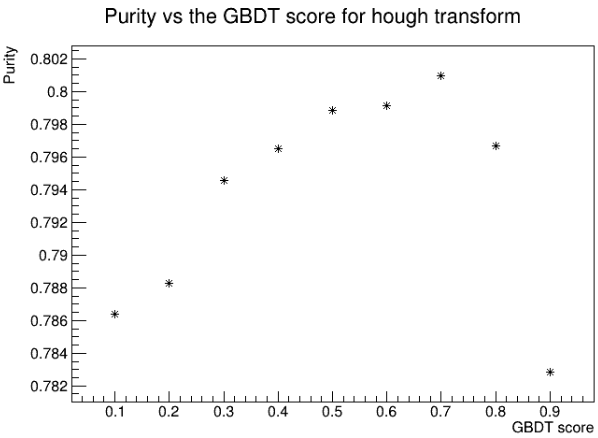

(a) Hit purity

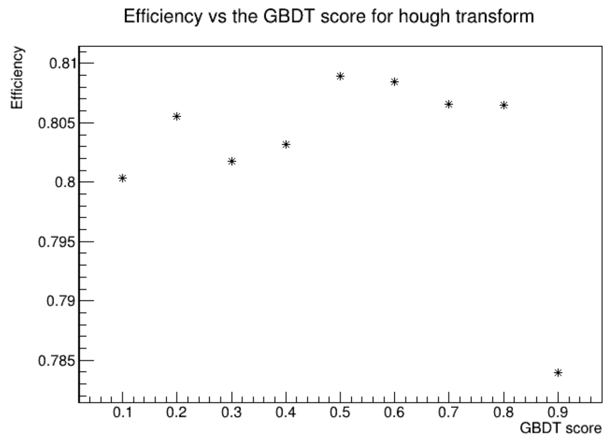

(b) Hit efficiency

Figure 6.28: Hit purity and hit efficiency function of the GBDT score cut before the circular Hough transform

6.5.2 Number of CHT N_{loop}

The algorithm was repeated with different numbers of iterations ranging from 1 to 6 to optimize the N_{loop} parameter. One being the minimal number of iterations required to retrieve both electron and positron trajectories. The best hit purity and hit efficiency have been drawn as a function of the number of iterations in Figure

6.29. Both the hit efficiency and hit purity appear to peak around five iterations. Thus, a minimum of $5 + 1$ Hough transform will be performed.

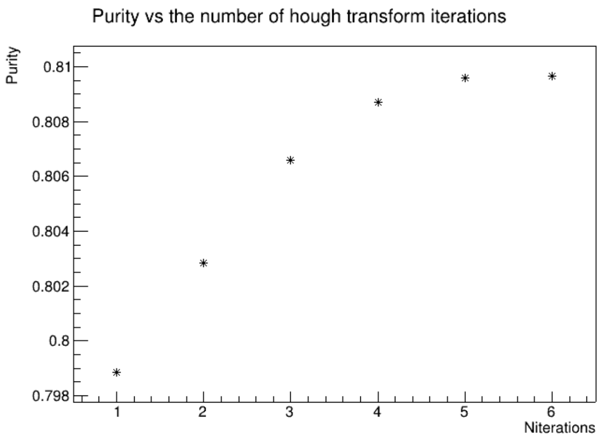

(a) Hit purity

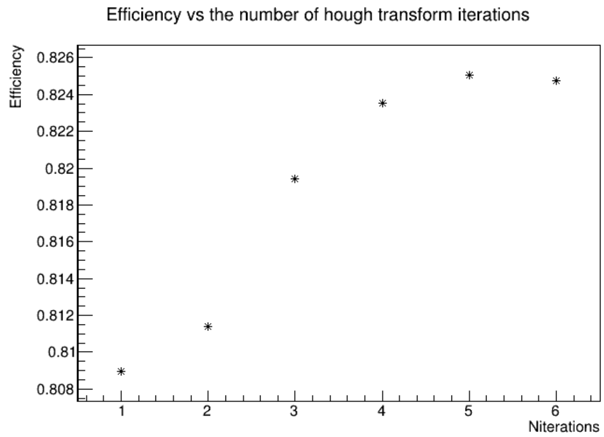

(b) Hit efficiency

Figure 6.29: Hit purity and hit efficiency function of the number of Circular Hough transform iterations. The Circular Hough Transform is working at a score of 0.5.

6.5.3 Hit parameter ADC sum C_{ADC}

The hit has been retrieved using S_t, R_d, and R_u. However, after recovering the hit, the hit purity and hit efficiency can be improved again by putting a cut on the ADC sum C_{ADC}. The ADC sum of recovered hits with S_t =0.4, R_d =-20 mm, and R_u =15 mm is shown in Figure 6.30. By applying a cut requiring the hit ADC-sum to be lower than 600, it helps to remove 30% of the remaining background hits while only losing 2% of the remaining signal hits. Thus C_{ADC} is required to be inferior to 600 ADC-sum.

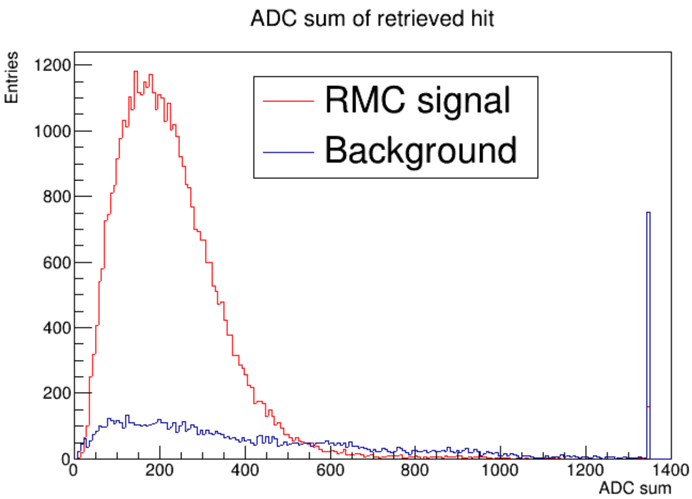

Figure 6.30: ADC sum distribution of hit retrieved with S_t =0.4, R_d =-20 mm and R_u =15 mm

6.5.4 Result: Parameter optimization

The hit filtering, track finding procedures have been optimized to reach 83% hit purity and 82% hit efficiency. To reach this result, the different parameters used are:

- $S_h = 0.7$,
- $N_{loop} = 5$,
- $S_t = 0.4$,
- R_d =-20 mm,
- R_u =15 mm, and
- C_{ADC} =600 ADC-sum.

6.6 Result

On average, a RMC electron (positron) track leaves 17 hits in the CDC. With the track-finding procedure, out of these 17 hits, only 3.1 are lost. Similarly, 2000 background hits have been simulated per event, and out of them, only 2.9 are left per track recovered. The denoising and track-finding procedures can successfully recover the electron and positron hits with a minimal number of hits lost. The track finding event efficiency, defined as the ratio of events where the minimal fitting condition is achieved (at least 5 hits for electrons and positrons are on the Hough transform found circles), to the total number of events, has been evaluated to be 99%. Thus, only 1% of the events are lost in by the track finding procedure.

Chapter 7

Track reconstruction procedure

To reconstruct the momentum of the electron and positron, track fitting is performed. The track fitting is implemented using GENeric Track-Fitting Toolkit (GENFIT), which is based on the Kalman filter. The Kalman filter assumes that the true state x_k at time k is derived from the state at time $k-1$:

$$x_k = F_k x_{k-1} + w_k, \tag{7.1}$$

where F_k is the state transition model which is applied to the previous state x_{k-1}, w_k is the process noise assumed to be a gaussian centered on 0. In parallel the measurement z_k is given by:

$$z_k = H_k x_k + v_k, \tag{7.2}$$

where H_k is the observation model and v_k is the measurement noise assumed to be a gaussian centered on 0.

In the example of fitting a charged particle going through a detector, the Kalman filter will need to be initialized by a seed to have a *starting state*. It will then propagate this *starting state* by using Eq. (7.1), where F_k assumes the trajectory of a charged particle in a magnetic field, while w_k is taking into account the different ways that the particle trajectory can change (scattering and so on). Then, the measurement will be compared with the prediction made by the Kalman filter with Eq. (7.2). The difference between the prediction and measurement will be used to calculate the Kalman gain. The Kalman gain is used to properly weight the current measurement and avoid giving it too much weight if it disagrees with the prediction made by the Kalman filter.

Thus, before fitting, there are two steps that are necessary to GENFIT:

- First, the measurements must be ordered. The Kalman filter can reorder sections of a track. However, because the validity of each measurement is determined by the previous agreement between the prediction and the measurement state, the initial ordering of the hits has an influence on the final results.

- Finally, the initial position and momentum of the particles need to be estimated. This is called the seed, and it is needed to start the Kalman filter.

Before showing the results of the fitting, this chapter shows how the hits are ordered and how the initial seed is obtained.

7.1 Organizing the hits

Figure 7.1 shows a sketch of hits organized by the time at which the hit (the ionization of the CDC gas) occurred. However, in the experiment, the time at which the gas is ionized is not properly known. Thus, it cannot be used to organize the hit. Instead, the hits are organized using the hit wire information.

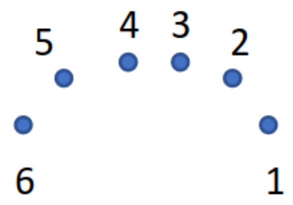

Figure 7.1: Sketch showing electron hits and how they are organizing

First, the hits are organized by decreasing layer ID. In cases of similar layer ID, the hits are ordered by increasing cell ID. Layer ID and cell ID are shown in Figure 7.2. The hits from Figure 7.1 are stored in an array: [4, 3, 5, 2, 6, 1].

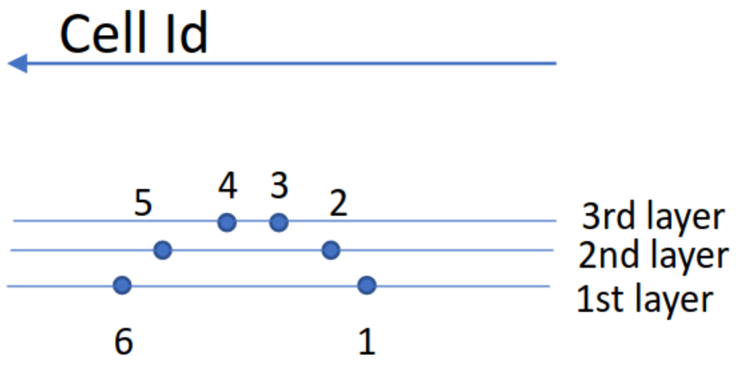

Figure 7.2: Sketch showing the layer id of each hits, and the cell Id axis

Hits from the top layer are recovered first and are stored in the organized array, which gives [4, 3]; the hits left are [5, 2, 6, 1]. As shown in the Figure 7.3, the distance between the hits 5 and 4 and the distance between the hits 5 and 3 are compared. Because the distance between the hits 5 and 4 is smaller than the distance between the hits 5 and 3, the hit 5 is added at the beginning of the ordered array: [5, 4, 3]. The list of left-over hits is given by [2, 6, 1].

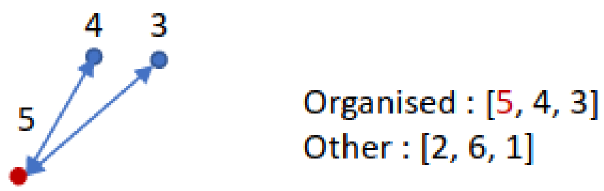

Figure 7.3: Distance comparizon between hit 5-4 and 5-3

The next step is to compare the distance between hits 2 and 5, and between hits 2 and 3. The distance between hits 2 and 3 being smaller, hit 2 is pushed to the end of the ordered array, which becomes [5, 4, 3, 2]. The left-over hits are given by [6, 1]. This algorithm can be repeated until every hit is ordered.

7.2 Calculating the seed

Two seeds need to be determined: the initial momentum ($P_{X_{\text{ini}}}$, $P_{Y_{\text{ini}}}$, $P_{Z_{\text{ini}}}$) and the initial position (X_{ini} , Y_{ini}, Z_{ini}) of the particle at the entrance of the CDC.

7.2.1 Initial momentum

Transverse momentum

Due to the magnetic field, the electron and positron tracks both describe helical trajectories. A circle trajectory is obtained by projecting these trajectories into the transverse plane. The transverse momentum, $P_{\perp_{\text{ini}}} = \sqrt{P^2_{X_{\text{ini}}} + P^2_{Y_{\text{ini}}}}$, is proportional to the radius of the circle trajectory described by the trajectory in the transverse plane. Figure 7.4 shows the distribution of the true initial transverse momentum of the simulation versus the radius found by the CHT for single turn events for the electron and positron. The relationship between the radius and the transverse momentum is basically linear.

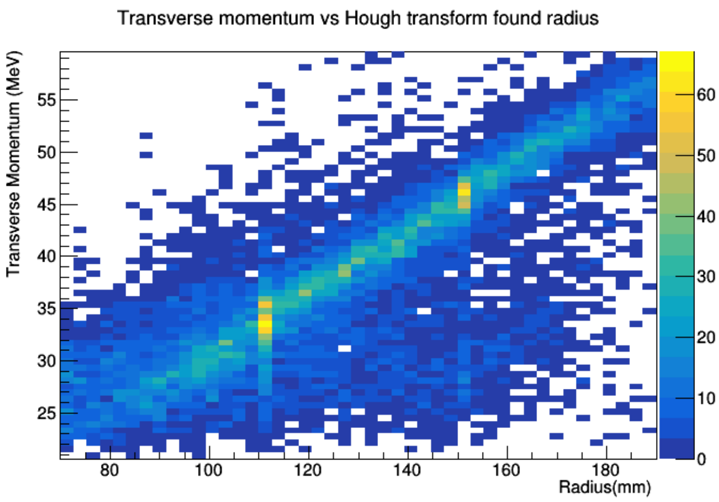

Figure 7.4: Transverse momentum vs. circular Hough transform found radius for electron and positron single turn events

The linear relationship between the transverse momentum and the radius is obtained by fitting a single-degree polynomial function to Figure 7.4. The result is:

$$P_{\perp_{\text{ini}}} = (0.47 \text{ MeV/mm}) \times R \; - \; 28 \text{ MeV}, \tag{7.3}$$

where R is the radius of the circle found by the Hough transform. This relation is used to obtain the initial $P_{\perp_{\text{ini}}}$ from the radii found by the CHT.

For GENFIT, the transverse momentum needs to be decomposed into $P_{Y_{\text{ini}}}$, and $P_{X_{\text{ini}}}$. The momentum decomposition is given by:

$$\begin{cases} P_{Y_{\text{ini}}} = \frac{\overrightarrow{\mathrm{CH}_0}.\overrightarrow{e_Y}}{\|\overrightarrow{\mathrm{CH}_0}\|} P_{\perp_{\text{ini}}}, \\ P_{X_{\text{ini}}} = \frac{\overrightarrow{\mathrm{CH}_0}.\overrightarrow{e_X}}{\|\overrightarrow{\mathrm{CH}_0}\|} P_{\perp_{\text{ini}}}. \end{cases} \tag{7.4}$$

where C is the center of the circle found by the circular Hough transform, H_0 is the first hit in the detector, $\overrightarrow{\mathrm{CH}_0}$ is the vector going from C to H_0 , $\overrightarrow{e_y}$, and $\overrightarrow{e_x}$ are the unit vectors of the X- and Y-axes, respectively. Figure 7.5 shows the definitions of the different parameters.

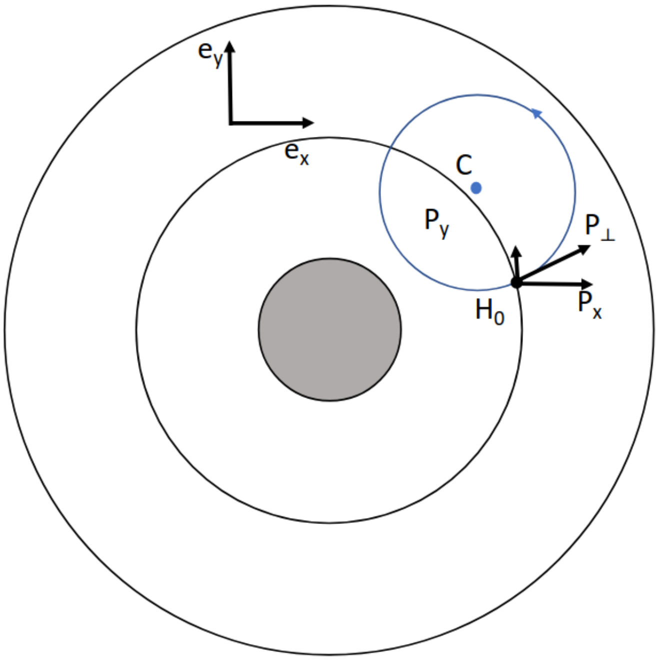

Figure 7.5: Sketch defining the different parameters from Eq. (7.4)

Figure 7.6 shows the correlations between $P_{X_{\text{ini}}}$ ($P_{Y_{\text{ini}}}$) thus obtained and known $P_{X_{\text{ini}}}$ ($P_{Y_{\text{ini}}}$) from the Monte Carlo simulation, proving the goodness of these initial parameters.

Longitudinal momentum

The longitudinal momentum ($P_{Z_{\text{ini}}}$) is difficult to guess before proper track fitting. However, the direction of the particle triggering the CTH is given by the CTH4-fold trigger position (downstream or upstream). Figure 7.7 shows the distribution of the CTH trigger position (downstream or upstream) vs. the Monte-Carlo true initial longitudinal momentum of the particle that triggers the CTH. Using this relation, the longitudinal momentum direction of the particle triggering the CTH can be obtained.

Figure 7.8 shows the distribution of the electron Monte-Carlo initial longitudinal momentum function compared to the positron Monte-Carlo initial longitudinal momentum from the Monte-Carlo simulation. It shows that in the vast majority of

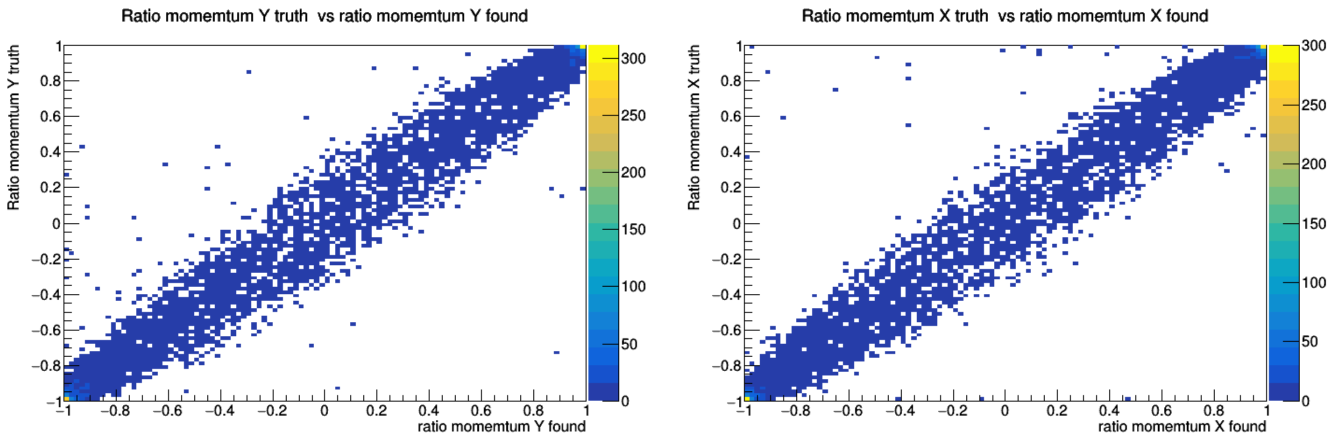

(a) (b)

Figure 7.6: Repartition of the initial transverse momentum on the Y- (a) and X- (b) axes truth versus the ratio found

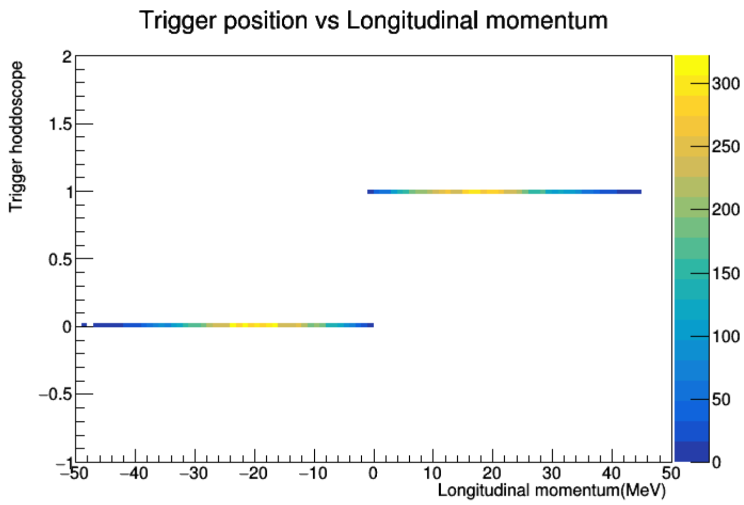

Figure 7.7: CTH 4-fold trigger position (0 = downstream, 1 = upstream) vs longitudinal momentum of the electron or positron that trigger the CTH.

cases, both particles share the same direction along the Z-axis. Thus, by using the trigger hodoscope position, one can guess the direction along the Z-axis of both the electron and positron in 99.9% of the cases.

Figure 7.9 shows the distribution of the initial longitudinal momentum of the electron and positron single-turn events. There is no clear link between the circular Hough transform results and the initial longitudinal momentum. However, due to the event selection criteria (CTH4-fold coincidence, both electron and positron reaching at least the 5th layer), most of the electron and positron have an initial longitudinal momentum distributed around 20 and -20 MeV. Thus, the longitudinal momentum is either chosen as -20 or 20 MeV depending on the trigger position (downstream or upstream).

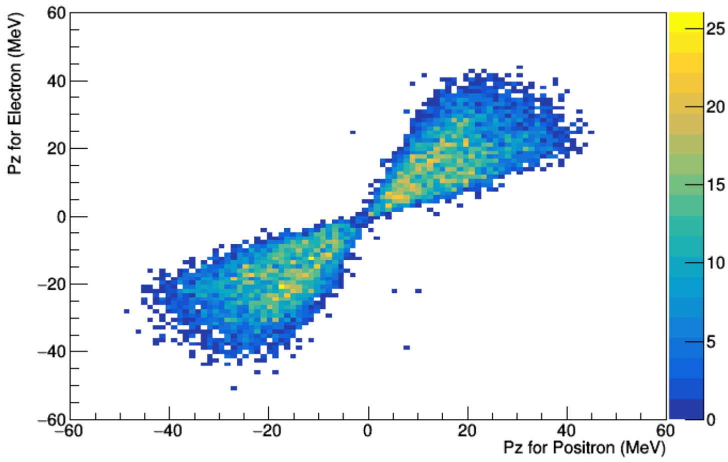

Figure 7.8: $P_{Z_{\text{ini}}}$ for electron vs. $P_{Z_{\text{ini}}}$ for positron from the Monte-Carlo.

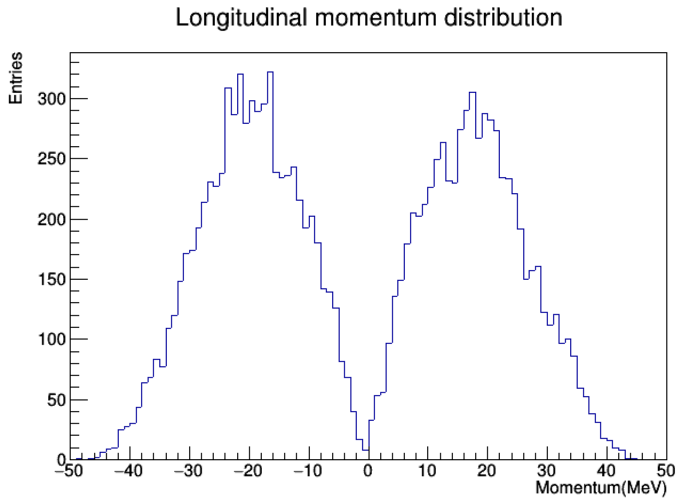

Figure 7.9: Distribution of longitudinal momentum for single turn electron and single turn positron

7.2.2 Position seed

The first wire is determined by taking the first hit when organizing the hits. After obtaining the Z_{ini} position, the precise X_{ini}, and Y_{ini} positions are determined.

The Z_{ini} position is determined by using the angle between the Hough transform circle centers found in the even- and odd-layer projections. Figure 7.10 shows the angle between the odd and even layer circular Hough transform results. This angle is directly linked to the shift between the hit Z positions. If the angle is small or close to 0, the hit happens when the wires on the odd and even layers cross each other. If not, they happen far away from the crossing point.

Figure 7.11 shows the relationship between the truth first hit Z position from the simulation and the angle difference between the odd and even layer CHT found circle. The fitting is used to determine the Z_{ini} position, the fitting parameters are given by:

$$Z_{\text{ini}} = (2.19 \text{ mm/rad}) \times \theta \;-\; 57 \text{ mm}, \tag{7.5}$$

where θ is the angle between the odd and even circular Hough transform found centers.

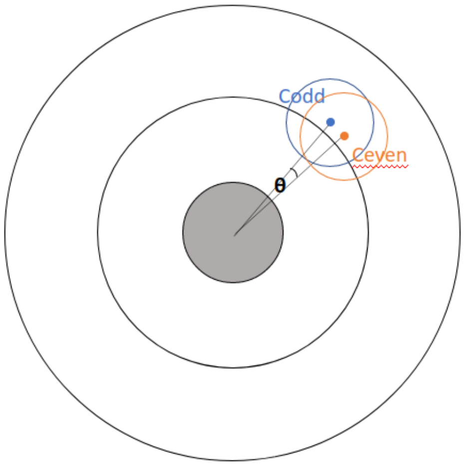

Figure 7.10: Sketch showing the shift between the Odd layer and Even layer Hough transform results

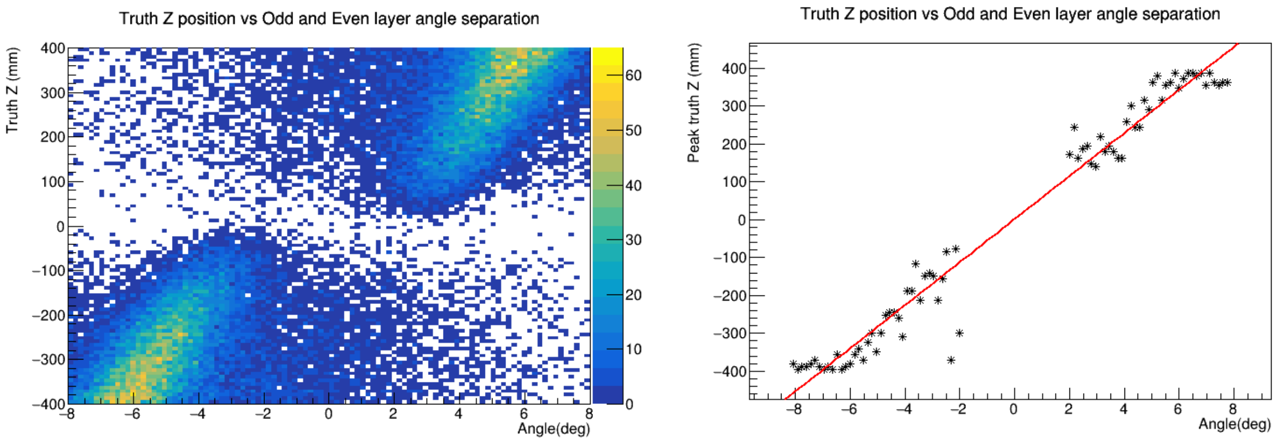

(a) (b)

Figure 7.11: Truth first hit Z position vs Found Hough transform angle shift between the odd and even layer. (b) is showing mean Z distribution truth and 1st degree polynomial fit.

The X_{ini}, and Y_{ini} positions are estimated using the wire 2D projection at the estimated Z_{ini}.

7.2.3 Error distribution on the seed

Figure 7.12 shows the distance between the truth hit position from the Monte-Carlo simulation (the first hit in the detector) and the calculated seed. The peak corresponds to the distance of 0, 1, 2, 3 cells, and so on. In most of the cases, the first hit of the track is found, but sometimes it is one, two, three, or more cells away from the Monte Carlo first hit position. The distribution around the peaks is caused by two factors: drift distance (which the Hough transform ignores) and Z_{ini} projection error.

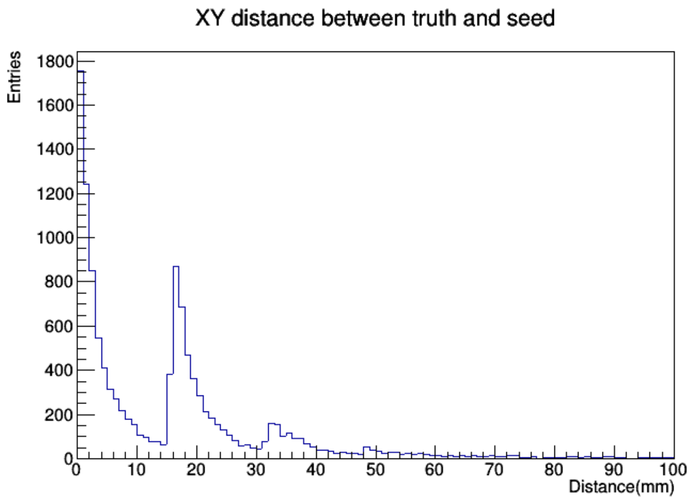

Figure 7.12: XY distance between truth and seed

Figure 7.13 shows the difference between Z_{ini} found minus the Monte-Carlo truth first Z position. The distribution looks like a Gaussian biased toward underestimating the real Z position. This is because the function used to reconstruct Z_{ini} should return $Z_{\text{ini}} = 0$ at $\theta = 0$, but due to the noisy fit, Z_{ini} is equal to -57 mm at $\theta = 0$.

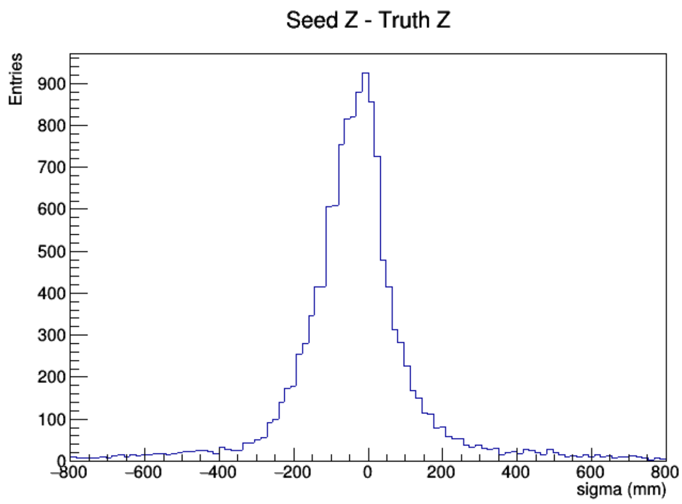

Figure 7.13: Found position Z_{ini} minus truth Monte-Carlo initial Z position

Figure 7.14 shows the transverse momentum seed reconstructed minus the true transverse momentum from the simulation. The error describes one peak and one bump; the peak is centered on 0 MeV and the bump is centered on 15 MeV. The bump indicates that the radius tends to be overestimated.

Figure 7.15, shows the longitudinal momentum used as a seed for the fitting minus the Monte-Carlo simulation truth longitudinal momentum. The error is quite large, but there is no tail above 30 MeV or below -30 MeV.

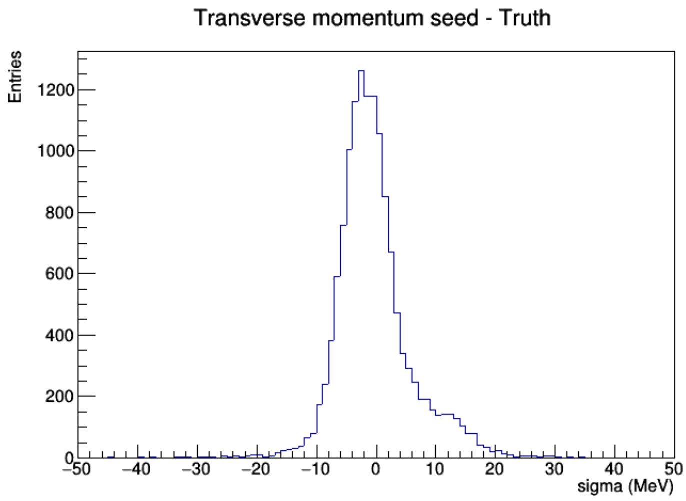

Figure 7.14: transverse momentum seed minus the Monte-Carlo initial transverse momentum

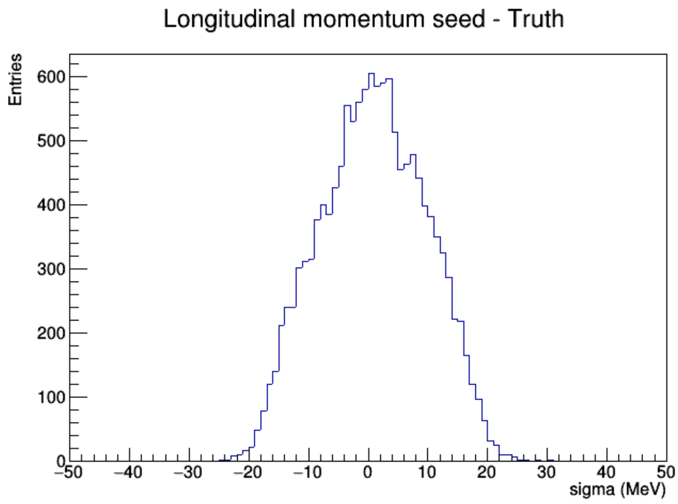

Figure 7.15: Longitudinal momentum found minus Monte-Carlo initial longitudinal momentum

7.3 Reconstruction Process

7.3.1 Helix fitting

For each event, two hit containers (electron and positron hit candidates) have been obtained. The hits have been ordered, and the initial parameters of the tracks have been obtained. They are then fitted using an helix (five free parameters). The helix parameters are adjusted to minimize the distance between the helix and the hit drift circles. The distance of the sum between the helix and the drift circles gives the χ^2.

An event is considered failed when the electron and/or positron track fitting didn't converge and when the Number of Degrees of Freedom (NDF)— the number of fitted hits minus the number of fitted parameters—is smaller than 0. Out of the 81×10^6 RMC events, 4.5×10^6 events have been successfully fitted.

7.3.2 Track selection

Track selection is necessary to improve the resolution of the measurement. For that purpose, two kinds of cuts are applied:

- fiducial cuts, and
- quality cuts.

The resolution, also called "residue" is defined as the reconstructed momentum P_{fitted} minus the Monte-Carlo truth momentum P_{truth} of the particle.

Fiducial cuts

Fiducial cuts are optimized using true information from the Monte-Carlo simulation.

Fitted longitudinal momentum Figure 7.16 shows the distribution of the residue function of the fitted longitudinal momentum for the electron track and the positron track. There is a clear relation between the two when Pz is smaller than -50 MeV or larger than 50 MeV. Furthermore, one knows that, according to the simulation, the longitudinal momentum of the electron and positron cannot be larger than 50 MeV, or smaller than -50 MeV, as shown in Figure 7.9. A fiducial cut is thus applied to reject the track with fitted longitudinal momentum larger than 50 MeV and smaller than -50 MeV.

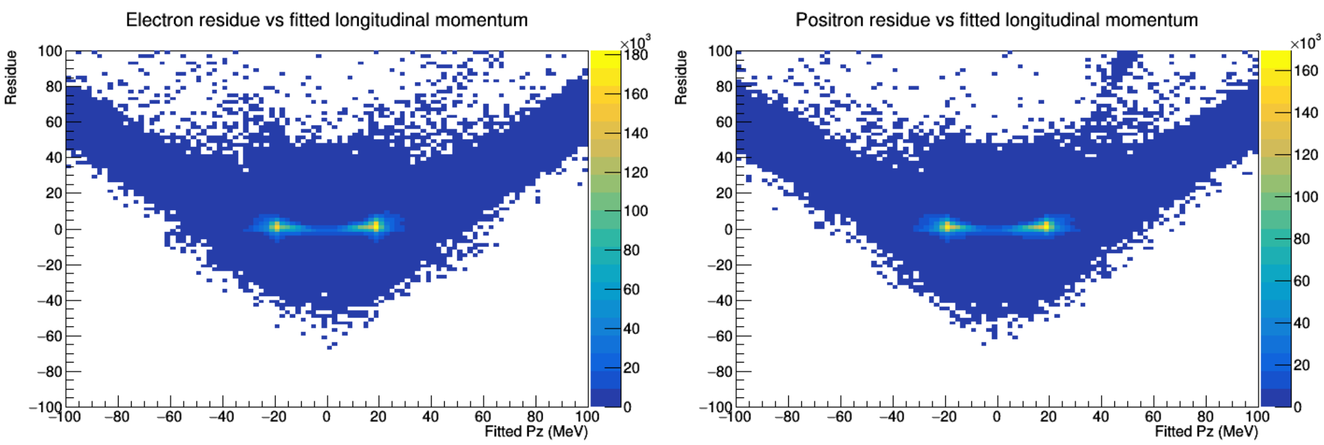

(a) (b)

Figure 7.16: Residue function of the fitted pz for the electron (a), and for the positron (b)

Total fitted momentum The residue function of the fitted momentum is shown in Figure 7.17. There is a clear relationship between the fitted momentum and the tail. According to the simulation, apart from a few rare cases, the momentum of the electron and positron is distributed only between 20 and 60 MeV. A fiducial cut is thus applied to reject the track with a total fitted momentum smaller than 20 MeV and larger than 60 MeV.

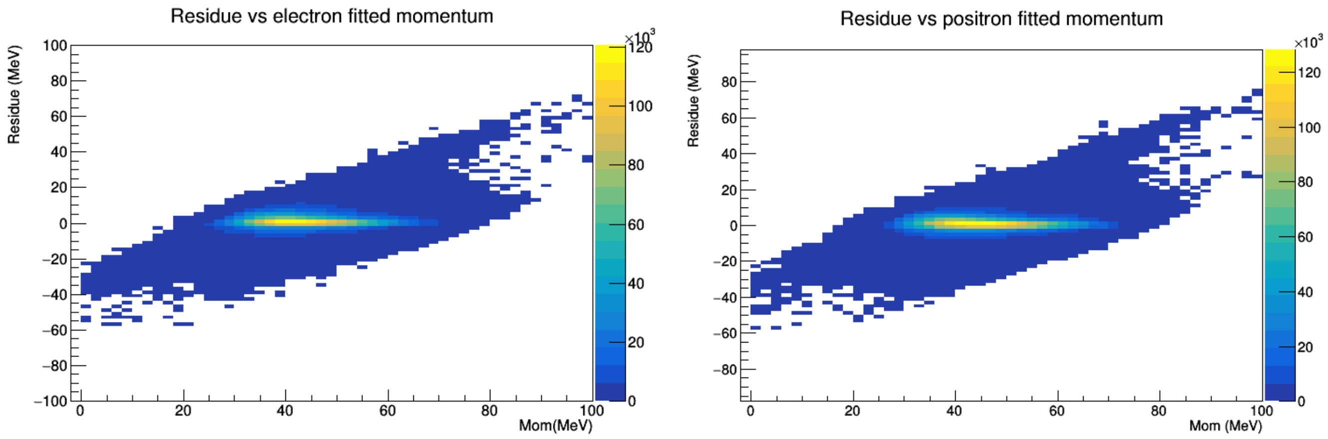

(a) (b)

Figure 7.17: Residue function of the total fitted momentum for the electron (a), and for the positron (b)

Track quality cut

The quality cuts were performed using the fit information to reject badly fitted tracks.
Reduced χ^2 In this study, no relation has been found between the residue and the reduced χ^2. To be consistent with the COMET experiment $\mu^- \rightarrow e^-$ conversion fitting study [18], the reduced χ^2 is required to be less than 2, which corresponds to a p-value of 5% for $NDF = 6$.

NDF requirement A second quality cut is made on the track using the minimal number of NDF. Figure 7.18 shows the residue $((P_{\text{fitted}})_{e^-} + (P_{\text{fitted}})_{e^+} + 2 \times m_e - E_{\gamma \text{ at vertex}})$ for different NDF cut criteria. Increasing the requirement on the NDF helps control the tail in one hand, but it also greatly reduces the number of accepted events. The number of events accepted is shown in Table 7.1.

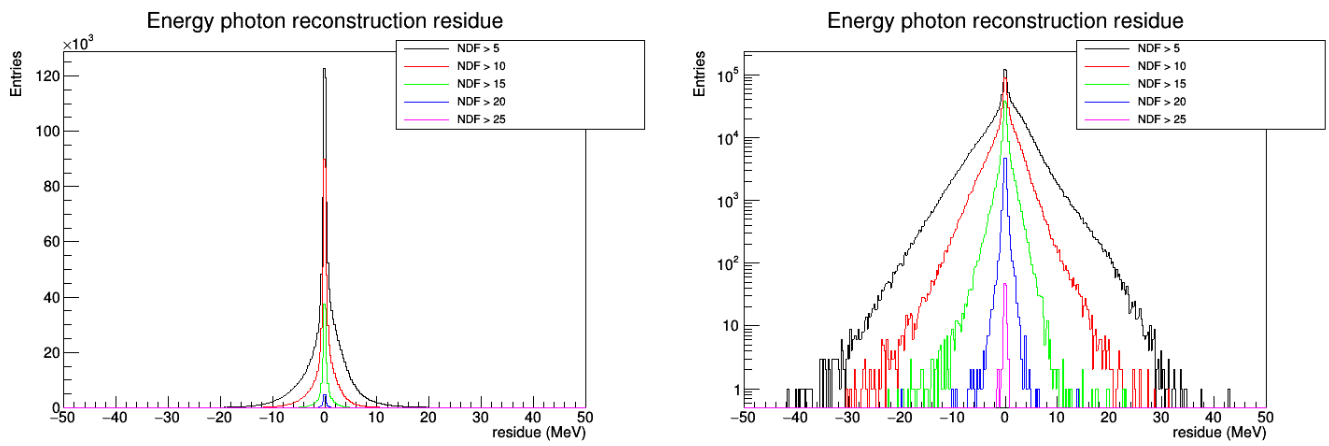

(a) (b)

Figure 7.18: Residue on γ energy $((P_{\text{fitted}})_{e^-} + (P_{\text{fitted}})_{e^+} + 2 \times m_e - E_{\gamma \text{ at vertex}})$ (a) and log scale (b) for different NDF requirement

Table 7.1: Accepted events and fitting efficiency for different NDF cuts. The total number of events is of 10×10^6. The number of event has been calculated for a $k_{\max}$ value of 90 MeV, and 100 running days.

NDF cut	Accepted events	Fitting efficiency	RMC expected event
5	1.46×10^6	14.6%	16 k
10	6.59×10^5	6.58%	3 k
15	1.73×10^5	1.72%	181
20	1.55×10^4	0.155%	0.8

This experiment aims for better precision than the TRIUMF experiment, which accumulated 3 k events with an aluminum target. Thus, to have better statistical precision, a low NDF cut of 5 is applied to be able to accumulate 16k events in COMET Phase-I for a running time of 100 days. Figure 7.19 shows the residue for RMC for both the electron and positron tracks to have $NDF > 5$, and $\chi^2/NDF < 2$.

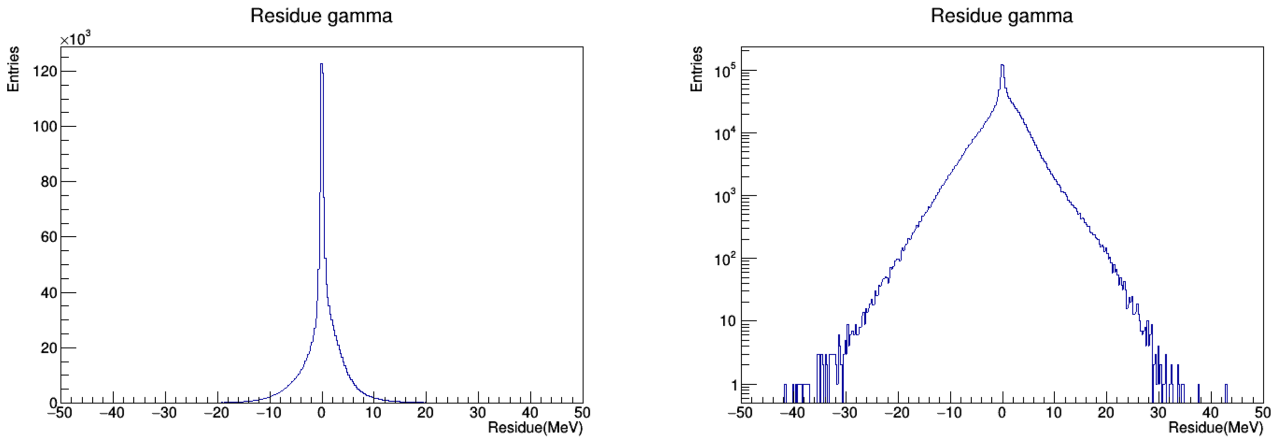

(a) (b)

Figure 7.19: Residue on γ energy ($(P_{fitted})_{e^-} + (P_{fitted})_{e^+} + 2 \times mass_e - E_{\gamma\ at\ vertex}$) (a) and log scale (b)

Result for single turn fitting and multiple turn fitting

The multiple-turns are events in which the electron and/or positron leave the CDC to come back in the CDC. There was no special treatment for multiple-turn events in the procedure. While multiple-turn events (either electron or positron) account for more than 73% of the total events passing the geometrical cut, they account for less than 30% of the total fitted events after track selection. Figure 7.20 shows the residue of fitted electrons and positrons versus the number of turns they made in the detector. The fitted single turn and the fitted multiple turn have similar residue distributions. The fitted multiple turn events, on the other hand, all follow one of the three patterns:

- the particle is quickly stopped after the re-entry into the chamber,
- the particles lose the majority of their energy in the detector inner wall, or

- a large scattering occurs before the re-entry into the detector.

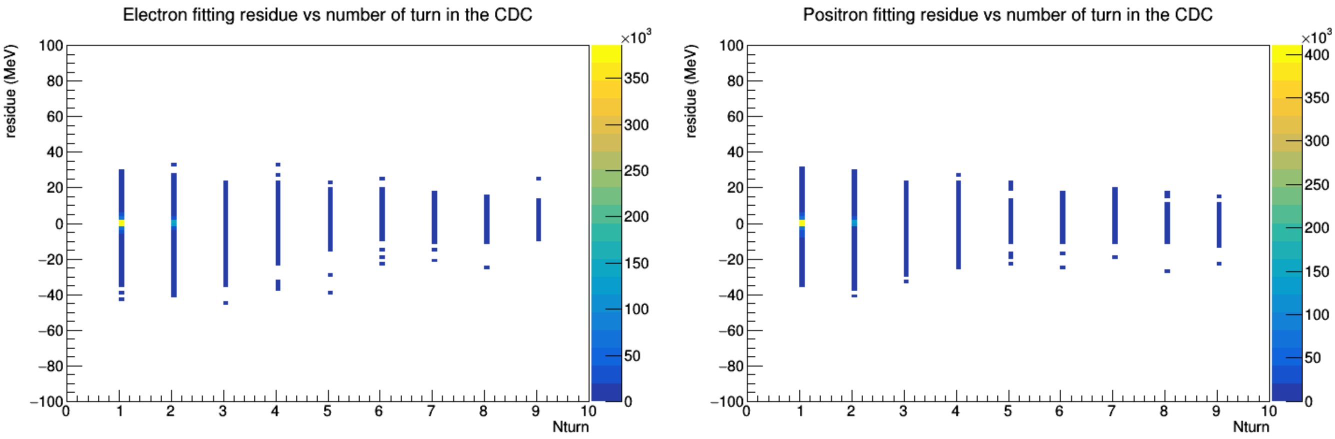

(a) (b)

Figure 7.20: Residue of fitted electron (a) and fitted positron (b) versus the number of turn they make in the detector.

Figure 7.21 shows a sketch of a typical multiple-turns events that can be fitted. Here, the electron track gradually loses energy, so the second turn of the track is well separated from the first turn. The positron loses energy when going out of the CDC; when the particle comes back, its energy and momentum are way smaller, and the trajectories of both turns are distinct. Because of these cases, some multiple-turn events can be successfully fitted.

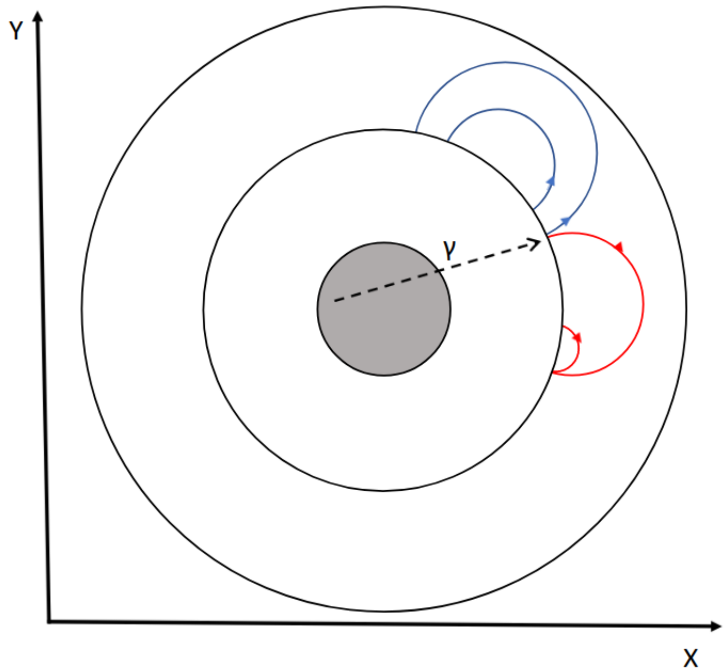

Figure 7.21: Sketch of an event where both the electron and positron track describes two turns in the CDC

7.3.3 Analysis efficiency $\epsilon_{\textbf{analysis}}$

Figure 7.22 shows (a) the true E_γ of the event that pass the quality cut selection, and (b) the reconstructed E_γ. Since the original γs in this study are generated with a flat spectrum, the shape of this distribution represents the analysis efficiency as a function of E_γ.

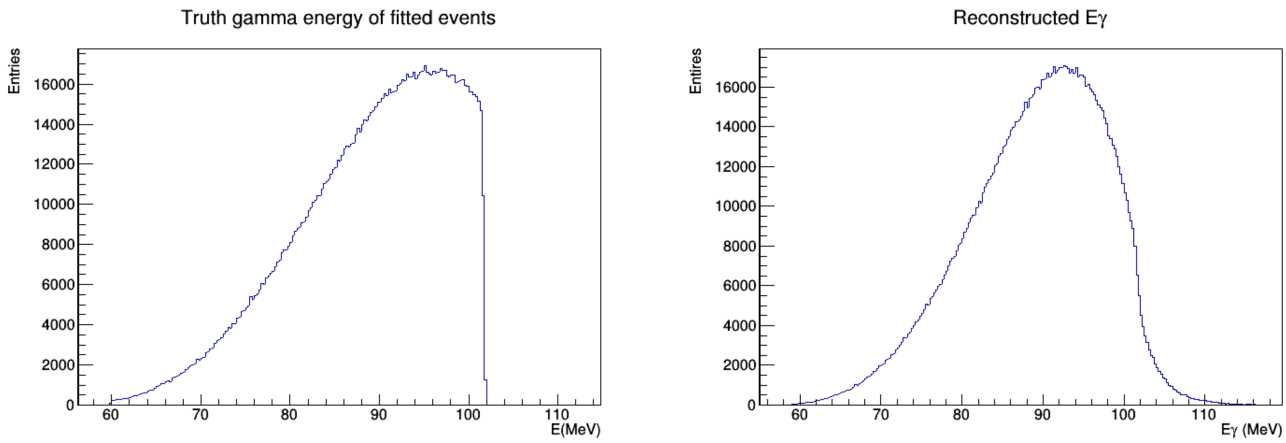

(a) (b)

Figure 7.22: (a) Truth energy of the γ for fitted events. (b) Reconstructed energy of γ

Figure 7.23 shows the analysis efficiency. The efficiency is strongly dependent on the photon energy, as it is easier to reconstruct higher-energy electrons (positrons). For 95 MeV photons, the efficiency is 19%, while it is only 2% for 60 MeV photons.

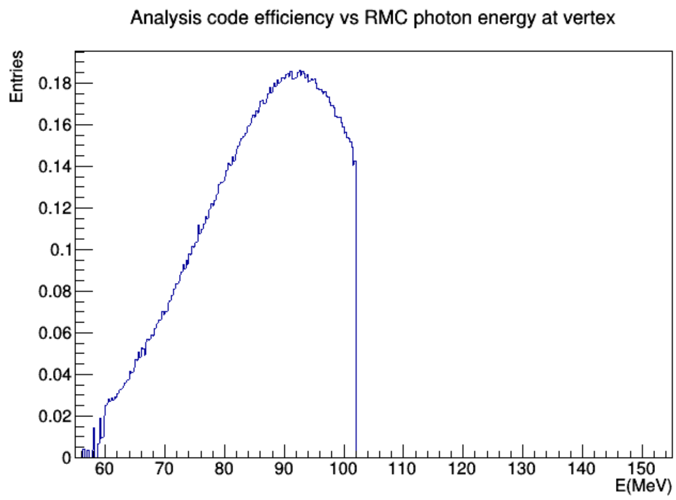

Figure 7.23: Analysis efficiency function of the photon energy before pair creation

Chapter 8

Analysis scheme breakdown

In the previous chapters, the various acceptances and the analysis efficiency have been estimated. A partial analysis breakdown is shown in Figure 8.1. The simulation started with 10^{11} photons simulated with an energy uniformly distributed between 60 and 101.85 MeV. The photon then converts in the inner wall; at this point, the number of photons is approximately 81×10^6. This number is further reduced by requiring a CTH4-fold trigger coincidence and that both the electron and positron reach the 5th layer, for a total of around 10×10^6 γs. At the end of the analysis algorithm 4.5×10^6 have been fitted however most of them have a really high tail and must be cut using quality cuts. The total number of events at the end is approximately 1.5×10^6. Furthermore, by considering the online trigger acceptance and the measurement time window acceptance, the final number of events in this Monte-Carlo simulation study is 378k.

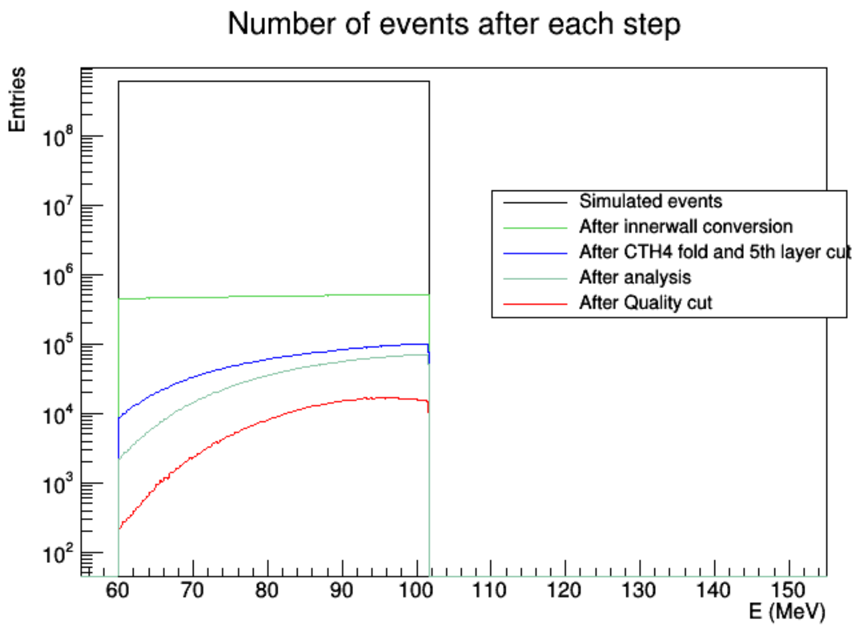

Figure 8.1: Breakdown of the analysis

Those parameters can be used to estimate the number of expected events with the equation previously shown in Chapter 3:

$$\begin{aligned} N_{\text{expected}} =& Y_\mu \times f_{\text{cap}} \times R_{\text{time}} \times R_\gamma \times A_{\text{conv}} \\ & \times A_{\text{geom}} \times A_{\text{MTW}} \times A_{\text{online}} \times \epsilon_{\text{analysis}}, \end{aligned} \tag{8.1}$$

where the various paramaters are resumed in table 8.1. The total number of expected event in the COMET Phase-I experiment is 16k events for $k_{\text{max}} = 90$ MeV and a running time of 100 days.

Table 8.1: Parameter to estimate number of Al RMC γ in the COMET Phase-I experiment

Parameters	Value	Comment
Y_μ	$1.2 \times 10^9\ s^{-1}$	Muon yield stop for COMET Phase-I experiment goal [18]
f_{cap}	61%	Muon stoped capture ratio in ^{27}Al [62]
A_{conv}	0.075-0.085%	Photon conversion ratio in the innerwall for $E_\gamma = [60 - 101.85]$ MeV see section 4.2.2
R_{time}	100 days	Measurement running time
A_{geom}	2-20%	Geometrical acceptance for $E_\gamma = [60 - 101.85]$ MeV see section 4.2.3
A_{MTW}	30%	Measurement time window acceptance see section 4.2.4
A_{online}	90%	Online trigger scheme acceptance see chapter 5
$\epsilon_{\text{analysis}}$	2-19%	Analysis algorithm efficiency minimum for 60 MeV photon and maximum for 95 MeV photons see section 7.3.3
R_γ	1.40×10^{-5}	TRIUMF Experiment measured partial branching ratio [43]
k_{max}	90 MeV	TRIUMF Experiment measured k_{max} [43]
Total	16k events	

Chapter 9

Estimation of $k_{\mathbf{max}}$ and R_γ

To calculate the effect of RMC on the measurement of $\mu^- \to e^+$ conversion positron measurement, the partial branching ratio (R_γ), where $E_\gamma > 57$ MeV, and the energy spectrum endpoint (k_{max}) must be evaluated. A likelihood fit on Monte-Carlo simulated data is performed to evaluate both of them.

9.1 Partial branching ratio R_γ

The RMC partial branching ratio R_γ for E_γ larger than 57 MeV is given by:

$$R_\gamma = \frac{N_{\gamma>57\ MeV}}{N_{\text{MC}} \times A_{\text{conv}} \times A_{\text{geom}} \times A_{\text{online}} \times A_{\text{MTW}} \times \epsilon_{\text{analysis}}}, \tag{9.1}$$

where $N_{\gamma>57\ MeV}$ is the number of observed RMC events with E_γ larger than 57 MeV, N_{MC} is the number of observed muon captured in the muon target. ϵ and A represents the various efficiencies/acceptances:

- A_{conv} is the conversion rate of photon in the innerwall of the CDC;
- A_{geom} is the geometry acceptance — CTH 4-fold trigger acceptance, and at least both electron and positron reach the 5th layer;
- A_{online} is the online trigger acceptance — 90%;
- A_{MTW} is the measurement time window acceptance — 30%; and
- $\epsilon_{\text{analysis}}$ is the analysis code efficiency.

These efficiencies and acceptance rates have been calculated in the previous chapters and have been resumed in Chapter 8. Using this information, the sensitivity of RMC measurement in the COMET Phase-I can be estimated.

9.2 RMC energy spectrum endpoint $k_{\mathbf{max}}$

The RMC photon energy spectrum can be successfully described within the Primakoff closure approximation model:

$$\frac{dN}{dE} = \frac{e^2}{\pi}\frac{k_{\text{max}}^2}{m_\mu^2}(1 - \frac{N-Z}{A})(1 - x + 2x^2)x(1-x)^2, \tag{9.2}$$

where E is the photon energy, $k_{\max}$ is the energy spectrum endpoint, $(N - Z)/A$ is the neutron excess in the nucleus, and x is given by $E/k_{\max}$ see chapter 1. The aluminum spectrum with $k_{\max} = 90$ MeV is shown in Figure 9.1.

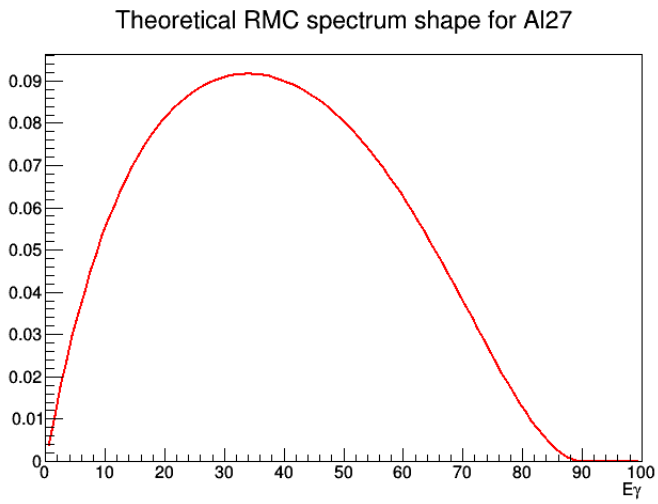

Figure 9.1: Theoretical RMC spectrum shape for ^{27}Al with $k_{\max} = 90$ MeV.

9.3 Log maximum likelihood estimation

The shape of the spectrum depends on $k_{\max}$ as shown in Eq. 9.2. However, the amplitude of the spectrum is dependant of N_γ. Thus, Eq. 9.2 is fitted with 2 parameters, $k_{\max}$ and N_γ. Here, N_γ acts as a free normalization factor.

The fitting is performed using the likelihood:

$$L(k_{\max}, N_{\gamma>57}) = \prod_i F(x_i; k_{\max}, N_{\gamma>57}); \tag{9.3}$$

where x_i is the number of RMC gamma measured in the i-th bin of the E_γ spectrum, and $F(x_i; k_{\max}, N_{\gamma>57})$ is the probability of observing x_i events with $k_{\max}$ and $N_{\gamma>57}$. The probability of observing x entries while the predicted average is m is given by the Poisson distribution:

$$f(x; m) = \frac{m^x e^{-m}}{x!}. \tag{9.4}$$

For RMC it is given by:

$$F(N_{\text{expected }i}, N_{measured\ i}) = \frac{N_{\text{expected }i}^{N_{\text{measured }i}} e^{-N_{\text{expected }i}}}{N_{\text{measured }i}!}, \tag{9.5}$$

where $N_{\text{expected }i}$ is the number of events expected in the i-th bin, and $N_{\text{measured }i}$ is the number of events measured in the same bin i.

For the analysis, instead of the likelihood function the log likelihood function is used:

$$\ln(L(k_{\max}, N_{\gamma>57})) = \sum_i \ln(F(x_i; k_{\max}, N_{\gamma>57})). \tag{9.6}$$

The most likely parameter for $k_{\max}$ and $N_{\gamma>57}$ are given when $\ln(L(k_{\max}, N_{\gamma>57}))$ is maximum. The confidence interval at 63% for the log likelihood is given by:

$$\ln(L(k_{\max}, N_{\gamma>57})) = \ln(L_{\max}) - \frac{1}{2}. \tag{9.7}$$

To quantify the quality of the fit, one can use λ defined as:

$$\lambda = \frac{L(k_{\max} N_{\gamma>57})}{L_0} \tag{9.8}$$

where L_0 corresponds to the saturated model, i.e, the likelihood of observing x events per bin, while the predicted average is x. Wilks' theorem [63] states that $-2\ln(\lambda)$ approaches the χ^2 distribution asymptotically. As a result, it can be used to assess the goodness of the fit.

9.4 Fitting function

To see the precision of the $k_{\max}$ and R_γ, the expected RMC spectrum has been calculated. The spectrum was calculated by combining the RMC theoretical spectrum shown in Figure 9.1 and the total measurement efficiency shown in Figure 8.1, which includes the inner wall conversion rate, the geometrical acceptance, and the analysis efficiency. The expected RMC spectrum is shown in Figure 9.2.

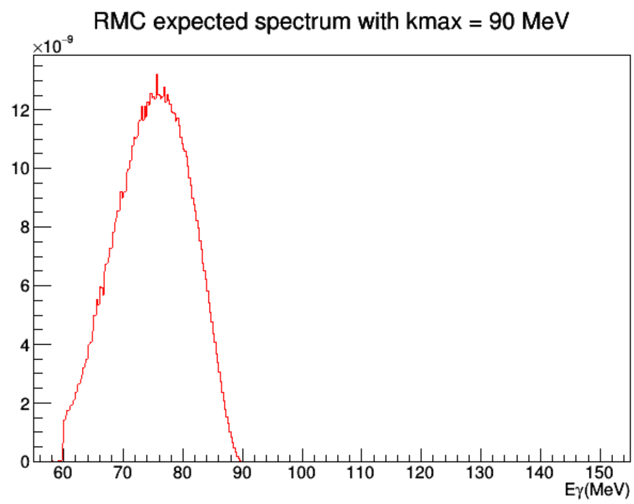

Figure 9.2: Al RMC predicted photon spectrum in the COMET Phase-I experiment by the Primakoff model with $k_{\max} = 90$ MeV

To reproduce the expected E_γ reconstructed spectrum by the COMET Phase-I experiment, the resolution of the analysis needs to be taken into account (Figure 7.18). The E_γ reconstructed spectrum is shown in Figure 9.3. Here, the resolution has been assumed to be the same for different E_γ. The systematics uncertainty coming from this assumption is discussed in chapter 10.

To calculate the statistical precision of $k_{\max}$ and R_γ for the number of RMC events N_{RMC}, one can generate N_{RMC} event using the spectrum shown in Figure 9.3. The generated spectrum for N_{RMC} expected in 100 days with a partial branching $R_\gamma = 1.40 \times 10^{-5}$ and a $k_{\max} = 90$ MeV is given in Figure 9.4.

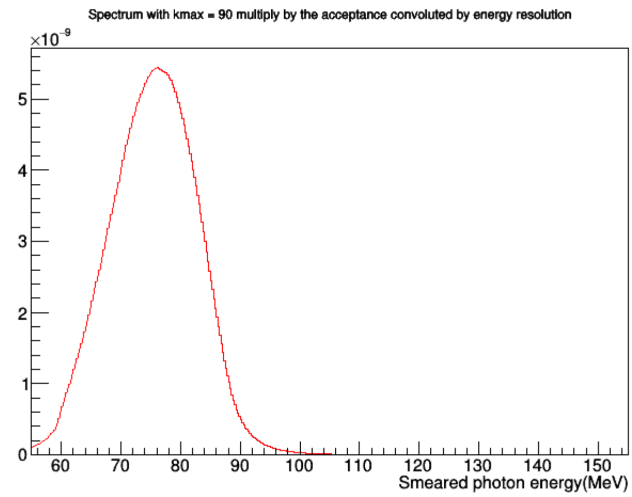

Figure 9.3: Spectrum expected to be reconstructed by the COMET Phase-I experiment assuming $k_{\mathrm{max}} = 90$ MeV

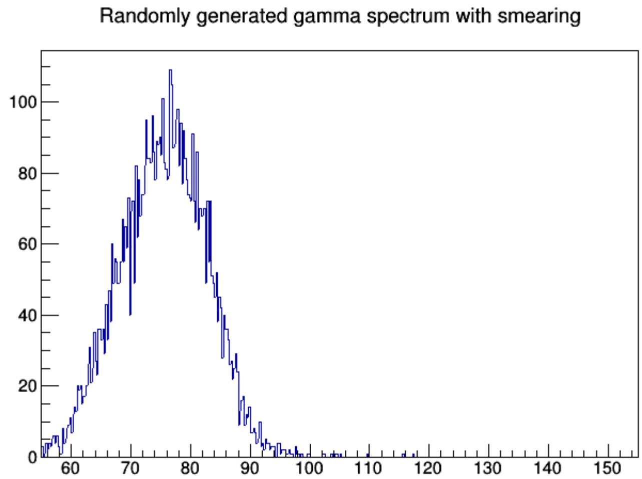

Figure 9.4: Spectrum generated with $N_{\mathrm{RMC}} = 16\ k$ coresponding to 100 days running. $R_\gamma = 1.40 \times 10^{-5}$ and $k_{\mathrm{max}} = 90$ MeV

As an example, the $\ln \lambda$ of the fitting of the spectrum shown in Figure 9.4 by the spectrum shown in Figure 9.3 is shown in Figure 9.5. The 63% confidence interval is shown by the black line. 200 bins were used for the fitting; which gives a reduced χ^2 of 1.01 indicating a good fit, which is expected because the fitted spectrum was directly generated using the fitting function.

9.5 Results

The analysis was performed to determine the statistical precision of this analysis for k_{max} and R_γ. As a result, the starting parameters were varied, and both k_{max} and R_γ statistical precision were assessed. All confidence intervals were calculated at a 90% level.

Table 9.1 shows the statistical error to k_{max} for different given values of k_{max} and R_γ. At a fixed R_γ, increasing k_{max} increases the number of expected events, and

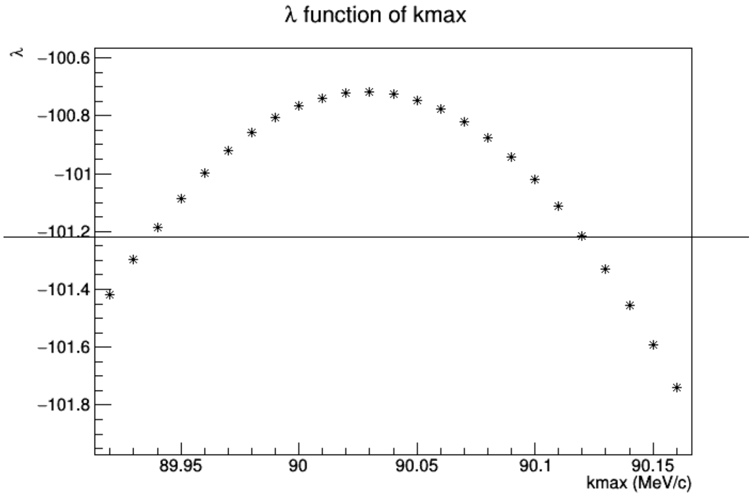

Figure 9.5: Log λ function of $k_{\max}$. The intersection between the black line and the $\ln \lambda$ function shows the 63% confidence interval. $k_{\max} = 90MeV$, 200 bins were used to calculate the $\ln \lambda$ function

thus the statistical precision improves. This is due to the geometrical acceptance and analysis efficiency being dependent on the E_γ combined with the RMC spectrum. At a fixed $k_{\max}$, increasing the R_γ improves the statistical precision slightly. In both cases, the statistical precision variation on $k_{\max}$ is negligible.

Table 9.1: Table showing obtained $k_{\max}$ with statistics error obtained for different partial branching ratio and different truth $k_{\max}$.

R_γ (10^{-5}) $k_{\max}(MeV)$	1.20	1.30	1.40
85	85.07 ± 0.20	85.1 ± 0.19	85.11 ± 0.19
90	90.04 ± 0.18	90.03 ± 0.18	90.05 ± 0.17
95	95.02 ± 0.18	95.03 ± 0.17	94.99 ± 0.17
100	99.95 ± 0.18	99.97 ± 0.17	99.98 ± 0.17

The statistical errors to R_γ for different initial value of $k_{\max}$ and R_γ are shown in Table 9.2. Contrary to $k_{\max}$, the statistical precision of R_γ is greatly affected by the change in the number of expected events for different parameters. For example, at a fixed R_γ, the precision doubles from $k_{\max} = 85$ MeV to $k_{\max} = 100$ MeV.

According to the TRIUMF experiment results for ^{27}Al [43], i.e. $k_{\max} = 90.1$ MeV and $R_\gamma = 1.40 \times 10^{-5}$, the COMET Phase-I experiment should be able to measure $k_{\max}$ at $\pm 0.17(stat)$ MeV and R_γ at $\pm 0.019 \times 10^{-5}(stat)$ from table 9.1, and table 9.2.

Table 9.2: Table showing obtained R_γ measured with statistics error obtained for different partial branching ratio and different truth $k_{\max}$.

R_γ (10^{-5}) $k_{\max}(MeV)$	1.20	1.30	1.40
85	1.20 ± 0.026	1.30 ± 0.024	1.40 ± 0.025
90	1.20 ± 0.018	1.30 ± 0.019	1.40 ± 0.019
95	1.20 ± 0.015	1.30 ± 0.015	1.40 ± 0.015
100	1.20 ± 0.012	1.30 ± 0.012	1.40 ± 0.012

Chapter 10

Uncertainty estimation

There are multiple sources of uncertainty in the measurement of k_{max} and R_γ. In addition to the statistical error, these other sources of error need to be understood. Depending on their dangerousness, countermeasures need to be used. This chapter calculates the background contribution of other processes to the measurement of RMC in ^{27}Al, and the systematic error in the measurement. In addition, examples of two calibration schemes are discussed.

10.1 Background contamination to RMC γ measurement

There are other physical processes that can produce photons, which can deform the measured RMC spectrum. To understand their impact on the RMC γ measurement, one can calculate the number of expected events from these background processes.

The main background sources possible for RMC are divided into two categories:

- beam-related background, and

- intrinsic physic background.

A list of potential background contamination is listed in table 10.1.

Table 10.1: A list of potential background for the measurement of ^{27}Al at the COMET Phase-I experiment

Beam related delayed backgrounds	
1. Beam neutrons	$\pi^0 \to 2\gamma$
2. Radiative pion capture	$\pi^- + N(A,Z) \to \gamma + N(A, Z-1)$
Intrinsic physics backgrounds	
3. Coincidental DIO electrons	Coincidental electrons
4. RMC in helium	Radiative muon capture in He

10.1.1 Beam related background

Beam neutrons π^0 decay

Energetic neutrons in the beam can create π^0 that can decay by producing two γs:

$$\pi^0 \rightarrow 2\gamma. \tag{10.1}$$

According to the simulation [18], neutrons arrive in the target region around 200 ns. The background is really suppressed around the measurement window region, which starts at 700 ns. The life time of a pion is 9.5×10^{-17} s. As a result, the prompt π^0 decay can be neglected. However, protons from the beam can leak and be emitted between bunches. This number may not be negligible and is calculated by:

$$N_{\pi^0} = N_{\text{proton}} \times R_{\text{extinction}} \times R_{n/p} \times R_{\pi^0/n} \times A_{\text{geo}} \times \epsilon_{\text{analysis}}, \tag{10.2}$$

where N_{π^0} is the number of π^0 expected, N_{proton} is the total number of protons on the pion production target, $R_{\text{extinction}}$ is the proton beam extinction factor introduced in chapter 2, $R_{n/p}$ is the number of neutrons per proton, $R_{\pi^0/n}$ is the number of π^0 per neutron, A_{geo} is the geometrical acceptance (photon conversion in inner wall, 5 layer reached by both electron and positron and CTH 4-fold coincidence), and $\epsilon_{\text{analysis}}$ is the analysis acceptance.

As a precaution, the maximum values of A_{geo} and $\epsilon_{\text{analysis}}$ are used, 7.9×10^{-5} and 19% respectively.

The value of each parameter is shown in Table 10.2. The parameters give $N_{\pi^0} < 4.4 \times 10^{-7}$ events for 148 days of running. This is sufficiently small to be neglected.

Table 10.2: Parameters list used to estimate the background rate due to π^0 double gamma decay.

Parameters	Value	Source
N_{proton}	3×10^{19}	COMET Phase-I experiment goal [18]
$R_{\text{extinction}}$	3×10^{-11}	Simulation[18]
$R_{n/p}$	10^{-5}	Simulation[18]
$R_{\pi^0/n}$	1.6×10^{-6}	Simulation[18]
A_{geo}	7.9×10^{-5}	Acceptance for 101 MeV sec. 4.2.3
$\epsilon_{\text{analysis}}$	19%	Efficiency for 95 MeV sec. 7.3.3

Radiative pion capture

RPC reaction is:

$$\pi^- + N(A, Z) \rightarrow \gamma + N(A, Z-1). \tag{10.3}$$

where the γ can have an energy distributed around 120 MeV as shown in Figure 10.1.

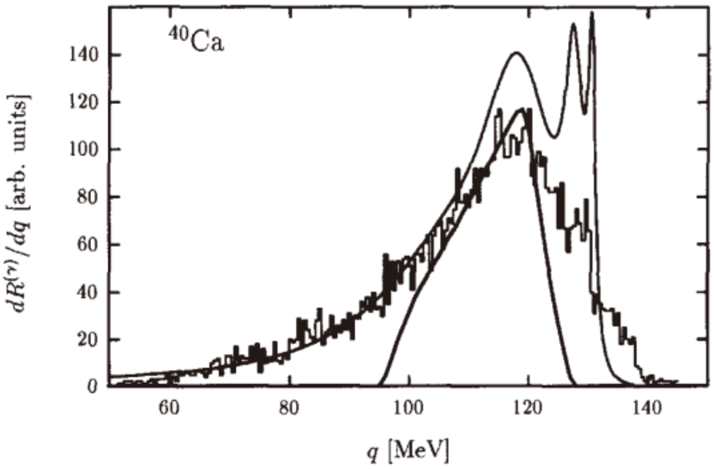

Figure 10.1: Measured momentum distribution of RPC-induced γs in ^{40}Ca [64] (histogram), with two theoretical model (smooth lines)

The same as for π^0 decay, the number of π^- from the prompt beam in the delayed measurement time window is extremely suppressed. According to the simulation [18], the number of π^- in the trigger window per proton is lower than 10^{-20} and thus can be neglected. However, π^- can be produced by delayed protons. The number of RPC events is given by [18]:

$$N_{RPC} = N_{\text{proton}} \times R_{\text{extinction}} \times R_{\pi-stop/p} \times B_{RPC} \times A_{\text{geo}} \times \epsilon_{\text{analysis}}, \tag{10.4}$$

where $R_{\pi-stop/p}$ is the number of π^- arring at the muon stopping target per proton, B_{RPC} is the branching ratio of radiative pion capture, A_{geo} is the geometrical acceptance (photon conversion in inner wall, 5 layer reached by both electron and positron and CTH 4-fold coincidence), and $\epsilon_{\text{analysis}}$ is the analysis acceptance.

The only unknown parameters for 120 MeV γ are the $\epsilon_{\text{analysis}}$ and the A_{geo}. However, as shown in chapter 7, the product of $\epsilon_{\text{analysis}}$ and A_{geo} is maximal around 95 MeV and decreases later. As a precaution, $\epsilon_{\text{analysis}}$ will be taken at its maximum, i.e., 19%, and A_{geo} is extrapolated by a 1st-degree polynomial to 120 MeV.

The value of parameter is shown in Table 10.3. The parameters give $N_{RPC} < 2.0 \times 10^{-3}$ events for 148 days of running, which is sufficiently small to be neglected.

Table 10.3: Parameters list used to estimate the background rate due to RPC.

Parameters	Value	Source
N_{proton}	3×10^{19}	COMET Phase-I experiment goal [18]
$R_{\pi-stop/p}$	3.4×10^{-6}	Simulation [18]
$R_{\text{extinction}}$	3×10^{-11}	Simulation [18]
B_{RPC}	$2.27\% \pm 0.48$	Branching ratio for ^{16}O[64]
A_{geo}	1.5×10^{-4}	Acceptance for 120 MeV extrapolated from sec. 4.2.3
$\epsilon_{\text{analysis}}$	19%	Efficiency for 95 MeV sec. 7.3.3

10.1.2 Intrinsic physic background

Accidental coincidence of decay in orbit electrons

The main decay channel of the muon stopped in the target is decay in orbit:

$$\mu^- + N \rightarrow e^- + \bar{\nu}_e + \nu_\mu + N. \tag{10.5}$$

As the majority of the stopped muons decay in orbit, a large number of electrons will be produced in the detector region. Thus, it is possible that two DIO electrons reach the detector at the same time. Figure 10.2 shows a sketch of a possible coincidental DIO event.

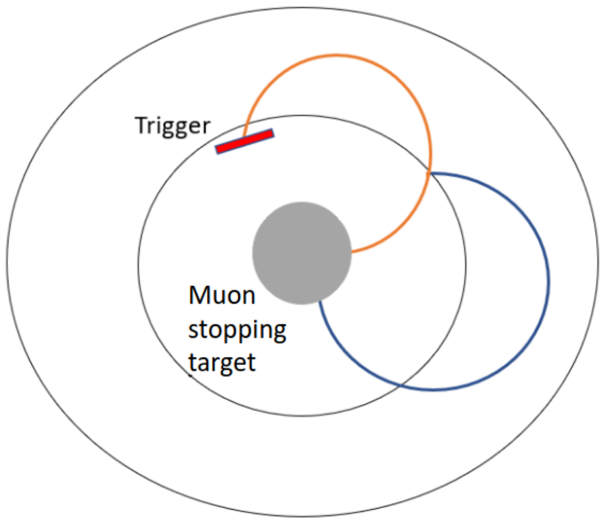

Figure 10.2: Sketch of coincidental DIO event

However, contrary to the electron and positron from our study, DIO electrons come from the muon stopping target. Thus, only high-energy electrons can reach the detector because of the 1 T magnetic field. From the simulation [18], the frequency of DIO event reaching the detector 5th layer is 1.8 Hz ($R_{5\text{th}}$), and the ratio of DIO electron passing the trigger condition and the 5th layer is 0.6 Hz (R_{CTH4}). The window frame used is 400 ns (dt). The number of events expected per second containing two DIO electron tracks ($R_{2\text{DIO}}$) is given by:

$$R_{2\text{DIO}} = R_{5\text{th}} \times R_{\text{CTH4}} \times dt. \tag{10.6}$$

This results in a rate of 4.32×10^{-7} events per second. For these two tracks to resemble a signal, they must be close together. Assuming that the track should be close near the CDC inner wall (2-3 cells), this decreases the rate to 4.32×10^{-9} events per second, which give in 148 days running time 0.0552 events expected. The background due to coincidental DIO is negligible in comparison to the expected number of RMC events($\approx$ 16k for 100 days).

Radiative muon capture

The muon-stopping target region is filled with helium at a pressure of 1 atmosphere. As a result, muons can be stopped in helium and undergo RMC, which can be problematic for the ^{27}Al RMC γ measurement. According to the simulation [65], the number of muons stopped in helium is a sixth of the number of muons stopped in the aluminum target. The gas consists primarily of two isotopes, ^{3}He and ^{4}He, with natural abundances of 0.0002% and 99.9998%, respectively [66]. Only RMC events from ^{4}He will be considered, as ^{3}He RMC events are well suppressed by ^{3}He natural rarity.

Similarly to the study for ^{27}Al RMC, the number of ^{4}He RMC events can be calculated using the Primakoff closure approximation model and the Monte-Carlo simulation. However, because ^{4}He RMC has not been measured, R_γ and k_{max} are both unknown. To estimate the energy range of the background, instead of using k_{max}, the maximum allowed kinetic energy is used. The maximum allowed γ energy for ^{4}He is $E_{\mathrm{RMC}}^{\mathrm{end}} = 81.2$ MeV. When it comes to R_γ, the highest measured value is used as an approximation.

The capture ratio is also different in ^{4}He. Measurement reported by Suzuki *et al.* [62] reported the capture ratio for ^{4}He to be 0.074%, lower than that of ^{27}Al by a factor of 827.

The acceptance of the measurement time window must be calculated for the helium muonic atom. The mean life-time of muonic helium is not known. However, a clear dependence of the mean life time of the muonic atom on its Z has been shown [62]. The life time is estimated to be between 2197 ns and 2173 ns, which are the lifetimes of the hydrogen and lithium muonic atoms, respectively [62]. The trigger time distributions for using H muonic atom and Li muonic atom are shown in Figure 10.3. Both acceptance rates are comparable and yield an acceptance rate of 36%.

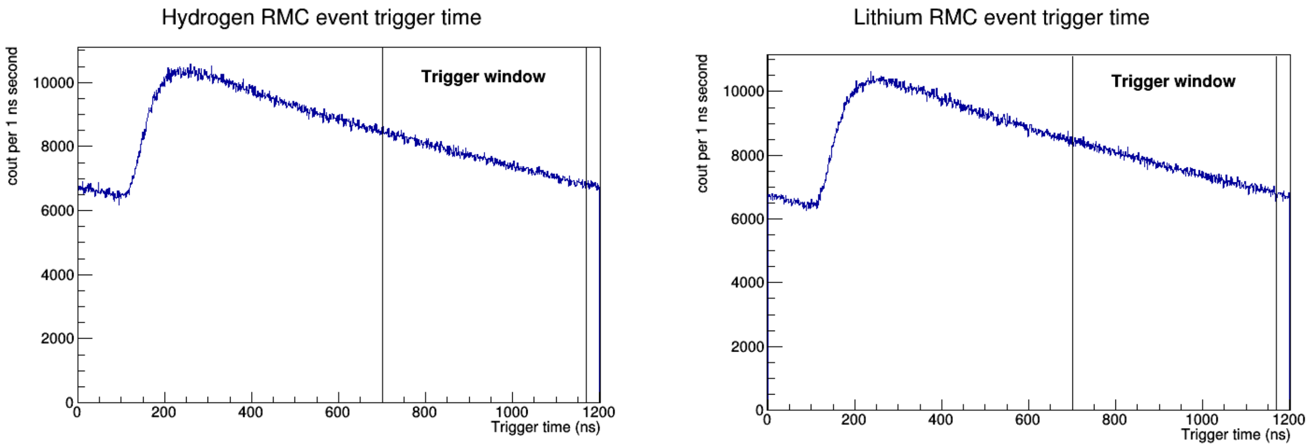

(a) (b)

Figure 10.3: Measurement time window of RMC event by replacing the aluminum target with (a) hydrogen and (b) lithium target.

The different parameters used to evaluate the number of expected ^{4}He RMC γ in the COMET Phase-I experiment are shown in Table 10.4. It yields a total number of events of 2.5 events in 100 days, which is negligible compared with the number of expected RMC events in aluminum.

Table 10.4: Parameter to estimate number of He RMC γ in the COMET Phase-I experiment

Parameters	Value	Comment
Y_μ	$2.0 \times 10^8\ s^{-1}$	Muon yield stop for COMET Phase-I experiment in He [65]
f_{cap}	0.074%	Muon stoped capture ratio in ^{4}He [62]
A_{conv}	0.075-0.085%	Photon conversion ratio in the innerwall for $E_\gamma = [60 - 101.85]$ MeV see section 4.2.2
R_{time}	100 days	Measurement running time
A_{geom}	2-20%	Geometrical acceptance for $E_\gamma = [60 - 101.85]$ MeV see section 4.2.3
A_{MTW}	35%	Measurement time window acceptance for ^{4}He
A_{online}	90%	Online trigger scheme acceptance see chapter 5
$\epsilon_{\text{analysis}}$	2-19%	Analysis algorithm efficiency minimum for 60 MeV photon and maximum for 95 MeV photons see section 7.3.3
R_γ	2.0×10^{-5}	Partial branching ratio for no neutron excess [67]
k_{max}	81.2 MeV	Maximum kinetically allowed energy for RMC γ in ^{4}He
Total	2.5 events	

Table 10.5: Summary of the estimated background events for ^{27}Al RMC measurement

Type	Background	Estimated events
Delayed beam	π^0 decay	4.4×10^{-7}
	Radiative pion capture	2.0×10^{-3}
Physics	Accidental muon decay in orbit	0.0552
	^{4}He radiative muon capture	2.5
Total		≤ 2.6

10.1.3 Summary of Background Estimations

Table 10.5 shows a summary of the estimation of the background event to the measure of ^{27}Al radiative muon capture γ. The number of expected background events is lower than 2.6, which is negligible compared with the expected 16k events from ^{27}Al RMC.

10.2 Systematic error

To understand the limit of the measurement, the systematic errors need to be estimated.

10.2.1 Partial branching ratio error

The number of RMC event expected is:

$$N_{\mathrm{RMC}} = N_{\mathrm{stopped}} \times R_{\gamma} \times R_{\gamma \to e^+e^-} \times A_{\mathrm{geom}} \times \\ A_{\mathrm{time}} \times \epsilon_{\mathrm{online}} \times \epsilon_{\mathrm{analysis}} \tag{10.7}$$

where N_{stopped} is the number of stopped muons, $R_{\gamma \to e^+e^-}$ is the ratio of photons that are converted into an electron-positron pairs inside of the detector inner wall.

N_{stopped} — number of stopped muon

Once the muon is stopped, an excited muon atom is formed. This muonic atom quickly transitions to the ground state by emitting X-rays. To measure the number of stopped muons, the COMET Phase-I experiment will measure the X-ray spectrum using a germanium detector.

The AlCap experiment is using a similar germanium detector, which reported $(160 \pm 5) \times 10^6$ muons stopped events in their measureemnt. This corresponds to a statistical error of 3.1% [68]. The uncertainty will thus be assumed to be constrained within 3.1%.

$R_{\gamma \to e^+e^-}$ - Inner wall effect, first layer conversion

Two uncertainties can be directly linked to the photon conversion rate:

- the inner wall thickness, and
- the pair creation in the guard layer or in the first layer of the CDC.

The manufacturing error on the thickness of the inner wall is known to be in the order of 0.02 mm for an inner wall with a thickness of 0.55 mm. This gives an uncertainty of 3.6% in the total number of converted photons in the inner wall.

Regarding the conversion in the first two layers of the CDC. The main contribution is due to the photon conversion in the wires. There are two kinds of wires: sense wires and field wires. They are both made of different materials: one is gold-plated tungsten (diameter of 25 μm) and the other is aluminum (diameter of 126 μm). The effect of the conversion in wires can be approximated by assuming an additional layers of material with an equivalent spacial thickness that corresponds to the average volume of the wire material. The resulting inner wall layer thickness is 70 nm for the sense wire and 2 μm for the field wire. While the tungsten layer may seem quite small, the pair creation branching ratio is a function of Z^2. Thus, for the same spacial thickness, photon conversion occurs 32 times more in tungsten than in aluminum. Taking this effect into account, an additional error of 0.77% on the total number of converted photons in the inner wall must be considered.

A_{geom}

The geometrical acceptance is taking into account the CTH 4-fold trigger rate. The trigger rate will be normalized using the DIO calibration. The knowledge of stopped muons, however, limits the precision of the DIO trigger rate. Or this is limited by an error of 3.1%, as explained in section 10.2.1. Both uncertainties will be estimated at 3.1% and assumed to be 100% correlated.

$A_{\mathbf{time}}$

The life time of aluminum muonic atom being relatively well-known [62] at a precision of 0.2%, the impact on the measure of RMC is negligeable. Thus, the error on the window acceptance is given by the CTH time resolution. The CTH time resolution is 1 ns. Thus, the error is given by shifting the trigger window by 1 ns.

Using the distribution of the trigger time shown in Figure 4.8, the error due to the shifting of the trigger window by 1 ns can be calculated to be 0.26%.

$\epsilon_{\mathbf{online}} \times \epsilon_{\mathbf{analysis}}$ - Background occupancy

The main cause of performance changes in the online trigger and analysis efficiency is the background occupancy. Both of them heavily rely of the detector background occupancy. With an increase in background occupancy, the probability of a signal hit being shadowed greatly increases.

A 45% background occupancy has been assumed in this study based on the simulation; see chapter 4. However, the simulation hints at a background occupancy variation of 2.3%. To look at this effect, the analysis has been made again on the signal event, but with a background occupancy of 50% instead of a background occupancy of 45%. In the case of a background occupancy of 50%, 1.3 M events are successfully fitted out of the 10 M events that passed the analysis code requirement, compared to 1.5 M for a background occupancy of 45%. Thus, the difference is in the order of 8.6% for an increase in the background by 5%.

One reason for this efficiency change is that the GBDT was not re-trained for a background occupancy of 50%. The denoising performed using a GBDT should be trained at different levels of background occupancy. Increasing the background occupancy changes the distribution of the neighboring features and may confuse the GBDT algorithm. Thus, one can train multiple GBDT algorithms at different occupancy levels and use the appropriate GBDT training results depending on the occupancy of this event.

However, increasing the background not only increases the number of background hits but also decreases the number of signal hits. Having a higher number of background hits means that the number of signals hits that are shadowed and thus lost increases. Figure 10.4 shows the effect of the shadowing effect on the electron and positron hits at a background occupancy of 45%. The average number of events hit per electron and positron goes from 25 to 17 hits (16 hits for 50% background occupancy).

To reduce this effect, there are only two possible ways:

- shifting the measurement time window, and
- reducing the beam power.

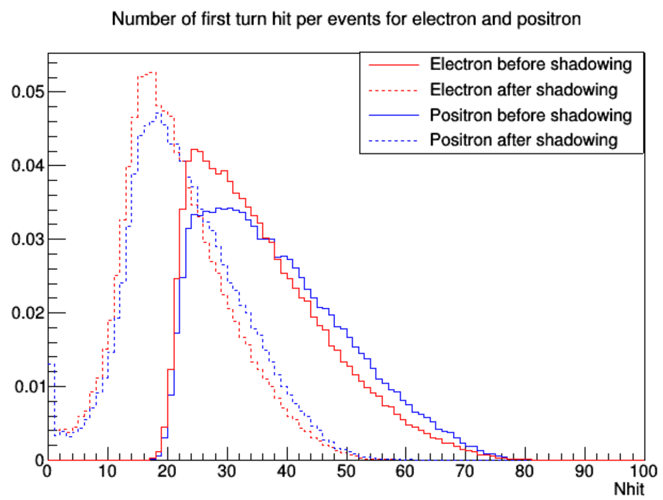

Figure 10.4: Number of first turn hit per events for electron and positron before and after shadowing effect with 45% background occupancy.

Both of these solutions will reduce the number of events observed, but on the other hand, the background occupancy should be lower, which will lessen the shadowing effect and increase the efficiency of the analysis code.

10.2.2 Result of R_γ systematic error

Table 10.6 shows the systematic uncertainties for the different parameters. For independent parameters, the square of the error can be added; however, for correlated parameters, the errors must be linearly added.

Table 10.6: List of systematic uncertainty on the measurement of $R_\gamma/N_{\mathrm{RMC}}$.

Parameter	Error	Comment
N_{stopped}	3.1% ‡	Based on AlCap preliminary results [68]
$R_{\gamma\ \to e^+e^-}$	4.4%	Due to inner wall thickness, and detector density
A_{geom}	3.1% ‡	Based on calibration from DIO electron
A_{time}	0.26%	Based on CTH time resolution
$\epsilon_{\mathrm{online}} \times \epsilon_{\mathrm{analysis}}$	4.3%	Due to background occupancy fluctuation
Total	8.7%	

‡ 100% correlated

The systematic uncertainty of R_γ is 8.7%. For a partial branching ratio of 1.40×10^{-5}, it corresponds to a systematic error of 1.22×10^{-6}. The precision of this study to R_γ is lower than the precision of the TRIUMF experiment. There are two ways to improve the systematic error on R_γ: first, when the efficiency of the procedure is estimated at 50% background occupancy, the procedure can be trained with 50% occupancy, which should improve the stability of the procedure. Second, another method for calibrating the detector geometry independent of any muon capture processes should be developed.

10.2.3 Spectrum endpoint (k_{max}) systematic error

As demonstrated in chapter 9, small statistical variations have negligeable effects on the k_{max} statistical error. Thus, even if N_{RMC} changes by 10%, k_{max} is almost unaffected. On the other hand, k_{max} is sensitive to parameters that can change the shape of the measured spectrum, such as the fitting residue, the spectrometer calibration, and so on.

Spectrometer calibration

To achieve its goal of measuring $\mu^- \to e^-$ conversion at a SES of 3.1×10^{-15}, the COMET Phase-I experiment must achieve a momentum resolution of 200 keV for 105 MeV electron [18]. This calibration depends on the magnetic field calibration (which can be monitored) and the drift time of the ionized electron toward the sense wire. The second is critical for the success of the COMET Phase-I experiment and has been evaluated on the prototype test [69], it has also been evaluated using cosmic ray muons, and once again will be calibrated using muon DIO electrons. The systematic uncertainty due to the spectrometer calibration is taken as 200 keV.

Analysis acceptance curve function of background level

The change in the background occupancy modifies the shape of the accepted events at the end of the algorithm. Figure 10.5 shows the distribution of the expected ^{27}Al RMC spectrum with 45% occupancy and with 50% occupancy.

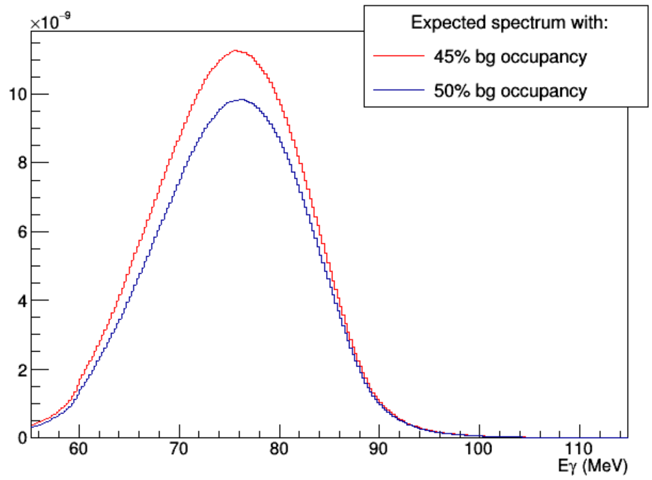

Figure 10.5: Expected shape of the RMC spectrum with analysis efficiency for 45% background occupancy and for 50% background occupancy

The same way as in chapter 9, a fitting is done. However, the fitting is done by generating events according to the 50% background occupancy expected spectrum and has been fitted assuming the 45% background occupancy expected spectrum. The log λ of the fitting is shown in Figure 10.6. This shifts the real value of k_{max} by 350 keV. A systematic error of 350 keV is thus considered to take into account the possible change in the background level.

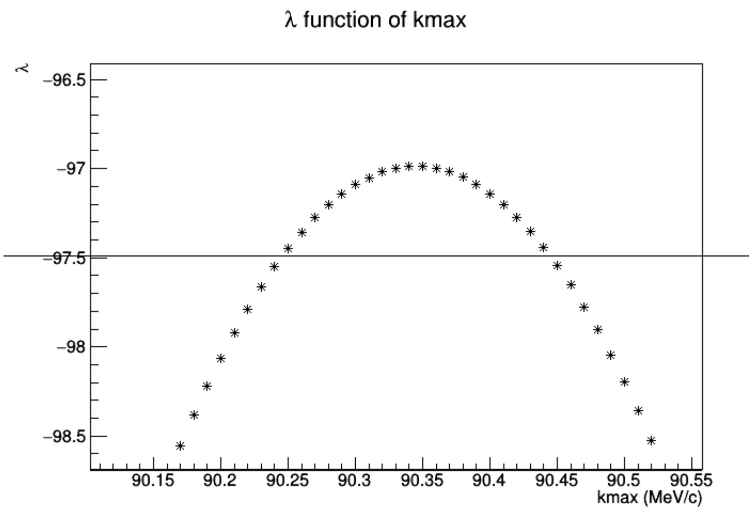

Figure 10.6: Fitting of RMC expected event with 50% occupancy with the 45% expected occupancy

Residue function dependence to E_γ

The residue shape was assumed to be independent of E_γ in chapter 9. However, this is not true. The residue shape for various E_γ is shown in Figure 10.7. A clear dependence on E_γ is demonstrated for the tail, while the main body is consistent for different energy; for the lower energy E_γ, the high-energy tail is larger but the low-energy tail is constrained. The trend is reversed at higher energies E_γ; the low-energy tail is larger while the high-energy tail is more constrained. This difference can be explained by fiducial cuts made on low- and high-fitted electron and positron momentum.

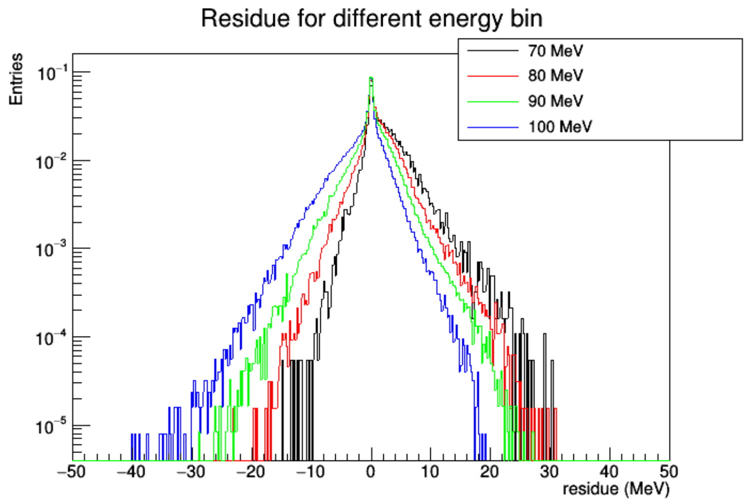

Figure 10.7: Residue function for different E_γ

The expected ^{27}Al RMC spectrum for residue without E_γ dependence, sampled every 20 MeV and sampled every 10 MeV is shown in Figure 10.8. The effect on the final expected shape is non-negligible. However, at a higher sampling of the residue, the error difference is minimal.

Thus, for the experiment, the fitting should be performed using the appropriate

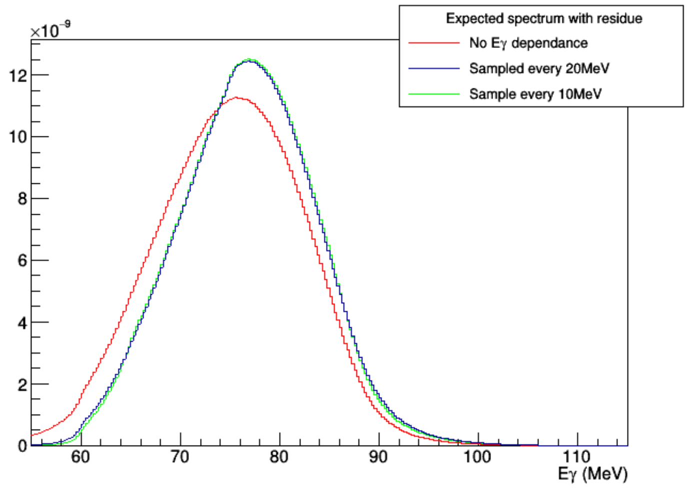

Figure 10.8: Expected ^{27}Al spectrum by taking into account 3 residue cases: with no E_γ dependence, with residue sampled every 20 MeV and with residue sampled every 10 MeV

residue function. There are two equivalent ways to increase the understanding on the resolution of the experiment:

- using the goodness of fit in the analysis, and
- doing a momentum calibration.

In both of this ways, the goal is to compare the simulation results with the experiment results. In the simulation, one can assume several resolutions and compare it with the measured spectrum. Radiative pion capture and neutral pion decay can both be used by the COMET experiment for the calibration, as explained in section 11.2. The TRIUMF experiment found an error of 500 keV to their calibration [41]. The COMET Phase-I experiment can obtain similar statistics in 1 day as shown in section 11.2. Thus, the effect of the residue function would be estimated at 500 keV.

Primakoff model spectrum shape

The Primakoff model is a convenient and general way of describing the RMC photon spectrum. As discussed in Chapter 1, many other models exist to describe precise RMC interactions for specific or heavy nuclei. It is, however, the only model available for describing the Al RMC γ spectrum. Thus, one must assume that this analysis is highly dependent on the model and that model-independent analyses are needed. In addition, $k_{\max}$ is a construction of the Primakoff model, no error is assumed from the Primakoff spectrum shape.

10.2.4 Result of $k_{\max}$ systematic uncertainty

The systematic uncertainties in the measurement of $k_{\max}$ are resumed in Table 10.7. As no correlation is found between the variables, the squares of the errors are summed to obtain the total systematic uncertainty.

Table 10.7: List of systematic uncertainty on the measurement of k_{max}.

Parameter	Error (keV)	Comment
Spectrometer calibration	200	105 MeV electron momentum resolution
O	350	Effect on the change of background occupancy
Residue shape	500	Photon acceptance calibration resolution
Total	650	

The COMET Phase-I experiment will be able to measure k_{max} at (± 0.17 ($stat.$) $\pm$ 0.65 ($syst.$)) MeV, which is an improvement from the TRIUMF experiment by a factor 2.

10.3 Results

It has been shown that the precision of the k_{max} value can be improved by a factor two. However, to achieve this goal, precise knowledge of the experiment is needed, such as the geometrical acceptance, the procedure efficiency, and so on. For that purpose, a precise calibration study is needed.

Chapter 11

Discusion

The primary goal of calculating the RMC spectrum endpoint is to estimate its background contamination in the $\mu^- \to e^+$ conversion experiment. The first section of this chapter focuses on calculating the background contribution of RMC-induced positrons to $\mu^- \to e^+$ conversion measurement within the Primakoff approximation. The second part discusses a few limitations with the current model and how future work is needed to solve them.

11.1 RMC background contamination to $\mu^- \to e^+$ conversion

In this section, the expected e^+ spectrum reconstructed by the COMET Phase-I experiment is calculated. The result of TRIUMF is assumed to be the real value of $k_{\mathrm{max}} = 90.1$ MeV and $R_\gamma = 1.40 \times 10^{-5}$ for the RMC-expected e^+ spectrum. In the experiment, the result may slightly vary, which would change the contamination. To make the spectrum, a few parameters have to be estimated, such as the acceptance of the COMET Phase-I positron event, the fitting residue, and so on.

11.1.1 Reconstruction of the spectrum

Two parameters need to be evaluated to take into account the COMET Phase-I specificity to the positron spectrum. The first is the acceptance of positron events, and the second is resolution reconstruction.

Positron acceptance

The positron acceptance is defined as:

$$A_{e^+} = A_{e^+}(\mathrm{CTH}) \times A_{e^+}(\mathrm{5th\ layer}) \times A_{e^+}(\mathrm{triger\ time\ window}) \times A_{e^+}(\mathrm{online\ trigger}). \tag{11.1}$$

where $A_{e^+}(\mathrm{CTH})$ is the CTH-4 fold trigger acceptance for positron, $A_{e^+}(\mathrm{5th\ layer})$ is the probability that a positron reach the 5th layer, $A_{e^+}(\mathrm{triger\ time\ window})$ is the acceptance of the triger time window, and $A_{e^+}(\mathrm{online\ trigger})$ is the online trigger acceptance.

The value for $A_{e^+}(\mathrm{triger\ time\ window})$ is the same as for RMC and $\mu^- \to e^-$ conversion, i.e. 30%, because they all depend on the muonic life time. Similarly, the A_{online} for RMC and for $\mu^- \to e^-$ conversion is the same with 90% acceptance; thus, similar online trigger for $\mu^- \to e^+$ conversion should give a similar acceptance. Both parameters are independent of the positron's initial momentum.

However, A_{e^+}(5th layer) and A_{e^+}(CTH) are dependant on the initial positron momentum. For the sake of simplification, in this study, they will be considered independent of the positron energy, and the acceptance value for the 92 MeV positron will be used. The simulation of 92 MeV positron [70] has estimated A_{e^+}(5th layer) = 80% and A_{e^+}(CTH) = 19%.

Resolution

The fitting residue will be assumed to be similar to 105 MeV electron signal. Because the positron has a lower energy, the fit may be more susceptible to multiple scattering. However, the tracks are selected using a GBDT, which gives good control over the resolution shape and the efficiency. The resolution is shown in Figure 11.1, to achieve this resolution, only 80% of the fitted track pass the GBDT quality cut requirement. For more information on the GBDT quality track selection algorithm see appendix B.

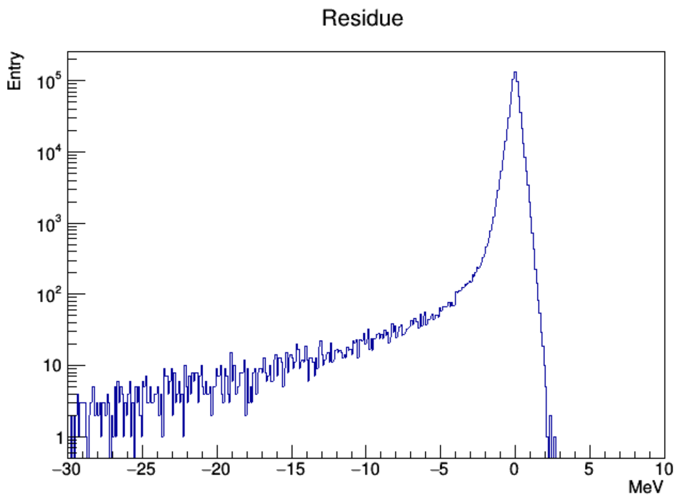

Figure 11.1: Fitting residue for $\mu^- \to e^-$ after GBDT track fitting quality cut B

11.1.2 RMC positron

For a RMC positron to be confused with a $\mu^- \to e^+$ conversion positron, it must originate from the muon stopping target. Thus, pair creation should happen in the muon stopping target. This can happen in two ways:

- by external conversion in the muon-stopping target or
- by internal conversion.

In the simulation, the number of 90 MeV external photons that were converted into the muon stopping target is 0.52%. Although the spectrum and rate of internal conversion are unknown, a similar measure calculating the ratio of photon internal conversion in radiative pion capture has given Br(internal RPC)/Br(RPC) = 0.00694

± 0.00031 [71]. Additionally, the SINDRUM-II experiment [21] only measured the positron spectrum and not the photon spectrum; however, they did not find any contradiction with previous measurements of the RMC spectrum for Au and Ti. This hints at the fact that the number of internal RPCs is highly suppressed. The internal conversion of photons will be considered negligible in this study.

The energy share of electron and positron follow Bethe-Heitler law, the energy share for 90 MeV photons is shown in Figure 11.2.

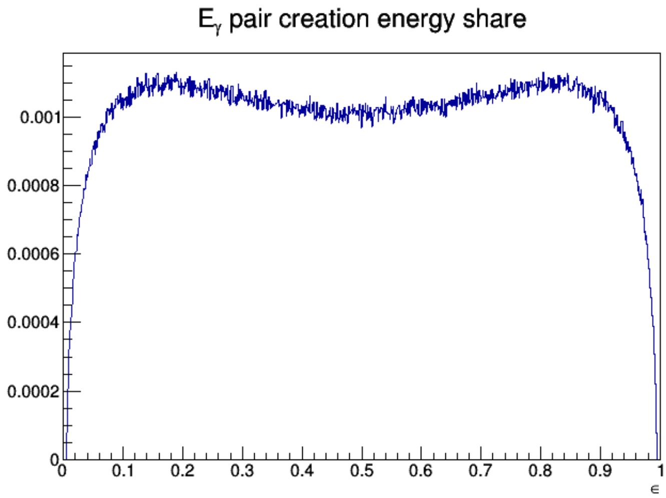

Figure 11.2: Energy share between the electron and the positron $\epsilon = (E_{e^-} + m_e)/E_\gamma$

11.1.3 Ground state and giant dipole resonance

Two transitions are usually used to calculate the spectrum of $\mu^- \to e^+$ conversion, the giant dipole resonance (GDR), and ground state (GS) transitions.

In the GS transition, the positron is emitted mono-energetically at 92.3 MeV for an Al target. In the GDR transition, some energy is taken by the nucleus, which changes the shape of the positron spectrum. In the GDR spectrum, the energy taken in by the nucleus can be represented using a Lorentzian function:

$$L(E) = \frac{1}{2\pi} \frac{\Gamma}{(E - E_0)^2 + (\frac{1}{2}\Gamma)^2}, \tag{11.2}$$

where E is the energy of the nucleus, Γ is the width of the distribution, and E_0 is the mean excitation of the nucleus. Traditionally, both Γ and E_0 are taken equal to 20 MeV when searching for $\mu^- \to e^+$ conversion^{GDR}. However, a previous experiment [72] has shown that for aluminum, the spectrum can be fitted using $E_0 = 21.1$ MeV and $\Gamma = 6.7$ MeV. Thus, as an approximation, the GDR spectrum of Na will be assumed to have a width of 6.7 MeV, and an energy of 21.1 MeV similar to the Al spectrum.

11.1.4 Reconstructed positron spectrum

The reconstructed spectrum is shown in Figure 11.3. The branching ratio for $\mu^- \to e^+$ conversion is assumed to be 100 times lower in the figure than the current upper limit measured by the SINDRUM-II experiment [21].

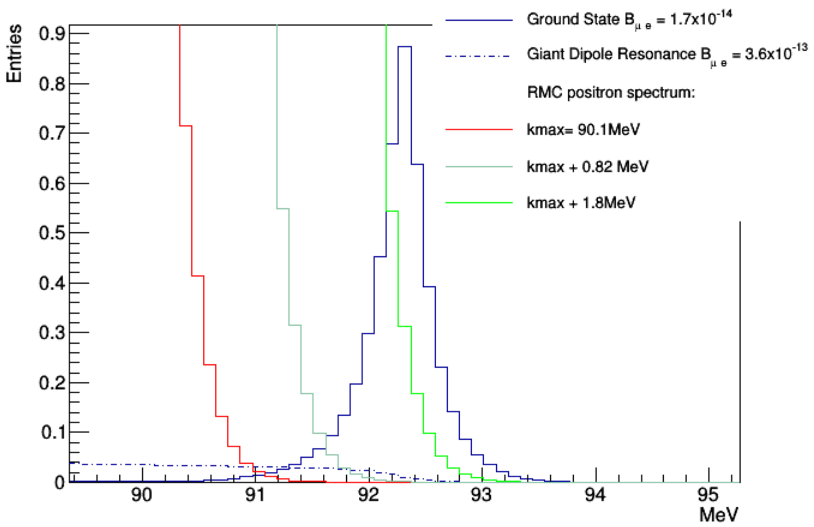

Figure 11.3: Positron spectrum due to RMC with k_{max} at 90.1 MeV, $k_{\text{max}} + 0.82$ MeV see sec. 10.2.3, $k_{\text{max}} + 1.8$ MeV [43], and $\mu^- \to e^+$.

To calculate the background contamination, the energy window of the measurement needs to be determined. The definition of the energy measurement window is not optimized. The end of the window is taken at 95 MeV. The start of the energy measurement window is taken when the number of expected positron events from RMC in bin j is lower than the number of $\mu^- \to e^+$ conversion expected positrons in the same bin using Figure 11.3. In the case of TRIUMF results, the energy measurement window is [92.2-95] MeV, 1.25 RMC-induced positron events are expected against 3.18 events for $\mu^- \to e^+$ conversion The energy measurement window for COMET Phase-I k_{max} precision improvement results is [91.7-95] MeV, and 0.115 RMC-induced positron events are expected versus 4.36 events for $\mu^- \to e^+$ conversion.

A factor of two improvement in the measure of k_{max} reduces the background contribution of RMC by a factor of ten.

11.2 Future work: Acceptance calibration

The acceptance calibration can be performed using two processes: the radiative pion decay and the neutral pion double photon decay, both shown in sections 10.1.1. The goal is to simulate the expected spectrum of the COMET Phase-I and then compare it to the real observed spectrum, like in the TRIUMF experiment [41]. For that, one must know the spectral shape of calibration photons and find a way to improve the number of accepted events. First, the section focus on defining the changes to the COMET Phase-I Experiment setup for the calibration, and at the end of the section, the number of expected events during the calibration is calculated.

11.2.1 Spectral shape: muon stopping target material

There are two issues with the muon stopping target material, first, the RPC spectrum is not known for aluminum. The second, neutral pions are not stopped in the target and can be hard to use for the calibration. However, precise measurements were performed in the past on hydrogen and carbon targets, which have been used in the TRIUMF experiment for their RMC measurement calibration [41]. Thus, these processes can also be used for the RMC calibration of the COMET Phase-I experiment.

Carbon target

To solve the first problem, a carbon target can be used. The spectrum has been measured in the past by Perroud *et al.* [73] and similar calibration have been performed in the TRIUMF experiment [41]. The spectrum and measurements from the TRIUMF experiment are shown in Figure 11.6.

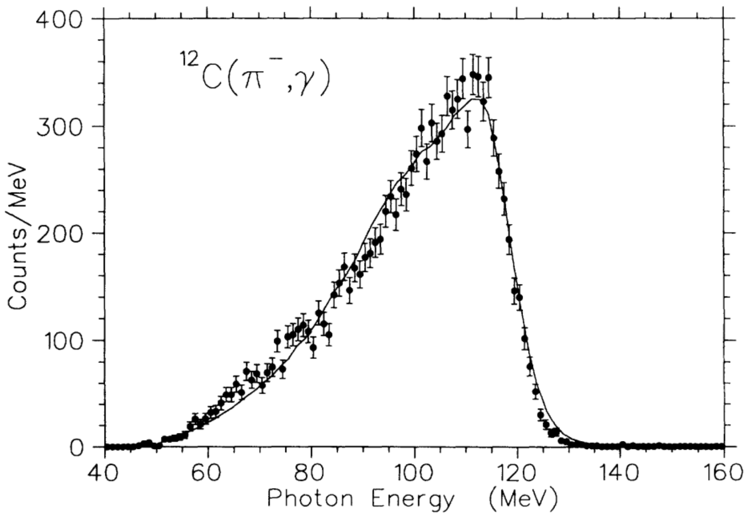

Figure 11.4: Photon energy spectrum from the RPC in ^{12}C compared with the Monte Carlo simulation in the TRIUMF experiment [41]. The data are given by the smooth line and the solid circles are the Monte Carlo results.

Hydrogen target

To create a neutral pion in the detector region, one can use a hydrogen target. A negative pion stopped in the target reacts with the nucleus:

$$\pi^- + p \to \pi^0 + n, \tag{11.3}$$

to create neutral pions in 60% of the cases. The neutral pion obtained then decays into two photons with a probability of 98.8%, producing a uniform photon energy spectrum between 54.9 MeV and 83 MeV. The rest of the negative pions undergo RPC, producing high-energy gamma with an energy of 129.4 MeV. The measurement of γ with a liquid H target by the TRIUMF experiment is shown in Figure 11.5.

11.2.2 Acceptance improvement

Even if the precise spectrum shape is known, the number of events expected for both the calibration processes is too small. To solve this problem, a few changes can be made in the experiment:

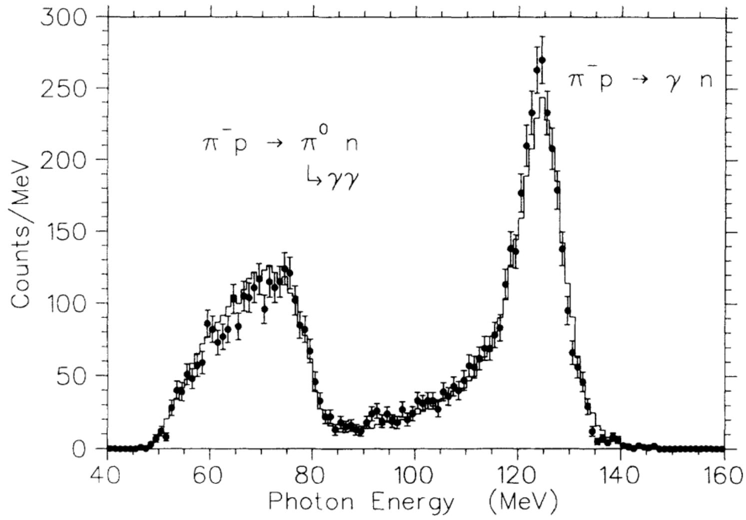

Figure 11.5: Photon energy spectrum from the TRIUMF experiment on a hydrogen target [41]. The data are given by the histrogram line and the solid circles are the Monte Carlo results.

- the measurement window needs to be adapted, and
- the photon conversion rate should be improved.

Measurement window shift

The negative pions arrive in the muon stopping target region around 180 ns after being produced in the pion capture solenoid. But the pionic life time is really short compared to the muonic life time, and thus it almost immediately decays. For this reason, the measurement window should be shifted around the arrival time of the negative pions, and thus start at around 100 ns instead of 700 ns. The only limitation to changing the measurement window is given by the DAQ system, and the performance of the online trigger system. Such a study has not been performed for the RMC online trigger; however, it has been performed for the $\mu^- \rightarrow e^-$ conversion online trigger [59]. For a measurement window with a start time of 100 ns, the online trigger for $\mu^- \rightarrow e^-$ conversion is capable of controlling the trigger rate so that the DAQ can still work while accepting 86% of the signal events. The same value will be used for calculating the number of expected γ events for the calibration because the RMC online trigger is based on the $\mu^- \rightarrow e^-$ conversion online trigger and gives similar results when the measurement window starts at 700 ns.

Conversion rate improvement

The conversion rate of photons in the inner wall of the detector could be improved by adding a lead converter, as shown in Figure 11.6. According to the simulation shown in chapter 4, 61% of the total simulated photons passed by the inner wall, but only 0.081% of these events were converted in the inner wall. This gives a conversion rate of only 0.13%. The photon conversion rate could, in theory, be improved by a factor of 770. However, adding more material will also degrade the energy of particles passing by this material, including the converted electron and positron.

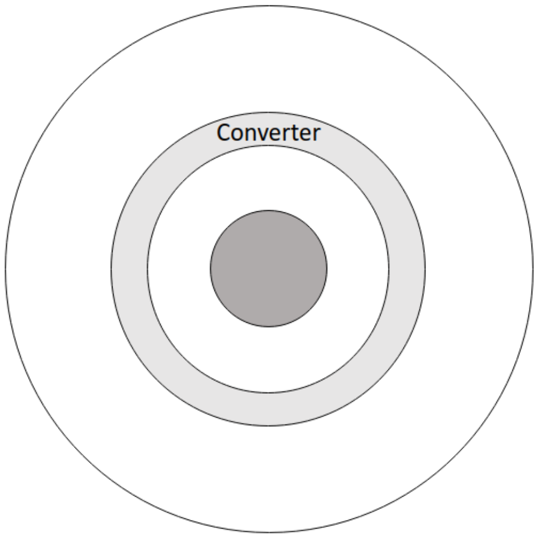

Figure 11.6: XY slice of the COMET Phase-I detector region with a converter

To calculate the effect of the converter on the reconstructed spectrum, a simple Monte-Carlo simulation has been performed. Photons of 90 MeV are directed at a lead wall of thickness x_{th} (converter) where they convert to produce electron-positron pairs. The setup of the simulation is shown in Figure 11.7.

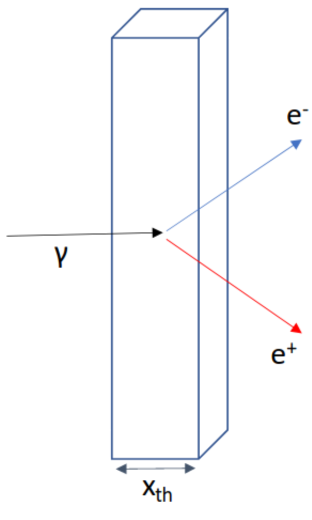

Figure 11.7: Monte-Carlo simulation setup to optimize converter inner wall thickness. Photon sare shoot at a wall with a thickness x_{th} where they convert to produce electron-positron pairs

The electron-positron pair energies are added up to look at the total energy lost inside the converter. The energy of the electron-positron pair distrubtion is shown in Figure 11.8. The ratio corresponds to the number of converted photons—the electron and the positron—that escape the target. The number in parenthesis is the ratio of conversion, but only if the energy of the electron-positron pair that escaped is between 89-90 MeV. E_{loss} value corresponds to the mean energy lost by the electron-positron pair in the converter. This number can be used to choose the best converter thickness, the best conversion thickness is given at 0.5 mm. This distribution is a function of different parameters: the distance traveled by the photon before conversion, the energy distribution between the electron and positron, the energy loss distribution of the electron and positron, and the distance they have to travel in the converter. For a thickness lower than 0.5 mm, the number of photons that convert is lower, but the average energy loss is also lower because the distance traveled by the electron and positron in the converter is smaller. For thicknesses higher than 0.5 mm, the total conversion rate is higher, but the distance that the electron and positron must travel is also increasing. Thus, the energy loss is more consequential.

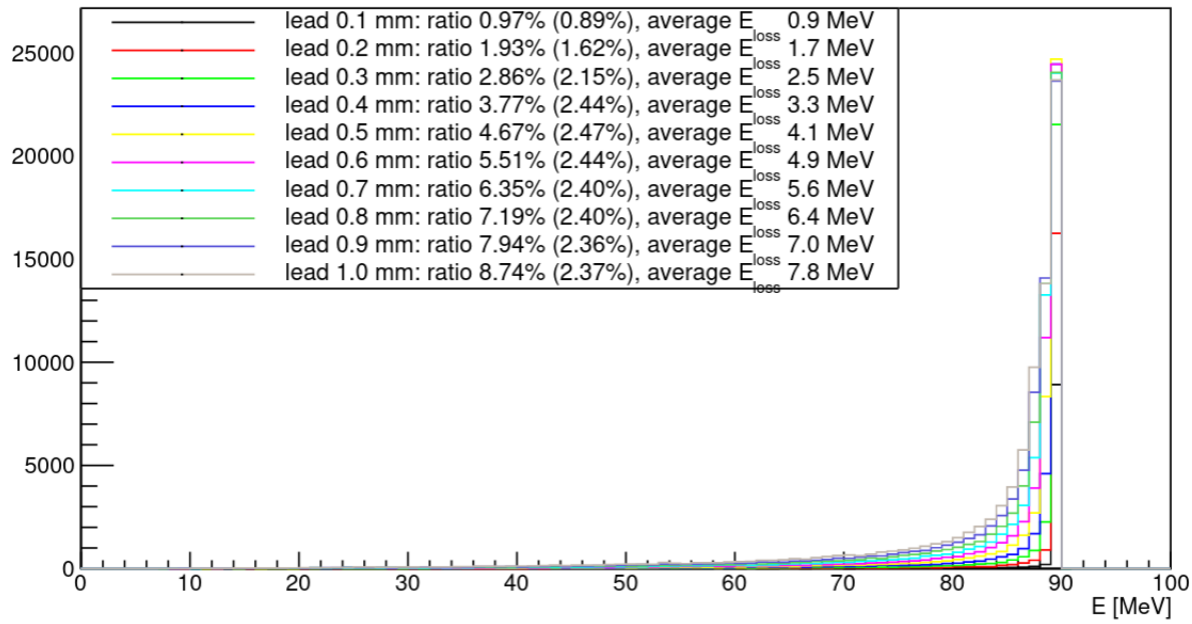

Figure 11.8: Electron-positron pairs energy after escaping the converter for different converter thickness[74]

Figure 11.9 shows, for the events with an energy loss inferior to 1 MeV, the distance between x_{th} and the depth of the conversion. It shows that when the difference is above 0.5 mm there are no entries, and thus the converter should not be thicker than 0.5 mm.

The conversion rate for a lead converter with a 0.5 mm thickness is 2.5%. The current conversion rate is 0.13%, so an improvement of 20 can be made on the conversion rate. In the analysis, the effect of the energy loss tail in the converter needs to be taken into account.

11.2.3 Expected number of event in the calibration

Assuming that the photons have an energy of 65 MeV, the number of event that are expected for the calibration are around 15k events in 1 days of running time. The TRIUMF experiment measured less than 10k events and estimated their error to be 500 keV. The parameters used for the calculation are summarized in Table 11.1.

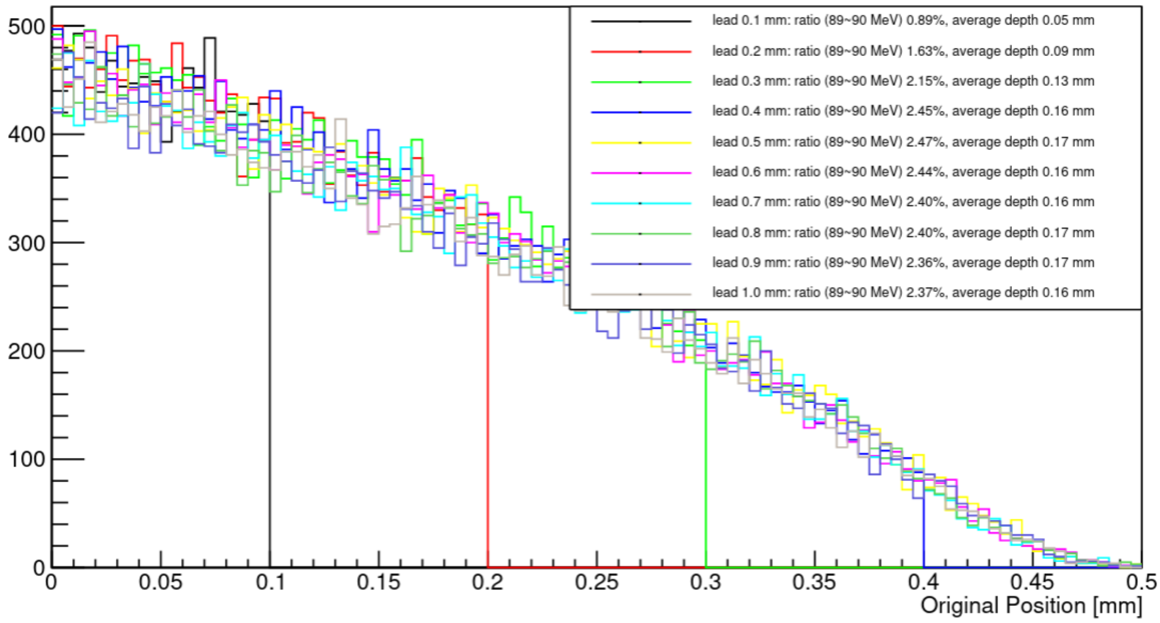

Figure 11.9: Converter thickness minus photon conversion depth for different converter thickness [74]

11.3 Measurement limitation

There are two main limitations to the measurement of $\mu^- \to e^+$ conversion positron due to the RMC spectrum. First, the measurement scheme presented in this study only takes into account external photon conversions, and not the internal conversions. The second limitation is due to the accuracy of the Hwang-Primakoff model. As discussed in chapter 1, the measured k_{max} value is always a few MeV below the maximum allowed energy, $E^{\mathrm{end}}_{\mathrm{RMC}}$. In aluminum, the difference is around 10 MeV. It is possible that photons are emitted with an energy superior to k_{max} which would make the measurement impossible with an aluminum target.

11.3.1 Internal photon spectrum

As explained in section 11.1.2, the part of RMC internal conversion is not known. However, if it is not too small its contribution can be calculated by using two measurements: the RMC γ and positron measurements. After the RMC γ spectrum is measured, the RMC contribution to high energy positron can be calculated as it was done in section 11.1. The predicted and measured positron spectra can be compared to see any-divergence.

The procedure presented in this thesis can also be used to measure the positron spectrum in the COMET Phase-I experiment. Only slight modifications are needed to use the procedure such as the GBDT training, only one hough transform is needed and the parameter optimization may differ.

11.3.2 Hwang-Primakoff model

Nothing prevents a photon with an energy greater than k_{max} from occurring as long as it is less than the maximum allowed energy $E^{\mathrm{end}}_{\mathrm{RMC}}$, as explained in Chapter 1.

Table 11.1: Parameter for the COMET Phase-I calibration number of expected events. The calibration time is expected to take 1 day.

Parameters	Value	Source
N_{proton}	2×10^{17}	COMET Phase-I experiment goal [18]
$R_{\pi-stop/p}$	3.4×10^{-6} ‡	Simulation [18]
B_{RPC}	$1.84\% \pm 0.08$	Branching ratio for ^{12}C[64]
A_{geo}	1.3×10^{-5}	Acceptance for 65 MeV from sec. 4.2.3
Measurement time window	100%	Measurement window adjustment
Lead converter conversion	20	For a 0.5 mm thick lead converter
$\epsilon_{\mathrm{analysis}}$	4%‡‡	Efficiency for 65 MeV sec. 7.3.3

‡ $R_{\pi-stop/p}$ is the value for aluminium target.
‡‡ due to the shift of the measurement window, the background occupancy will be higher. Thus, the efficiency may be lower. An optimization on the intensity of the beam may be needed.

Thus, in addition to the measurement of k_{max}, it is imperative to measure the RMC event in the k_{max}-$E^{\mathrm{end}}_{\mathrm{RMC}}$ region.

However, due to the long tail in the photon energy resolution shown in this study, RMC γ with an energy E_γ greater than k_{max} are already expected. It limits the power of this study to calculate the partial branching ratio $R_{E_\gamma > k_{\mathrm{max}}}$ of event with a E_γ greater than k_{max}. For aluminum, the TRIUMF experiment has shown that $R_{E_\gamma > k_{\mathrm{max}}}$ is at least 3000 times inferior to R_γ. With the current resolution, and $k_{\mathrm{max}} = 90$ MeV, a little bit less than 400 events are expected with an E_γ superior to k_{max}.

The experiment sensitivity to RMC events with E_γ greater than k_{max} can be increased by improving the momentum resolution to RMC γ. The resolution can be improved by strenghtening the quality cuts. For example, increasing the NDF quality cut increases the resolution as shown in chapter 7. However, this comes at the cost of heavily reducing the efficiency of the algorithm and, thus, the number of events that can be used in the analysis.

One way to counteract this effect is to add material to the inner wall to increase the number of photons converting in the inner wall as explained in section 11.2.2. The conversion rate can be improved by a factor of 20.

A more complex quality cut selection can be used to improve the track selection. For example, the track selection after fitting for $\mu^- \to e^-$ conversion electron is currently using a GBDT algorithm, as explained in appendix B. This offers better control over the high-energy tail and thus should also be adapted to the RMC measurement.

Chapter 12

Conclusion

For the COMET Phase-I experiment to measure RMC with an aluminum target, an analysis procedure has been developed. This procedure is based on a mix of GBDT algorithm and the circular Hough transform, and the fitting is performed using the GENFIT algorithm. This procedure has been tested on simulation data. As a result, the COMET Phase-I experiment will be able to collect approximately 16k RMC events over the course of 100 days.

Additionally, the online trigger scheme for $\mu^- \to e^-$ conversion (see [59]) has been adapted to the RMC measurement. It yields a rejection power of 96% for an acceptance of RMC event of 90%. This reduces the trigger rate to 4 kHz, six times lower than the rate required by the DAQ system.

Owing to a likelihood analysis, the endpoint spectrum and the partial branching of RMC have been estimated for initial values. For a running time of the COMET Phase-I experiment of 100 days, the endpoint of the RMC spectrum $k_{\max}$ for aluminum can be measured with a precision of $(\pm 0.17(stat.) \pm 0.65(syst.))$ MeV, which is an improvement of a factor 2 over the current value. Similarly, the partial branching ratio R_γ can be measured at a precision of $\pm 1.1\%(stat.) \pm 8.7\%(syst.)$.

The reduction of the background of RMC contamination to $\mu^- \to e^+$ conversion within the Primakoff closure approximation model was calculated. The improvement by a factor of 2 on the precision of $k_{\max}$, helps reduce the number of RMC-induced positrons in the measurement region of $\mu^- \to e^+$ conversion by a factor of 10.

Appendix A

Gradient boosted decision trees

This annex describes the basics of GBDT algorithms, from how to build a decision tree to the use of gradient-boosted techniques.

A.1 Decision Tree

GBDT algorithm is based on binary decision trees. A decision tree, is a succession of nodes used to classify a dataset, a way of thinking and so on. Each node represents a condition. A binary decision tree is tree were a node can have at most only 2 children nodes.

Figure A.1 shows an example of a binary decision tree. The value $x(x_1, x_2, x_m)$ represents the different features of a specific hit. In the example of hit filtering, x_1 can be the energy deposit, and x_2 can be the timing of a hit and so on. c_0 and c_1 are different cuts that can be used to differentiate the background from signal data. The end of a tree is given by a leaf; in the leaf a value different w_i is given to the hit. The closer this hit features are to a signal hit, the higher its w_i value is.

The depth of a tree is virtually infinite; however, growing a decision tree to infinitly is prone to over-fitting, over-training and can loose its prediction power. To avoid this, the depth of a tree is often limited by a maximum depth factor, and by requiring a minimum of the data size still being present before calculating a node.

To choose which parameter will be used at the top of a node, the Gini Impurity factor [1] is calculated for each condition. The Gini Impurity number G is defined as:

$$G = 1 - p^2_{\text{Signal}} - p^2_{\text{Background}}, \tag{A.1}$$

where p_{Signal} is the probability of a sample to belong to the signal and $p_{\text{Background}}$ is the probability of a sample to belong to the background.

The gini must be calculated for both True, and False case outcome. Then, the total Gini Impurity is given by the weighted sum of the different Gini Impurity. The variable and condition giving the lower Gini impurity is chosen to represent the current node.

Calculating the Gini impurity for every possible condition is really time consuming; thus, a binning is used for non-boolean variable. The Gini impurity is calculated

[1]There exist different factor to measure the impurity, however this study only use the Gini impurity factor to decide which parameter is more suitable as a condition

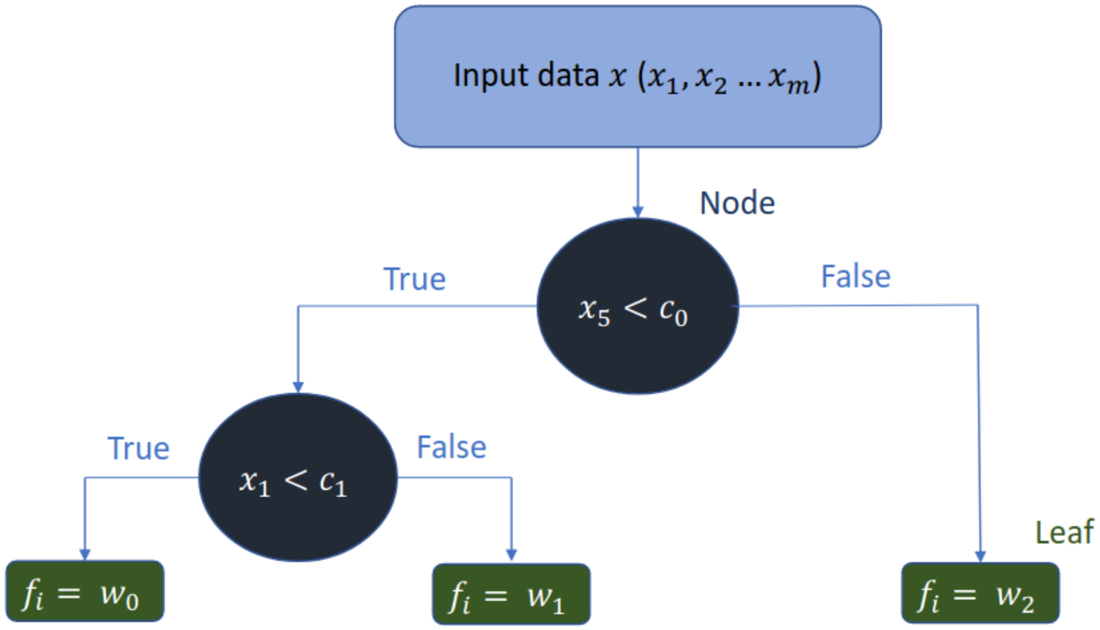

Figure A.1: Sketch of a decision tree. The tree have a depth of 2.

for N-1 bin.

As an example, the ADC sum distribution for signal and background is shown in Figure A.2 from chapter 5, and the number of bins will be 5. The data is distributed between 0 and 1350 thus the bin size will be of 270 ADC sum.

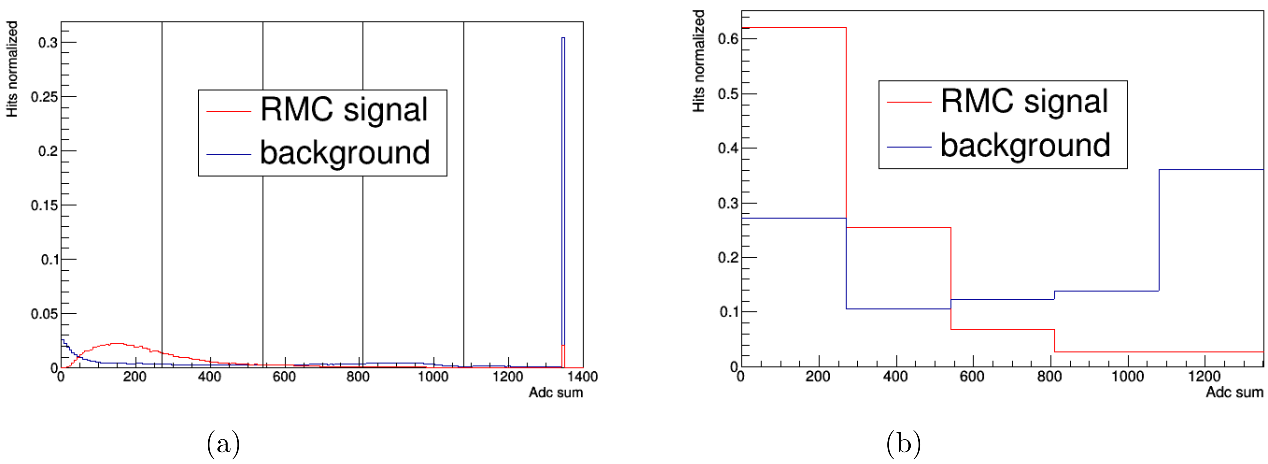

Figure A.2: ADC distribution for RMC signal and for background from chapter 5 with a thin binning of 8 ADC per bin (a) and with a thick binning of 270 ADC per bin (b)

The gini impurity is calculated for the four possible conditions 270, 540, 710 and 1080. For the conditions $ADCsum < 270$, there is 0.620 signal hits, and 0.272 background hits that pass the distribution. This gives a gini impurity of 0.424. There is 0.379 signal hit and 0.727 bg hits that donot pass the distribution. This

Table A.1: Gini impurity values calculation for different condition on the ADC values

Conditions	Gini Truth	Gini false	Gini impurity
ADC <270	0.424	0.450	0.881
ADC <540	0.421	0.276	0.707
ADC <710	0.452	0.178	0.635
ADC <1080	0.478	0.130	0.632

gives a gini impurity of 0.450. The total gini impurity is given by normalizing the gini impurities and adding them together; it gives a total gini impurity of 0.881 for the condition $ADCsum < 270$.

The results for all Gini impurity are given in Table A.1. The total lowest gini impurity is given by $ADC\ sum < 1080$. Thus, it is chosen as the cut for the current node.

A.2 Gradient boosted tree

Gradient boosted trees are a collection of small classification trees with small prediction power but that are combined together to give a higher prediction values. Gradient boosted tree output is given by:

$$F(x) = \sum_{i=0}^{M} \alpha_i f_i(x), \tag{A.2}$$

where $f_i(x)$ corresponds to different decision trees. The weighting factors α_i are obtained by minimizing the loss-function. Figure A.3 shows how the GBDT works.

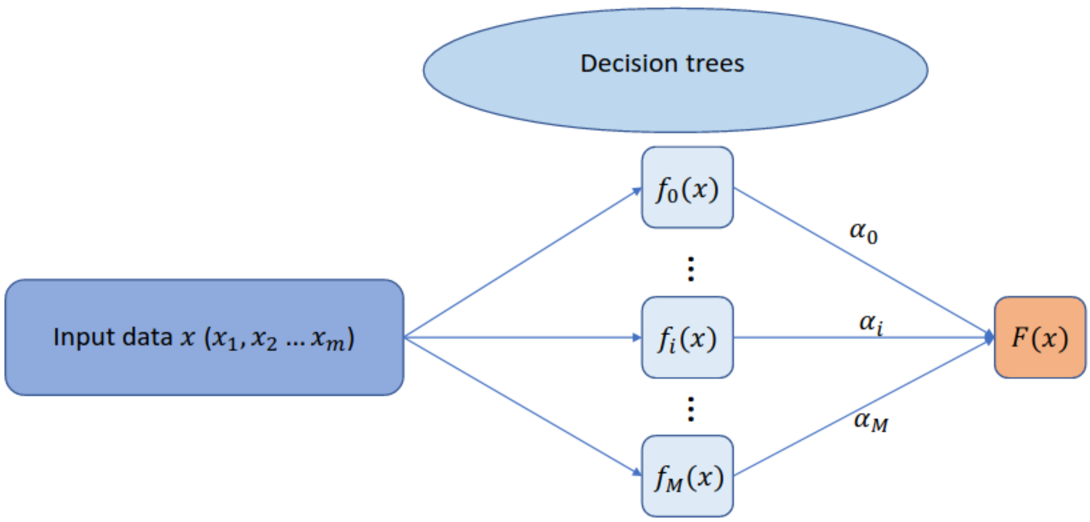

Figure A.3: Sketch of a gradient boosted tree architecture

Appendix B

Multiple Variable Analysis of track fitting quality cut

A track quality cut using a GBDT algorithm is under development to reduce the right part of the fitting tail. For now, it has only been tested for $\mu^- \to e^-$ conversion (105 MeV electrons), but it may be used in the future for the $\mu^- \to e^+$ conversion, the RMC, and so on.

The original idea is inspired by [75] where they are using artificial neural networks to remove high-energy tail events from their results. The same way, the COMET Phase-I (COMET Phase-I) experiment wants to remove the high-energy tail events as they will contribute to the background contamination from DIO electrons. The current study only considers 105 MeV single turn electrons, with no background and perfect seed for the fitting.

B.1 GBDT

This study focuses on the residue after fitting. The residue is defined by:

$$residue = |\overrightarrow{P_{fitted}}| - |\overrightarrow{P_{truth\ 1st\ hit\ in\ detector}}|. \tag{B.1}$$

Thus, the higher the residue is the higher the chance of having the DIO electron spectrum overlapping with the $\mu^- \to e^-$ conversion spectrum.

B.1.1 Training and parameters

For the training, the data are separated into two categories: good events (with a $|residue| < 1MeV$) and bad events (with a $residue > 2MeV$).

The goal is only to target the right part of the tail. The left part of the tail is due to the electron scattering inside of the chamber is it not harmful to the $\mu^- \to e^-$ conversion measurement.

The GBDT is using the eight parameters:

- the number of hit,
- the NDF,
- the χ^2,

- the χ^2/NDF,
- the maximum layer reached by the electron track (after fitting),
- the Genfit error matrix Longitudinal position,
- the Genfit error matrix Longitudinal momentum, and
- the fitted longitudinal momentum.

Number of hit The number of hit parameters is the number of hits used in the fitting by GENFIT. The distribution is shown in Figure B.1. The difference between the bad and good events is not striking, but the number of hits for bad events is usually slightly lower than that for the good events.

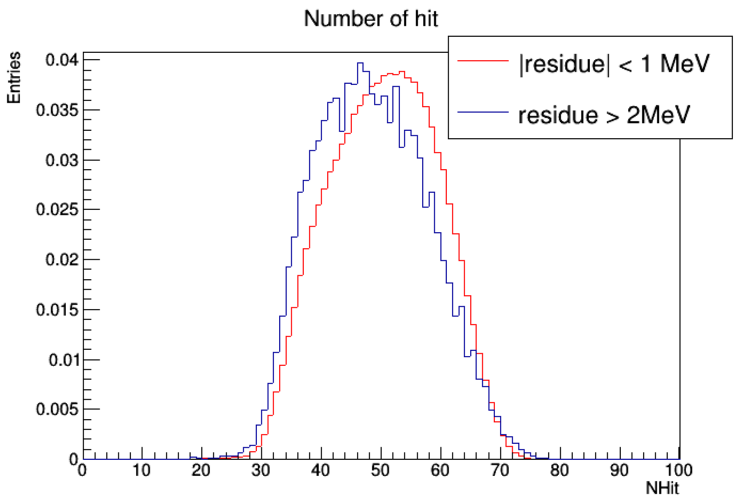

Figure B.1: Number of hit given to the fitting

NDF The NDF is the degree of freedom of the fit. It can be calculated by:

$$NDF = Nhit - N_{fitting\ parameters}, \tag{B.2}$$

where $N_{fitting\ parameters}$ is the number of parameters of an helix (6). The NDF distribution is shown in Figure B.2. Bad fitting events have a lower NDF, than good fitting events. The difference is mainly due to the number of hits that are dropped by the fitting algorithm.

χ^2 and χ^2/NDF The χ^2 is defined as:

$$\chi^2 = \sum_{i}^{N} \frac{(x_i - m_i)^2}{\sigma}, \tag{B.3}$$

where N is the total number of fitted hits, x_i is the fitted value for measurement for hit i, m_i is the measured value for hit i. σ is the fitting resolution. The fitting is performed to minimize the value of χ^2.

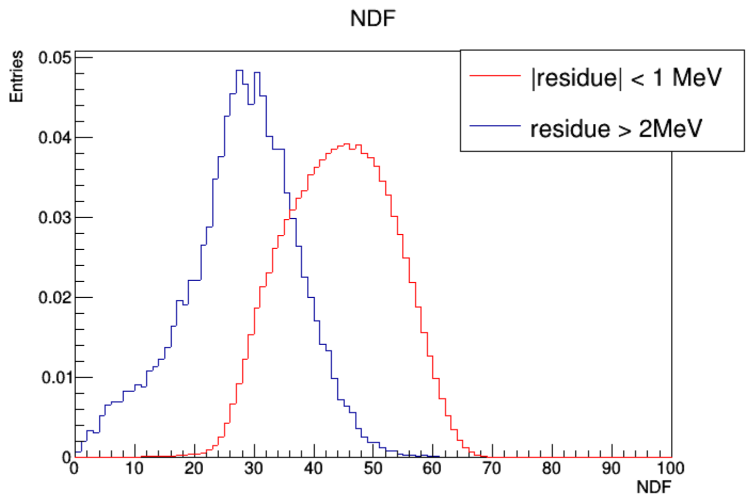

Figure B.2: NDF from the fitting

Usually, good fitting has χ^2/NDF distributed around 1. Figure B.3 shows the χ^2 and χ^2/NDF distributions. The bad-fitted event and good-fitted clearly different distributions. For χ^2/NDF, the good event are distributed around 1 while bad event are distributed around 3.

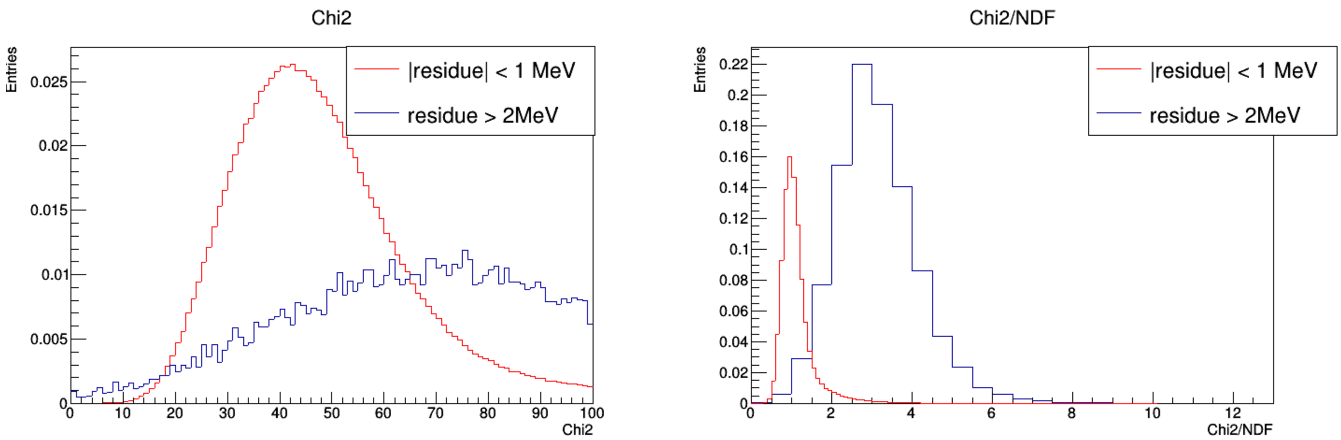

(a)

(b)

Figure B.3: χ^2 and χ^2/NDF for bad fitted event and for well fitted events

Maximum layer reached by the electron track Only event with the electron reaching the 5th layer of the detector have been considered. Figure B.4 shows the distribution of the maximum layer for bad fitted event and good fitted events. Bad fitted event distribution peak at 5, while a signal peak around 9-10 layers reached.

Fitted longitudinal momentum Due to the geometry of the detector, fitting the trajectory in the transverse plane is not too difficult; however, fitting in the longitudinal plane is harder. Thus, the fitted longitudinal momentum can easily diverge from the true value. Figure B.5 shows the distribution of the fitted z momentum for event with a $|residue| < 1MeV$ and for event with a $residue > 2MeV$.

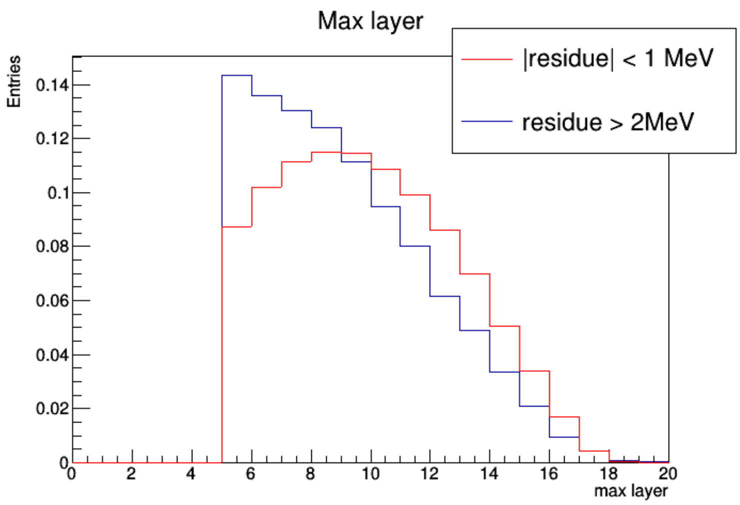

Figure B.4: Maximum layer event

For events with a $residue > 2MeV$, there is a tail over 80 , and -80 MeV not present for the good events, with the COMET Phase-I Experiment, no event with such high longitudinal momentum should be able to reach the detector and at least reach the 5th layer of the detector.

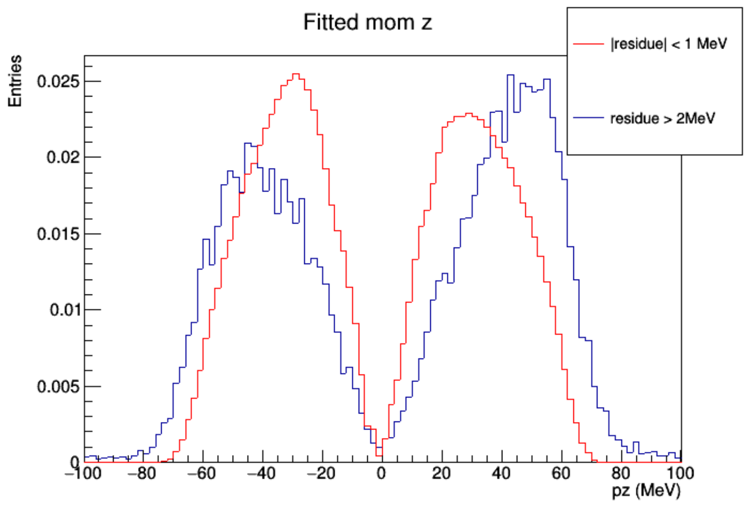

Figure B.5: Fitted Pz

Genfit error matrix : Longitudinal position and Longitudinal momentum As seen previously, the longitudinal position and momentum can be difficult to recover. However, Genfit provides the matrix error for the fitting on position(X,Y,Z) and momentum (X,Y, Z; thus, thus it can be used as an input for differentiating bad fitting events from good fitting events. Figure B.6 shows the distribution of these errors.

B.1.2 GBDT results

Below, one can see the input parameters ranked by their separation power [60]. A separation of 0 is a total overlap between the background and signal distribution,

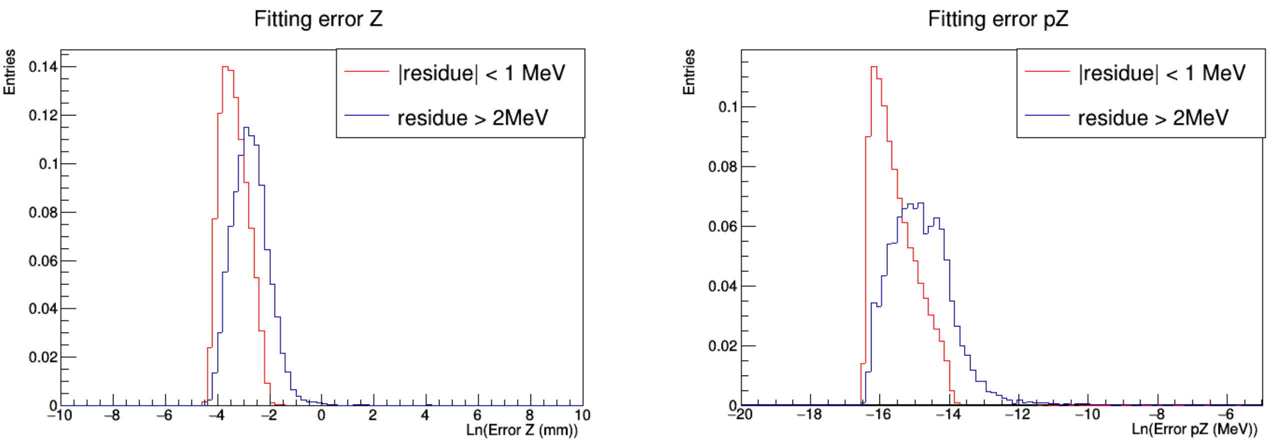

(a)

(b)

Figure B.6: Genfit longitudinal position (a) and momentum (b) fitting error

while a separation power of 1 indicates a total separation between the background and the signal distribution:

- χ^2/NDF — 0.1676
- Number of hit — 0.1641
- Fitted longitudinal momentum — 0.1174
- χ^2 — 0.1167
- NDF — 0.1140
- Genfit error matrix Longitudinal momentum — 0.0812
- Genfit error matrix Longitudinal position — 0.0723
- Maximum layer reached by the electron track (after fitting) — 0.0655

Figure B.7 shows the distribution of the score given by the GBDT algorithm to badly fitted event and to well -fitted events. They are easily separated by the GBDT algorithm.

B.2 Residue

Instead of applying a simple on GBDT score, like in [75], only the 80% tracks with the best score are kept. The results are shown in Figure B.8, and are compared to the residue without any cut. 80% of the events are kept, and the right tail is constrained below 3 MeV.

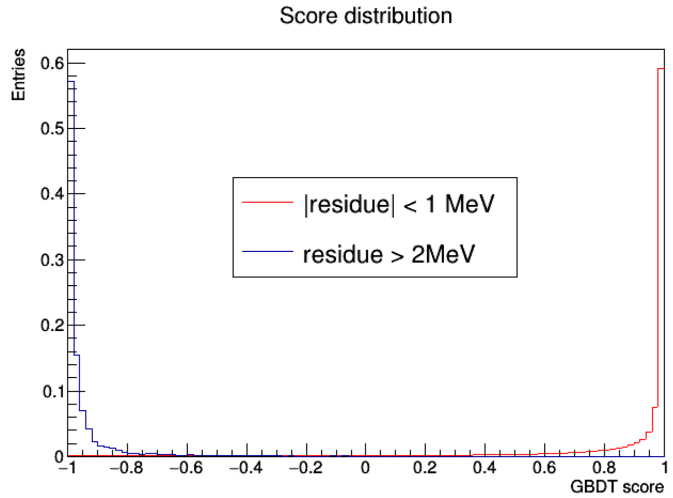

Figure B.7: Score distribution

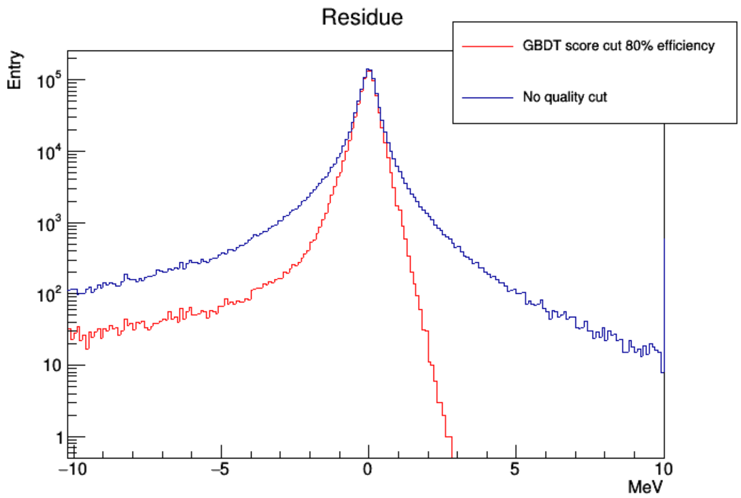

Figure B.8: Residue distribution by taking the best 80% fitted events according to the GBDT score and without cut

Bibliography

[1] T. Aaltonen et al. "High-precision measurement of the W boson mass with the CDF II detector". In: *Science* 376.6589 (2022), pp. 170–176.

[2] H.Yukawa. "On the interaction of Elementary Particles". In: *Proceedings of the Physico-Mathematical Society of Japan* (1935).

[3] G. P. S. Occhialini and C. F. Powell. "Nuclear Disintegrations produced by slow charged particles of small mass". In: *Nature* (1947). DOI: 10.1038/159186a0. URL: https://doi.org/10.1038/159186a0.

[4] R.H. Bernstein and Peter S. Cooper. "Charged lepton flavor violation: An experimenter's guide". In: *Physics Reports* 532.2 (2013). Charged Lepton Flavor Violation: An Experimenter's Guide, pp. 27–64. ISSN: 0370-1573. DOI: https://doi.org/10.1016/j.physrep.2013.07.002. URL: https://www.sciencedirect.com/science/article/pii/S0370157313002688.

[5] Y. Fukuda et al. "Evidence for Oscillation of Atmospheric Neutrinos". In: *Phys. Rev. Lett.* 81 (8 1998), pp. 1562–1567. DOI: 10.1103/PhysRevLett.81.1562. URL: https://link.aps.org/doi/10.1103/PhysRevLett.81.1562.

[6] Q. R. Ahmad et al. "Direct Evidence for Neutrino Flavor Transformation from Neutral-Current Interactions in the Sudbury Neutrino Observatory". In: *Phys. Rev. Lett.* 89 (1 2002), p. 011301. DOI: 10.1103/PhysRevLett.89.011301. URL: https://link.aps.org/doi/10.1103/PhysRevLett.89.011301.

[7] Q. R. Ahmad et al. "Measurement of the Rate of $\nu_e + d \to p + p + e^-$ Interactions Produced by ^8B Solar Neutrinos at the Sudbury Neutrino Observatory". In: *Phys. Rev. Lett.* 87 (7 2001), p. 071301. DOI: 10.1103/PhysRevLett.87.071301.

[8] Sergio Palomares-Ruiz and S.T. Petcov. "Three-neutrino oscillations of atmospheric neutrinos,θ_{13}, neutrino mass hierarchy and iron magnetized detectors". In: *Nuclear Physics B* 712.1-2 (2005), pp. 392–410. DOI: 10.1016/j.nuclphysb.2005.01.045. URL: https://doi.org/10.1016%2Fj.nuclphysb.2005.01.045.

[9] S. M. Bilenky and S. T. Petcov. "Massive neutrinos and neutrino oscillations". In: *Rev. Mod. Phys.* 59 (3 1987), pp. 671–754. DOI: 10.1103/RevModPhys.59.671. URL: https://link.aps.org/doi/10.1103/RevModPhys.59.671.

[10] W. J. Marciano and A. I. Sanda. "Reaction $\mu^- +$ Nucleus $\to e^- +$ Nucleus in Gauge Theories". In: *Phys. Rev. Lett.* 38 (26 1977), pp. 1512–1515. DOI: 10.1103/PhysRevLett.38.1512. URL: https://link.aps.org/doi/10.1103/PhysRevLett.38.1512.

[11] B. W. Lee et al. “Muon and Electron Number Nonconservation in a $V-A$ Gauge Model”. In: *Phys. Rev. Lett.* 38 (17 1977), pp. 937–939. DOI: 10.1103/PhysRevLett.38.937. URL: https://link.aps.org/doi/10.1103/PhysRevLett.38.937.

[12] Wolfgang Altmannshofer et al. “Anatomy and phenomenology of FCNC and CPV effects in SUSY theories”. In: *Nuclear Physics B* 830.1-2 (2010), pp. 17–94. DOI: 10.1016/j.nuclphysb.2009.12.019. URL: https://doi.org/10.1016%2Fj.nuclphysb.2009.12.019.

[13] Kaustubh Agashe and Christopher D. Carone. “Supersymmetric flavor models and the $\vec{B}_{\phi K_S}$ anomaly”. In: *Physical Review D* 68.3 (2003). DOI: 10.1103/physrevd.68.035017. URL: https://doi.org/10.1103%2Fphysrevd.68.035017.

[14] Graham G. Ross, Liliana Velasco-Sevilla, and Oscar Vives. “Spontaneous CP violation and non-Abelian family symmetry in SUSY”. In: *Nuclear Physics B* 692.1-2 (2004), pp. 50–82. DOI: 10.1016/j.nuclphysb.2004.05.020. URL: https://doi.org/10.1016%2Fj.nuclphysb.2004.05.020.

[15] Stefan Antusch, Stephen F King, and Michal Malinský. “Solving the SUSY flavour and CP problems with SU(3) family symmetry”. In: *Journal of High Energy Physics* 2008.06 (2008), pp. 068–068. DOI: 10.1088/1126-6708/2008/06/068. URL: https://doi.org/10.1088%2F1126-6708%2F2008%2F06%2F068.

[16] Monika Blanke et al. “Particle-antiparticle mixing, ϵ_K, $\Delta\Gamma_q$, A^q_{SL} in the Littlest Higgs model with T-parity”. In: *Journal of High Energy Physics* 2006.12 (2006), pp. 003–003. DOI: 10.1088/1126-6708/2006/12/003. URL: https://doi.org/10.1088%2F1126-6708%2F2006%2F12%2F003.

[17] Monika Blanke et al. “Rare K and B Decays in a warped extra dimension with custodial protection”. In: *Journal of High Energy Physics* 2009.03 (2009), pp. 108–108. DOI: 10.1088/1126-6708/2009/03/108. URL: https://doi.org/10.1088%2F1126-6708%2F2009%2F03%2F108.

[18] The COMET Collaboration. “COMET Phase-I Technical Design Report”. In: *Progress of Theoretical and Experimental Physics* (2020). DOI: 10.1093/ptep/ptz125.

[19] L. Bartoszek et al. *Mu2e Technical Design Report*. 2015. DOI: 10.48550/ARXIV.1501.05241. URL: https://arxiv.org/abs/1501.05241.

[20] H.V.Klapdor et al. *Lepton and Baryon Number Violation in Particle Physics, Astrophysics and Cosmology*. 1999. DOI: 10.1201/9781482268638.

[21] Wilhelm H. Bertl et al. “A search for μ^--e conversion in muonic gold”. In: *The European Physical Journal C - Particles and Fields* (2006). DOI: 10.1140/epjc/s2006-02582-x. URL: https://doi.org/10.1140/epjc/s2006-02582-x.

[22] Stefano Dell’Oro et al. “Neutrinoless Double Beta Decay: 2015 Review”. In: *Advances in High Energy Physics* 2016 (2016), pp. 1–37. DOI: 10.1155/2016/2162659. URL: https://doi.org/10.1155%2F2016%2F2162659.

[23] Anupama Atre, Vernon Barger, and Tao Han. "Upper bounds on lepton-number violating processes". In: *Physical Review D* 71.11 (2005). DOI: 10.1103/physrevd.71.113014. URL: https://doi.org/10.1103%2Fphysrevd.71.113014.

[24] Jeffrey M. Berryman et al. "Lepton-number-violating searches for muon to positron conversion". In: *Phys. Rev. D* 95 (11 2017), p. 115010. DOI: 10.1103/PhysRevD.95.115010. URL: https://link.aps.org/doi/10.1103/PhysRevD.95.115010.

[25] Chian-Shu Chen, C. Q. Geng, and J. N. Ng. "Unconventional neutrino mass generation, neutrinoless double beta decays, and collider phenomenology". In: *Physical Review D* 75.5 (2007). DOI: 10.1103/physrevd.75.053004. URL: https://doi.org/10.1103%2Fphysrevd.75.053004.

[26] V. Cirigliano et al. "Neutrinoless Double Beta Decay and Lepton Flavor Violation". In: *Physical Review Letters* 93.23 (2004). DOI: 10.1103/physrevlett.93.231802. URL: https://doi.org/10.1103%2Fphysrevlett.93.231802.

[27] Stephen F. King, Alexander Merle, and Luca Panizzi. "Effective theory of a doubly charged singlet scalar: complementarity of neutrino physics and the LHC". In: *Journal of High Energy Physics* 2014.11 (2014). DOI: 10.1007/jhep11(2014)124. URL: https://doi.org/10.1007%2Fjhep11%282014%29124.

[28] P.C. Divari et al. "The exotic double-charge exchange $\mu^- \to e^+$ conversion in nuclei". In: *Nuclear Physics A* 703.1-2 (2002), pp. 409–431. DOI: 10.1016/s0375-9474(01)01533-0. URL: https://doi.org/10.1016%2Fs0375-9474%2801%2901533-0.

[29] Leslie L. Foldy and John Dirk Walecka. "Muon capture in nuclei". In: *Il Nuovo Cimento (1955-1965)* 34 (1964), pp. 1026–1061.

[30] K A Snover. "Giant Resonances in Excited Nuclei". In: *Annual Review of Nuclear and Particle Science* 36.1 (1986), pp. 545–603. DOI: 10.1146/annurev.ns.36.120186.002553. eprint: https://doi.org/10.1146/annurev.ns.36.120186.002553. URL: https://doi.org/10.1146/annurev.ns.36.120186.002553.

[31] J. Kaulard et al. "Improved limit on the branching ratio of $\mu^-\to$e+ conversion on titanium". In: *Physics Letters B* 422.1 (1998), pp. 334–338. ISSN: 0370-2693. DOI: https://doi.org/10.1016/S0370-2693(97)01423-8. URL: https://www.sciencedirect.com/science/article/pii/S0370269397014238.

[32] Jeremy Bernstein. "Radiative Muon Capture". In: *Phys. Rev.* 115 (3 1959), pp. 694–705. DOI: 10.1103/PhysRev.115.694. URL: https://link.aps.org/doi/10.1103/PhysRev.115.694.

[33] H.P.C. Rood and H.A. Tolhoek. "Radiative muon-capture in complex nuclei". In: *Physics Letters* 6.1 (1963), pp. 121–122. ISSN: 0031-9163. DOI: https://doi.org/10.1016/0031-9163(63)90246-4. URL: https://www.sciencedirect.com/science/article/pii/0031916363902464.

[34] Harold W. Fearing. "Relativistic calculation of radiative muon capture in hydrogen and 3He". In: *Phys. Rev. C* (1980).

[35] F E Low. “Bremsstrahlung of very low-energy Quante I Elementary Particle Collisions”. In: *Physical Review (U.S.) Superseded in part by Phys. Rev. A, Phys. Rev. B: Solid State, Phys. Rev. C, and Phys. Rev. D* (). DOI: 10.1103/PhysRev.110.974. URL: https://www.osti.gov/biblio/4302068.

[36] S. L. Adler and Y. Dothan. “Low-Energy Theorem for the Weak Axial-Vector Vertex”. In: *Phys. Rev.* 151 (4 1966), pp. 1267–1277. DOI: 10.1103/PhysRev.151.1267. URL: https://link.aps.org/doi/10.1103/PhysRev.151.1267.

[37] P. Christillin and S. Servadio. “About low-energy expansion of two-current amplitudes”. In: *Il Nuovo Cimento A (1965-1970)* (1977). URL: https://doi.org/10.1007/BF02724581.

[38] P. Christillin, M. Rosa-Clot, and S. Servadio. “Radiative muon capture in medium-heavy nuclei”. In: *Nuclear Physics A* 345.2 (1980), pp. 331–366. ISSN: 0375-9474. DOI: https://doi.org/10.1016/0375-9474(80)90344-9. URL: https://www.sciencedirect.com/science/article/pii/0375947480903449.

[39] W Y. P. Hwang. “Radiative muon capture”. In: *Phys. Rev. C* 22 (1 1980), pp. 233–246. DOI: 10.1103/PhysRevC.22.233. URL: https://link.aps.org/doi/10.1103/PhysRevC.22.233.

[40] M. Gmitro and A. A. Ovchinnikova. “Continuity-equation constraint for electron scattering and radiative muon capture”. In: *Czechoslovak Journal of Physics B* (1986). URL: https://doi.org/10.1007/BF01597844.

[41] D. S. Armstrong et al. “Radiative muon capture on Al, Si, Ca, Mo, Sn, and Pb”. In: *Phys. Rev. C* 46 (3 1992), pp. 1094–1107. DOI: 10.1103/PhysRevC.46.1094. URL: https://link.aps.org/doi/10.1103/PhysRevC.46.1094.

[42] T. P. Gorringe et al. “Isotope dependence of radiative muon capture on the ^{58,60,62}Ni isotopes”. In: *Phys. Rev. C* 58 (3 1998), pp. 1767–1776. DOI: 10.1103/PhysRevC.58.1767. URL: https://link.aps.org/doi/10.1103/PhysRevC.58.1767.

[43] P.C.Bergbusch et al. “Radiative muon capture on O, Al, Si, Ti, Zr and Ag”. In: (1999).

[44] D.H. Wright et al. “The TRIUMF radiative muon capture facility”. In: *Nuclear Instruments and Methods in Physics Research Section A: Accelerators, Spectrometers, Detectors and Associated Equipment* 320.1 (1992), pp. 249–262. ISSN: 0168-9002. DOI: https://doi.org/10.1016/0168-9002(92)90783-Z. URL: https://www.sciencedirect.com/science/article/pii/016890029290783Z.

[45] L. L. Foldy and J. D. Walecka. “Coupling Constants in Muon Capture”. In: *Phys. Rev.* 147 (3 1966), pp. 886–886. DOI: 10.1103/PhysRev.147.886. URL: https://link.aps.org/doi/10.1103/PhysRev.147.886.

[46] R. Parthasarathy and V.N. Sridhar. “Effect of meson exchange corrections on allowed muon capture”. In: *Physics Letters B* 106.5 (1981), pp. 363–366. ISSN: 0370-2693. DOI: https://doi.org/10.1016/0370-2693(81)90642-0. URL: https://www.sciencedirect.com/science/article/pii/0370269381906420.

[47] M. Kobayashi et al. "Average polarization of 12B in polarized muon capture". In: *Nuclear Physics A* 312.3 (1978), pp. 377–393. ISSN: 0375-9474. DOI: https://doi.org/10.1016/0375-9474(78)90598-5. URL: https://www.sciencedirect.com/science/article/pii/0375947478905985.

[48] M. MacKenzie and P. Murat. *Search for $\mu^- \to e^+$ conversion: what can be learned from the SINDRUM-II positron data on a gold target.* 2020. DOI: 10.48550/ARXIV.2009.00214. URL: https://arxiv.org/abs/2009.00214.

[49] Andrzej Czarnecki and Xavier Gartcia i Tormo. "Muon decay in orbit: Spectrum of high-energy electrons". In: (2011).

[50] Evgeny Karpechev et al. "Study of energy dependence of pion production by proton on copper target near 350 MeV". In: *Physics of Atomic Nuclei* 71 (Jan. 2008), pp. 1–8. DOI: 10.1134/S1063778808010018.

[51] D Möhl. "Production of low-energy antiprotons". In: *Hyperfine Interactions* (1997). URL: https://doi.org/10.1023/A:1012680728257.

[52] C.Wu and Y.Fuji. "Personnal communications". In: (2022).

[53] E.R. Davies. "A modified Hough scheme for general circle location". In: (1988).

[54] R. E. Kalman. "A New Approach to Linear Filtering and Prediction Problems". In: *Journal of Basic Engineering* 82.1 (Mar. 1960), pp. 35–45. ISSN: 0021-9223. DOI: 10.1115/1.3662552. eprint: https://asmedigitalcollection.asme.org/fluidsengineering/article-pdf/82/1/35/5518977/35_1.pdf. URL: https://doi.org/10.1115/1.3662552.

[55] Lidner. "Evolution of the T2K-ND280 Computing Model". In: (2015).

[56] S. Agostinelli et al. "Geant4—a simulation toolkit". In: *Nuclear Instruments and Methods in Physics Research Section A: Accelerators, Spectrometers, Detectors and Associated Equipment* 506.3 (2003), pp. 250–303. ISSN: 0168-9002. DOI: https://doi.org/10.1016/S0168-9002(03)01368-8. URL: https://www.sciencedirect.com/science/article/pii/S0168900203013688.

[57] Francesc Salvat et al. "PENELOPE-2008: A Code System for Monte Carlo Simulation of Electron and Photon Transport". In: (2008).

[58] Baro et al. "Analytical cross sections for Monte Carlo simulation of photon transport". In: (1994).

[59] Yu Nakazawa. "A Trigger System with Online Track Recognition for the μ^-–e Conversion Search in the COMET Phase-I Experiment". In: (2020).

[60] Andreas Hoecker et al. "TMVA: Toolkit for Multivariate Data Analysis". In: *PoS* ACAT (2007), p. 040. arXiv: physics/0703039.

[61] Y.Kuno C.Wu T.Wong. "Track Fitting of COMET CDC". In: (2018).

[62] T.Suzuki and D.F. Measday. "Total nuclear capture rates for negative muons". In: (1987).

[63] S. S. Wilks. "The Large-Sample Distribution of the Likelihood Ratio for Testing Composite Hypotheses". In: *The Annals of Mathematical Statistics* 9.1 (1938), pp. 60 –62. DOI: 10.1214/aoms/1177732360. URL: https://doi.org/10.1214/aoms/1177732360.

[64] J.E. Amaro et al. "Radiative pion capture in nuclei: a continuum shell–model approach". In: (1997).

[65] T.Xing. "Personnal communications". In: (2022).

[66] John R. de Laeter et al. "Atomic weights of the elements. Review 2000 (IUPAC Technical Report)". In: *Pure and Applied Chemistry* 75.6 (2003), pp. 683–800. DOI: doi:10.1351/pac200375060683. URL: https://doi.org/10.1351/pac200375060683.

[67] P.C.Bergbusch et al. "Radiative Muon Capture On Oxygen, Aluminum, Silicon, Titanium, Zirconium, and Silver". In: (1993).

[68] John Quirk. "Preliminary results from the AlCap Experiment". In: (2019).

[69] C. Wu et al. "Test of a small prototype of the COMET cylindrical drift chamber". In: *Nuclear Instruments and Methods in Physics Research Section A: Accelerators, Spectrometers, Detectors and Associated Equipment* 1015 (2021), p. 165756. DOI: 10.1016/j.nima.2021.165756. URL: https://doi.org/10.1016%2Fj.nima.2021.165756.

[70] Ting Sam Wong. "Study of Negative Muon to Positron Conversion in the COMET Phase-I experiment". In: (2020).

[71] N. P. Samios. "Dynamics of Internally Converted Electron-Positron Pairs". In: *Phys. Rev.* 121 (1 1961), pp. 275–281. DOI: 10.1103/PhysRev.121.275. URL: https://link.aps.org/doi/10.1103/PhysRev.121.275.

[72] Tanja Geib, Alexander Merle, and Kai Zuber. "μ^-–e+ conversion in upcoming LFV experiments". In: *Physics Letters B* 764 (2017), pp. 157–162. ISSN: 0370-2693. DOI: https://doi.org/10.1016/j.physletb.2016.11.029. URL: https://www.sciencedirect.com/science/article/pii/S037026931630692X.

[73] J.P. Perroud et al. "Isovector transitions in 1p-shell nuclei induced by radiative pion capture". In: *Nuclear Physics A* 453.4 (1986), pp. 542–590. ISSN: 0375-9474. DOI: https://doi.org/10.1016/0375-9474(86)90252-6. URL: https://www.sciencedirect.com/science/article/pii/0375947486902526.

[74] C.Wu. "Personnal communications". In: (2023).

[75] A. Edmonds et al. "Using machine learning to select high-quality measurements". In: (2019).

Acronyms

$0\nu\beta\beta$ neutrinoless double beta decay. 4, 5

$\mu^- \to e^+$ **conversion** muon to positron conversion. 5, 6, 9, 10, 89, 108–111, 116, 118, 122

$\mu^- \to e^-$ **conversion** muon to electron conversion. 4, 5, 11–13, 18, 21, 33, 36, 39, 41, 43, 69, 83, 104, 113, 117, 118, 122

BSM Beyond the SM. 1

CDC Cylindrical Drift Chamber. 18

CHT Circular Hough Transform. 49, 57, 60, 62, 75, 78

cLFV charged Lepton Flavor Violation. 3

COMET COherent Muon to Electron Transition. 3, 26

COMET Phase-I COMET Phase-I. 122

CTH CyDet Trigger Hodoscope. 18, 20, 76

CyDet Cylindrical Detector System. 15

DAQ Data Acquisition. 39, 47

DIO Decay In Orbit. 12, 98, 101, 104, 122

GBDT Gradient Boosted Decision Tree. 43, 44, 57, 102, 118, 119, 121, 122, 126

GDR Giant Dipole Resonance. 6

GEANT4 GEometry And Tracking. 26, 27

GENFIT GENeric Track-Fitting Toolkit. 73, 76, 123

GS Ground state. 4–6

ICEDUST Integrated COMET Experiment Data User Software Toolkit. 26

J-PARC Japan Proton Accelerator Research Complex. 11, 13

MR Main Ring. 13

NDF Number of Degrees of Freedom. 81, 83, 84

POT proton-on-target. 33

RCS Rapid Cycling Synchroton. 13

RMC Radiative Muon Capture. 6, 7, 9, 10, 26–28, 41, 84, 89, 90, 95, 98, 102, 118

ROC Receiver Operator Characteristics. 45, 47, 56

RPC Radiative Pion Capture. 12, 13, 16, 96, 97

SES Single Event Sensitivity. 11, 104

SM Standard Model. 1